Geosphere

E: geosphere@geosociety.org
W: geosociety.org/gsa
T: @geosociety

FOR PEER REVIEW - CONFIDENTIAL

Progradational Slope Architecture and Sediment Partitioning in the Outcropping Mixed Siliciclastic-Carbonate Bone Spring Formation, Permian Basin, west Texas

Tracking no: GS2184

Authors:
Wylie Walker (Colorado School of Mines), Zane Jobe (Colorado School of Mines), Rick Sarg, and Lesli Wood (Colorado School of Mines)

Abstract:
Sediment transport and partitioning are important for understanding slope-building processes in mixed carbonate-siliciclastic sediment routing systems. The Permian-aged Bone Spring Formation, Delaware Basin, west Texas is a mixed carbonate-siliciclastic system that has been extensively studied in its basinal extent, but poorly constrained at its proximal, upper slope segment. In this study, we constrain the stratigraphic architecture of the proximal Bone Spring Fm. outcrops in Guadalupe Mountains National Park in order to delineate the dynamics of carbonate and siliciclastic sediment delivery to the basin. These upper-slope deposits are composed predominantly of fine-grained carbonate slope facies interbedded at various scales with terrigenous hemipelagic and sediment gravity flow deposits. We identify ten slope-building clinothems that vary from siliciclastic-rich to carbonate-rich and are truncated by slope detachment surfaces that record large-scale mass-wasting of the shelf margin. X-ray fluorescence (XRF) data indicates that slope detachment surfaces contain a higher-than-normal proportion of terrigenous siliciclastic sediment, suggesting failure is triggered by accommodation or sediment supply changes at the shelf margin. Furthermore, a well-exposed siliciclastic-rich clinothem, identified here as the 1st Bone Spring Sand, provides evidence that carbonate and terrigenous sediment were deposited contemporaneously, suggesting both autogenic and allogenic processes influenced the Bone Spring Fm. stratigraphy. This mixing of lithologies at multiple scales and the prevalence of mass-wasting act as a primary control on the stacking patterns of siliciclastic and carbonate lithologies on not only the Bone Spring margin, but also in the distal portion of the Delaware Basin.

Progradational Slope Architecture and Sediment Partitioning in the Outcropping Mixed Siliciclastic-Carbonate Bone Spring Formation, Permian Basin, west Texas

Wylie Walker[1*], Zane R. Jobe[1], J. F. Sarg[1], Lesli Wood[1]

[1]*Geology and Geological Engineering, Colorado School of Mines, 1600 Illinois St., Golden, CO, United States*

*** Correspondence:**
Wylie Walker, Encana Corporation, Denver, CO
wylie.walker@gmail.com

ABSTRACT

Sediment transport and partitioning are important for understanding slope-building processes in mixed carbonate-siliciclastic sediment routing systems. The Permian-aged Bone Spring Formation, Delaware Basin, west Texas is a mixed carbonate-siliciclastic system that has been extensively studied in its basinal extent, but poorly constrained at its proximal, upper slope segment. In this study, we constrain the stratigraphic architecture of the proximal Bone Spring Fm. outcrops in Guadalupe Mountains National Park in order to delineate the dynamics of carbonate and siliciclastic sediment delivery to the basin. These upper-slope deposits are composed predominantly of fine-grained carbonate slope facies interbedded at various scales with terrigenous hemipelagic and sediment gravity flow deposits. We identify ten slope-building clinothems that vary from siliciclastic-rich to carbonate-rich and are truncated by slope detachment surfaces that record large-scale mass-wasting of the shelf margin. X-ray fluorescence (XRF) data indicates that slope detachment surfaces contain a higher-than-normal proportion of terrigenous siliciclastic sediment, suggesting failure is triggered by accommodation or sediment supply changes at the shelf margin. Furthermore, a well-exposed siliciclastic-rich clinothem,

identified here as the 1st Bone Spring Sand, provides evidence that carbonate and terrigenous sediment were deposited contemporaneously, suggesting both autogenic and allogenic processes influenced the Bone Spring Fm. stratigraphy. This mixing of lithologies at multiple scales and the prevalence of mass-wasting act as a primary control on the stacking patterns of siliciclastic and carbonate lithologies on not only the Bone Spring margin, but also in the distal portion of the Delaware Basin.

1. **INTRODUCTION**

The dynamics of continental margin evolution and sediment partitioning impact the spatial and temporal distribution of reservoir-forming elements (Saller et al., 1989; Bull et al., 2009; Playton et al., 2010; Janson et al., 2011; Stevenson et al., 2015; Hurd et al., 2016; Playton and Kerans, 2018) and record autogenic and allogenic processes acting on the system (Shanley and McCabe, 1994; Covault et al., 2006; Burgess, 2016; Madof et al., 2016; Romans et al., 2016). The importance of stratigraphic architecture and sediment partitioning on continental margin evolution has been documented in both siliciclastic (Kertznus and Kneller, 2009; Sylvester et al., 2012; Salazar et al., 2015; Stevenson et al., 2015; Prather et al., 2017) and carbonate systems (Bosellini, 1984; Sonnenfeld, 1991; Kerans et al., 1993; Ross et al., 1994; Sarg et al., 1999; Mulder et al., 2012). Clinothems (surface-bounded packages of sediment) in both siliciclastic and carbonate systems record slope evolution and the variable distribution of lithologies (Rich, 1951; Mitchum et al., 1977; Vail, 1987; Sonnenfeld, 1991; Ross et al., 1994; Sarg et al., 1999; Playton et al., 2010; Salazar et al., 2015). While most studies of clinothems have focused on siliciclastic margins (Mitchum et al., 1977; Vail, 1987; Bull et al., 2009; Kertznus and Kneller, 2009; Sylvester et al., 2012; Salazar et al., 2015; Stevenson et al., 2015; Prather et al., 2017) or steep, reef-rimmed carbonate margins (Bosellini, 1984; Katz et al., 2010; Harman, 2011; Mulder et al., 2012; Jo et al., 2015; Principaud et al., 2015; Playton and Kerans, 2018), studies of low-relief, mixed siliciclastic-carbonate margins are less well documented (Saller et al., 1989; James et al., 1991; Sonnenfeld, 1991; Fitchen, 1997; Grosheny et al., 2015; Tassy et al., 2015).

In the Permian-aged Delaware Basin of west Texas, the Victorio Peak (shelfal facies) and Bone Spring (slope, basinal facies) formations represent a low-relief, mixed siliciclastic-carbonate depositional system that is a prolific hydrocarbon system (Allen et al., 2013; Driskill et al., 2018; Schwartz et al., 2018). Studies in the Bone Spring Fm. have focused primarily on the basinal deposits, which record heterogeneity between siliciclastic and carbonate lithologies and a mixture of turbidites, mass-transport deposits, and hemipelagic-pelagic deposits (Saller et al., 1989; Montgomery, 1997a, 1997b; Asmus and Grammer, 2013; Nance and Rowe, 2015; Driskill et al., 2018). A few studies (Kirkby, 1982; Fitchen, 1997) have focused on the shelfal (Victorio Peak) deposits, documenting cyclic deposition of platform carbonates and bypassing siliciclastic sands. While both the proximal and distal portions of the sediment routing system have been documented, the upper slope segment of the Bone Spring Formation has only been partially documented (King, 1948; McDaniel and Pray, 1967; Kirkby, 1982; Fitchen, 1997).

This study constrains the progradational slope architecture and the sediment partitioning of the upper-slope Bone Spring deposits exposed in Guadalupe Mountains National Park, west Texas. The objectives of this study are to document (1) slope-building clinothems of variable and mixed lithology, (2) slope detachment surfaces that bound clinothems, and (3) abundant mass-wasting deposits and their relationship to clinothems and slope detachment surfaces. We use these results to speculate on slope evolution in a mixed-lithology margin, the role of mass-wasting and terrigenous sediment supply in shaping the margin and delivering sediment to the basin, allogenic and autogenic forcing on sediment delivery, and how the evolution of the upper slope affects the depositional processes and stacking patterns of carbonate and siliciclastic sediment in the distal Delaware Basin.

2. GEOLOGIC AND STRATIGRAPHIC SETTING

2.1 Geologic Setting

The Bone Spring Formation was deposited in the Delaware Basin, a sub-basin of the larger Permian Basin of west Texas during Leonardian time (middle Permian, ~275-280 Ma; Figure 1A inset). During the late-Mississippian assembly of the supercontinent Pangea (~326 Ma), the Permian Basin began to take shape as a foreland basin north of the Marathon-Ouachita-Sonora orogeny (Poole et al., 2005; Figure 1A inset). Compression reactivated Precambrian areas of weakness and uplifted the Central Basin Platform, creating two sub-basins of the Permian Basin, the Delaware and Midland Basins (Figure 1A inset; Hills, 1984; Hill, 1996; Amerman, 2009; Nance and Rowe, 2015). The Delaware Basin was bounded to the west and north by the Diablo Platform and Northwest Shelf, to the south by the Marathon-Ouachita-Sonora fold belt and Hovey Channel, and to the east by the Central Basin Platform and San Simon and Sheffield Channels (Figure 1A inset; Asmus and Grammer, 2013). Tectonic activity occurred until at least the middle Wolfcampian (~295 Ma; Hills, 1984; Amerman, 2009) while the Leonardian stage (~285 to 275 Ma) was generally a quiescent tectonic environment (Hills, 1984; Amerman, 2009). Subsidence related to sediment loading as well as isostatic adjustment on the basin margins created a deep (~450 meters) Delaware basin with up to 2,500 meters of Permian sediment (Hills, 1984).

Sediment routing into the Delaware Basin originated from the north and east (Soreghan and Soreghan, 2013) with some sediment input from the Marathon-Ouachita-Sonora region to the south (Hu et al., 2018; Soto-Kerans et al., 2018), where aeolian and fluvial processes delivered sediment to the shelf and shelf margin (Presley, 1987; Fisher and Sarnthein, 1988). During Leonardian time, especially during low sea-level conditions, the entrance to the open Panthalassa Ocean to the west was restricted by a sill in the Hovey Channel (Fitchen, 1997). This sill restricted water circulation in the basin, leading to euxinic basin conditions (McDaniel and Pray, 1967), minimal bioturbation, and the preservation of organic-rich sediment (Hills, 1984).

2.2 Shelf-to-Basin Stratigraphy

The evolution of the shelf-margin and basinal strata that comprise the Delaware Basin are well documented by King (1948), Sarg and Lehman (1986), Kerans et al. (1993), Sarg et al. (1999), and Kerans and Kempter (2002). Figure 2 shows the chronostratigraphic and lithostratigraphic units within the Delaware Basin that have been correlated from shelf to basin. Representing the lower-most Permian-aged rock is the Wolfcamp Fm., a mixed carbonate-siliciclastic prograding shelf-to-basin system (Silver and Todd 1969; Kvale and Rahman, 2016) that does not outcrop in the study area (Figure 1). Overlying the Wolfcamp Fm. are Leonardian-aged prograding carbonate banks to rimmed platforms with slopes of 5-20 degrees (Harris, 2000) that transition into a deep basin assemblage (Figure 2; Fitchen, 1997; Asmus and Grammer, 2013; Hurd et al., 2018). The Leonardian system is composed of the proximal Yeso Formation that represents a restricted shelf environment with aeolian red beds and evaporitic deposits (Stanesco 1991; Fitchen, 1997). The Yeso Formation transitions to the open platform Victorio Peak Formation, a carbonate grain-margin (Kirkby, 1982), that transitions to the Bone Spring Formation carbonate and siliciclastic slope and basin deposits (Figure 2; Saller et al., 1989; Montgomery, 1997a; Fitchen, 1997; see Figure 2). Fitchen (1997) described six third-order sequences within the Victorio Peak-Bone Spring margin (L1-L6; Figure 2), where sequence boundaries represent subaerial exposure on the platform and coeval sand deposition in the deep basin. Within sequences are lowstand (sand-rich) and highstand to transgressive (carbonate-rich) members thought to be representations of cyclicity in sea-level and basinal subsidence (Figure 2; Silver and Todd, 1969; Saller et al., 1989; Fitchen, 1997; Nance and Rowe, 2015). Within each of the sand-rich and carbonate-rich members, higher-order lithologic cyclicity exists in the Bone Spring basinal deposits (Montgomery, 1997a; Nance and Rowe, 2015; Driskill et al., 2018) and is interpreted to represent allogenic high frequency sequences (Nance and Rowe, 2015). A significant erosional surface separates the Victorio Peak and Bone Spring Formations from the overlying Cutoff Formation (Figure 2). This surface is known as the top of LD10 (Sarg et al., 1999) or top of L6 (Fitchen, 1997; Hurd et al., 2018). The Cutoff Formation began as a lowstand system that eroded parts of the Victorio Peak/Bone Spring margin before reaching a maximum transgression (L8/G1) that has been biostratigraphically correlated with the Leonardian to Guadalupian boundary (Hurd, 2016). Above the Cutoff Formation is the Guadalupian-aged Delaware Mountain Group, including the Brushy Canyon Formation (G5-G7), which consists of a submarine channel-fan system (Zelt and Rossen, 1995;1995; Gardner and Sonnenfeld, 1996; Gardner et al., 2008; Figure 2). Capping the succession are Guadalupian-aged reef-rimmed carbonate platforms (Capitan Formation) and their coeval basinal deposits (Figure 2; Kerans et al., 1993; Harman, 2011).

Constraining the outcropping Victorio Peak and Bone Spring Formations in Guadalupe Mountains National Park (GMNP, Figure 1) into this stratigraphic context is difficult because of paleo-erosional features (e.g. Cutoff Fm.) and poor-resolution biostratigraphy. Lithostratigraphic correlations from Fitchen (1997) suggest the Victorio Peak-Bone Spring outcrops represent the L5 and L6 shelf margin to upper slope sequences; this interpretation is supported by recent biostratigraphic and lithostratigraphic correlations in the Cutoff Fm. (Hurd et al., 2016). To complicate matters, correlating the Bone Spring Fm. outcrops to the basin can be difficult as many industry naming schemes are purely lithostratigraphic (e.g., 1st Bone Spring Sand, 1st Bone Spring Carbonate, Avalon) and biostratigraphic age control is poor in the subsurface basinal deposits (Figure 2; Driskill et al., 2018; Hurd et al., 2018). Hurd et al. (2018) correlates the base of the outcropping Cutoff Fm. (base L7) to the base of the Upper Avalon Shale in the basin (Figure 2). Therefore, the Bone Spring Fm. outcrops in our study area likely correlate to basinal rocks referred to as the Middle Avalon Carbonate, Lower Avalon Shale (boundary between L5 and L6), and some portion of the 1st Bone Spring Carbonate (Figure 2).

3. STUDY AREA AND OUTCROP MAPPING

3.1 Study Area

The study area is focused along the ‘western escarpment’ of GMNP (Figure 1B), a northward-trending footwall fault block that was created during Cenozoic extensional tectonism (Hills, 1984; Hill, 1997) and exposes Leonardian and Guadalupian-aged carbonate and siliciclastic shelf-margin stratigraphy (Figure 2; King, 1948; Hills, 1984; Harris, 1987). Post-depositional loading (Hills, 1984), Late-Cretaceous transpression (Montgomery, 1997a), and the Cenozoic-aged Huapache Monocline (Hayes, 1964; Resor and Flodin, 2010) contribute to a 2-4° eastward dip of Permian rocks along the western escarpment. King (1948) extensively mapped the National Park and the surrounding area, including the Bone Spring Formation that is well-exposed in a system of west-east trending canyons (Figure 1B). This study focuses primarily on the outcrops in Shumard and Bone canyons, as well as the west-facing exposures between the canyons (Figure 1B). Located at the entrance to Bone Canyon is the historic Williams Ranch House (Figure 1B), a blue-painted homestead built in 1908.

3.2 3D Outcrop Model and Field Measurements

A 3-dimensional (3D) digital outcrop model was built using Agisoft software and over 2,000 drone-collected photographs (Figure 3; see Supplementary Material for field-scale print). Using the existing stratigraphic framework, the study area was constrained below the Cutoff Fm. and down-dip of the lithostratigraphic boundary with the Lower Victorio Peak (Figure 3). Field observations from bedding-attitude transects (N=16 transects, n=593 bedding measurements), nine measured sections, and six photopanel interpretations (Figures 8, 10, 12, 14, Appendix A) were incorporated into the 3D model to capture depositional elements, facies relationships, and prominent stratigraphic surfaces (Figure 3).

3.3 Stratigraphic Surface Nomenclature and Mapping

Prominent stratigraphic surfaces of various scales can be mapped throughout the outcrop (Figure 3). Surfaces are identified using bedding attitude changes and truncation/onlap relationships (Figure 3). Large-scale surfaces are defined as those with more than 20 m of truncation/onlap that can be mapped along the outcrop extent (kilometer-scale) before disappearing into the subsurface, coalescing with another surface, or transitioning northwestward into the Victorio Peak shelfal facies (black surfaces, blue numbers in Figure 3B). These large-scale surfaces are interpreted as slope detachment surfaces (SDS) that may be associated with larger scale clinoform geometries. Some SDS show roll-over in the study area (SDS 4, 7, 8, 9; cf. Rich, 1951), suggesting these SDS have a clinoforming shape, much like the clinoforms mapped in the Leonardian shelf margin by Sarg (1988) and Fitchen (1997). However, because of the limited exposure of the full geometries of many of the surfaces, we refer to them as SDS. We identify nine SDS and ten intervening clinothems (defined as the strata bounded by SDS) within the study area (orange numbers, Figure 3B). Smaller-scale surfaces are defined as those with less than 20 m of truncation/onlap (red lines in Figure 3B). We interpret these smaller-scale surfaces as mass-wasting scars and slope failure deposits, and they occur within every clinothem (Figure 3B).

4. SEDIMENTARY FACIES AND DEPOSITIONAL ENVIRONMENTS

4.1 Facies

4.1.1 Naming Schemes

Facies naming schemes can be difficult in mixed carbonate-siliciclastic systems because of confusion between textural/compositional facies schemes (e.g., Dunham, 1962; Folk, 1980) and schemes that define facies based on depositional process (e.g., Bouma, 1962; Lowe, 1982; Hubbard et al., 2008). In recent years, efforts have been made to name mixed sediments focusing on the mudstone dominated environments (Milliken, 2014; Lazar et al. 2015; Driskill et al., 2018; Thompson et al., 2018). These naming conventions are useful in the basin setting but break down as one moves up-dip along the sediment routing system into the classical carbonate realm (e.g., a transition from calcareous siltstone deposited by sediment gravity flow to a lime wackestone deposited on a carbonate platform). For the purposes of this paper, we developed a system-scale facies scheme that is valid all along the sediment routing system (i.e. from shelf to basin) and can move along a continuum from carbonate-rich to siliciclastic-rich deposits (Figure 4). In our scheme, we use the historical naming convention with the highest constituent component. That is, if carbonate makes up >50% of the sediment, we use the Dunham classification scheme (Dunham, 1962), and if siliciclastic and argillaceous sediment make up >50% of the sediment we use the Folk classification scheme (Folk, 1954; Folk, 1980). To further clarify the composition of the facies, we add a modifier if a secondary constituent makes up greater than 10% of the sediment (Chiarella and Longhitano, 2012; Lazar et al., 2015). We also include a siliciclastic-carbonate ratio (s/c in Table 1) to quantify compositional variability (Chiarella and Longhitano, 2012). Because most facies within the Bone Spring Formation have primary sedimentary structures, we also add a modifier (e.g., 'laminated') to the facies name to differentiate depositional process.

4.1.2 Facies Descriptions

Eight facies were identified based on composition, grain size, depositional process, bed thickness, sedimentary structures, and fossil content. In addition to field-scale observations, facies were constrained by thin section analysis, scanning electron microscope (SEM) analysis, and X-ray fluorescence (XRF) data (Figures 4 and 5, Table 1, Appendix B). The eight facies are listed below, with the dominant interpreted depositional process in parentheses based on observations outlined in Table 1: 1) thin-bedded laminated lime mudstone (hemipelagite/sediment gravity flow deposit); 2) thin to thick-bedded deformed lime mudstone (mass-transport deposit); 3) thick-bedded bioclastic lime wackestone to packstone (hemipelagite/sediment gravity flow deposit); 4) interbedded lime mudstone and bioclastic packstone (interbedded hemipelagites and turbidites); 5) thick-bedded normally-graded bioclastic lime packstone to grainstone (turbidites); 6) thin-bedded laminated bioclast quartz siltstone (hemipelagites and turbidites); 7) thin-bedded laminated quartz lime mudstone (hemipelagites and turbidites); and 8) thick-bedded bioclastic lime packstone to grainstone (in-place shallow-water carbonate platform deposits to reworked platform deposits).

Facies show a high degree of mixing of siliciclastic and carbonate sediment (Figure 4B). Biogenic silica (i.e. chert) is abundant throughout facies and is differentiated from detrital siliciclastic by a lack of clay content (cf. Driskill et al., 2018). Depositional processes also vary considerably between facies (Figure 4A). The primary facies on the upper slope are carbonate-dominant mudstone to wackestone facies (Facies 1, 2, 3, Figure 4A) interpreted as hemipelagic and sediment gravity flow processes on the slope. Facies 1 and 2 represent a continuum of deformation on the slope ranging from undeformed (Facies 1) to highly deformed (Facies 2). Carbonate slope deposits are interbedded in places with coarser-grained sediment gravity flow deposits (Facies 4 and 5) interpreted as calciturbidites. The carbonate-dominant facies (e.g., Facies 1) occur along a facies continuum with siliciclastic-dominant Facies 6, with Facies 7 representing a medial position on the carbonate-siliciclastic continuum (Figure 4C). This continuum represents variable carbonate and siliciclastic compositional mixing on the shelf and slope during transport (Chiarella et al., 2017). Facies 8 represents the Lower Victorio Peak of King (1948) and Kirkby (1982).

4.2 Depositional Environments

Four facies associations in the outcropping Bone Spring Formation are interpreted to represent sub-environments within the mixed-lithology, shelf-slope depositional system. (Figures 6, 7).

Facies Association 1 Description

Facies Association 1 (FA1), includes F1, F3, and F8, with a predictable stacking pattern shown in Figure 6A. F1, F3, and F8 always occur in stratigraphic sequence, with F1 at the base, F3 in the middle, and F8 at the top (Figure 6A). Contacts between facies are gradational and can transition over several meters (Figure 6A).

Facies Association 1 Interpretation

FA1 represents an upward-shoaling carbonate slope environment, with increasing grain size, bed thickness, sparite and fossil content, and decreasing chert content from Facies 1 to Facies 8, representing a shoaling succession from slope carbonate mudstones and turbidites to platform carbonates (McDaniel and Pray, 1969). The upward-shoaling character of FA1 suggests the Leonardian carbonate margin was predominantly progradational in the study area.

Facies Association 2 Description

The primary facies association, Facies Association 2 (FA2), makes up roughly 90% of the study area and includes some mixture of F1, F2, and F4 (Figures 6B, 7A, B). The F1, F2, and F4 facies are interbedded and can be found transitioning laterally in a single bed-set (Figure 6B). Contacts between facies can be gradational but are predominantly sharp, with truncation below and onlap above the surface, particularly between F1 and F2 (Figures 6B, 7B).

Facies Association 2 Interpretation

FA2 represents a carbonate slope environment with abundant mass failure. The sharp erosional surfaces found within FA2 are interpreted as slope failure scarps and/or erosional bypass surfaces (Figure 7B). The lack of coarse-grained material directly mantling these surfaces (Figure 7B) supports a failure scarp interpretation. These failure surfaces are often filled with a wedge architectural pattern that is interpreted to be the filling of local topography. The chaotic bedding and folded features found in FA2 are interpreted to be mass-failure deposits on the slope

(Figure 5B, 7B). This “failure-and-fill” architecture has been well-documented in other carbonate slopes (Bosellini, 1984; Ross et al., 1994; Katz et al., 2010; Playton et al., 2010; Mulder et al., 2012; Playton and Kerans, 2018) as a mechanism for slopes prograding and aggrading over its failed deposits.

Facies Association 3 Description

Facies Association 3 (FA3) is composed of F1, F3, F5, and F8 (Figure 6C, 7C, D). The type locale of FA3 occurs on the south wall of Shumard Canyon (Figure 3), where a sharp surface with 10 m relief truncates F3, with F5 onlapping the surface (Figure 7C). The F5 deposit is a 100 m wide and 10 m thick lenticular deposit with a concave base and a flat top. Over a 10 m interval, F5 gradually transitions into F8 (Figure 6C). Other instances of FA3 (Figure 3, 6C, 7D) show similar architecture, but smaller dimensions (e.g., a 10 m wide and 0.5 m thick, lenticular F5 lying above a surface that truncates F1; Figure 7D). In some instances, Facies 5 beds offset stack, with fine-grained F1 draping previous deposits (Figure 7D).

Facies Association 3 Interpretation

FA3 is interpreted as submarine channel deposits developed in a carbonate slope setting. The erosional truncation of fine-grained facies (F1, F3) and overlying coarse-grained channel fill with normally graded beds (F5) indicates erosion and deposition by turbidity currents (Figure 4E, 7C, D; Talling et al., 2012; Janocko et al., 2013). The presence of amalgamation surfaces (Figure 7C) indicate multiple erosive events, suggesting that the channels were long-lived conduits for sediment to the deeper basin. The presence of F8 (Lower Victorio Peak) overlying the channel fill on the Shumard south wall outcrop suggests that this submarine channel was located very near the shelf edge (Figure 6C). The smaller channel deposits in association with F1 are interpreted to lie in a mid-slope position and may represent slope gully deposits (Figure 6C; Shumaker et al., 2016).

Facies Association 4 Description

Facies Association 4 (FA4) is composed of gradational interbedding of F6 and F7 (Figure 6D, 7E). The typical thickness of these interbeds of siliciclastic (F6) and mixed-lithology (F7) facies are ~ 10 cm (Figure 7E), but on the west wall of Shumard Canyon the thickness of F6 can reach 10 meters (Figure 3). Contacts between the F6 and F7 components of FA4 are typically sharp and undulatory (Figure 7E). Like FA1, FA4 contains internal truncation surfaces, with overlying deformed intervals.

Facies Association 4 Interpretation

FA4 is interpreted as periods where more siliciclastic material was delivered to the outer carbonate bank and upper slope. We interpret that this terrigenous silt-rich sediment was deposited by hemipelagic and sediment gravity flow processes. The interbedded nature of F6 and F7 (Figure 7E) suggests a high-frequency cyclicity in siliciclastic and carbonate deposition. Deformed intervals and truncation surfaces suggest an unstable slope setting dominated by failure and bypass, similar to FA2 carbonate deposits. The increased detrital siliciclastic material differentiates FA4 from FA1, suggesting a change in sediment supply that affected the primary slope-building facies (FA1).

5. STRATIGRAPHIC ARCHITECTURE

Six photopanels demonstrate the stratigraphic architecture of the Bone Spring Formation (Figures 1B, A.1; see Supplementary Material for field-scale print). We discuss four photopanels below in detail (Shumard Canyon north, Shumard Canyon south, Bone Canyon north, and Bone

Canyon south). The intervening areas (west wall Shumard Canyon, west wall Bone Canyon) were used to correlate between Shumard and Bone Canyons and provide additional stratigraphic context and are included in Appendix A.

5.1 Shumard Canyon

5.1.1 North Wall of Shumard Canyon

The north wall of Shumard Canyon represents the best-exposed transition between the Victorio Peak and Bone Spring Formations (Figure 8). Eastward and southward dipping Bone Spring outcrops (F1, F2, F3) comprise most of the north wall, with flat-lying Victorio Peak Formation (F8) making up the uppermost cliffs (Figure 8). Dip data show the Bone Spring Fm. slope built out predominantly in an easterly direction but varies in orientation from 060° to 180° (Figure 8, Figure 3A). Several areas of interest from the north wall of Shumard canyon are highlighted in Figure 9. In area A, SDS 3 (Figure 9A) spans the entire height of the outcrop (~40m relief). Bedding orientation changes significantly across the surface, shifting from 18/090 (dip magnitude/dip azimuth) below to 23/045 above. Above SDS 3, Clinothem 4 is characterized by FA4, with siliciclastic content (F6) increasing up-section (Figure 9A). Siliciclastic-dominant beds are truncated by SDS 4, a prominent truncation surface (Figure 9A) which has ~80 meters of visible relief and shows a bedding orientation change from 23/045 to 14/100. Above SDS 4, F7 gradually transitions to F1, and FA2 characterizes Clinothem 5 and 6. Bedding orientation also changes across SDS 6 (Figure 9B), with a 5-10 m thick MTD sitting directly above the surface in Clinothem 7 (Figure 9B). Above SDS 7, Clinothem 8 is characterized by FA2 but lacks a basal MTD (Figure 9C). However, Clinothem 8 contains many discordant surfaces (red surfaces, Figure 8), one with 10-20 m of overlying F1 with a wedge geometry (Figure 9D). A prominent dip azimuth shift from due east to due south also occurs in Clinothem 8, and where this change occurs, there are FA3 channel deposits (Figures 7D, 8).

5.1.2 South Wall of Shumard Canyon

SDS 3-8 and clinothem packages 4-9 can be traced from the north wall of Shumard Canyon across the canyon floor to the south wall (Figure 10). The FA4-dominated Clinothem 4 continues across the canyon (Figure 11C), but sand beds are thinner (cm-scale) and more interbedded with Facies 7 than the deposits on the north wall. Moving up-section, Clinothems 5-7 are poorly exposed but the MTD in the basal part of Clinothem 7 on the north wall of Shumard Canyon (Figure 9B) can be correlated across the canyon to the south wall (Figure 10). At this locale, the MTD displays decollement surfaces and compressional deformation features (Figure 11B). Above SDS 7, Clinothem 8 contains a ~ 10 m thick MTD (Figure 10, 11A), which was not present on the north wall (Figure 8), suggesting significant parallel-to-slope heterogeneity. FA2 is most common on the south wall, but this locale also contains the largest submarine channel deposit (FA3) in the study area (Figure 7C, Figure 10).

5.2 Bone Canyon

5.2.1 North Wall of Bone Canyon

The clinothems on the north wall of Bone Canyon display fewer bedding orientation changes and mass wasting features (F2) than in Shumard Canyon. At the entrance to the canyon the FA4-dominant Clinothem 4 is present, but the sand-rich F6 becomes progressively more discontinuous from Shumard to Bone canyon (Figures 3, 12, 13A1; Figure A.3). At the mouth of Bone Canyon, FA4 deposits in Clinothem 4 are offset by numerous normal faults (Figure 13A2) that are likely related to the primary Cenozoic escarpment-bounding fault (Figure 1). In Clinothem 8, a small-scale discordant surface truncates F1 beds and is traceable for only ~ 10 m laterally, with minimal dip attitude change across the surface (Figure 13C). Moving up stratigraphically, SDS 8 shows the same architectural elements as in Shumard Canyon, including dip attitude changes, truncation, and MTD-rich FA2 deposits (Figure 13B). In area D, SDS 9 is overlain by a 20-30 m wide by 1 m thick submarine channel deposit (FA3; Figure 13D).

5.2.2 South Wall of Bone Canyon

The south wall of Bone Canyon displays where the Cutoff Formation truncates the Bone Spring Formation with debrites composed of Victorio Peak Fm lying on the contact (Figure 14; Hurd et al., 2016). Area A highlights a large (~100 m wide x 20 m thick) wavy, deformed FA2 interval with localized thrust faults (Figure 14, 15A). Individual F1 beds can be traced through the entire feature and dip at greater than 40° in some places. We interpret this unit of FA2 to be a slope failure deposit (Figure 14, 15A). SDS 8 can be traced across Bone Canyon from the north wall just beneath this MTD (Figure 14, 15B), where a 40° bedding azimuth change occurs across the surface (Figure 15B). In area C, SDS 9 and several overlying smaller-scale discordant surfaces are identified on both canyon walls (Figure 15C). Facies 2 MTDs overlie SDS 9, and numerous bedding orientation changes indicate a failure-prone Clinothem 10 (Figure 15C).

6. FAILURE AND DEFORMATION IN THE BONE SPRING FM.

The Bone Spring Fm. outcrops provide an opportunity to observe failure and deformation in a mixed siliciclastic-carbonate slope environment, which has been understudied in comparison to purely siliciclastic margins (cf. Moscardelli and Wood, 2016). Carbonate MTDs can act as barriers, baffles, source, and reservoirs in the Delaware Basin and elsewhere (Saller et al., 1989; Allen et al. 2013; Asmus and Grammer, 2013; Thompson et al., 2017; Bhatnager et al., 2018; Driskill et al., 2018). Therefore, an improved understanding of failure and deformation from the outcrop can lead to better identification in core and well-logs, resulting in better reservoir prediction.

6.1 Scale of Failure and Deformation

Failure and intrastratal deformation occur at many scales on the Bone Spring Fm. upper slope. Most commonly, intrastratal deformation occurs on the micro-scale, typically acting on individual lamina (< 1 cm) within individual 5-20 cm thick beds (Figure 16A1, A2). Micro-scale failure and intrastratal deformation is common within carbonate mudstone facies (F1, F2), including slumping, water-escape, folding, imbricate stacking (cf. Auchter et al., 2016), convolute bedding, micro-faults, and detachment surfaces (Figure 16A1, A2). Soft-sediment deformation of similar geometry is also found on the meso-scale (1-20 meters, Figure 16B, C, D) and macro-scale (>20 meters, Figure 15A). At the meso-scale, failure surfaces (red surfaces in Figure 9D, Figure 13C, Figure 3) likely represent detachments for slope-attached failures (Moscardelli and Wood, 2008). Meso-scale MTDs are common on the slope and consist of meter-scale carbonate F1 and F2 slump and debris flow deposits (Figures 16B, C, 11B) and siliciclastic slope facies (F6 and F7; Figure 16D).

At the macro-scale, slope detachment surfaces (SDS) can be correlated the length of the study area (>1 km) and display minimum visible relief of 20-100 meters (Figure 3). These surfaces are marked by truncation, bedding orientation changes across the surface, and a lack of karsting or other evidence of subaerial exposure (Figure 9A). We interpret these surfaces to represent the evacuation scars for subaqueous mass-failures (Bosellini, 1984; Bull et al., 2009; Mazzanti and De Blasio, 2010; Janson et al., 2011; Mulder et al., 2012; Principaud et al., 2015). Headwall scarps from sediment evacuation on carbonate slopes often have steep angles (Mulder et al., 2012; Jo et al., 2015; Principaud et al., 2015), and SDSs in the study area have structurally-restored dips of 15-25 degrees. The lack of macro-scale MTDs in the study area suggests that most MTDs were sourced from this steep (~15 degrees) upper slope locale, bypassing this zone and deposited more distally. This slope segmentation, with large-scale MTDs sourced in the upper slope, bypassing the slope, and being deposited at the toe-of-slope or further into the basin, has been documented both in the Permian Basin (Saller et al., 1989; Montgomery, 1997a; Allen et al., 2013; Nance and Rowe, 2015; Bhatnager et al., 2018; Hurd et al., ,2018, Schwartz et al., 2018) and in other carbonate slope systems (De Blasio et al., 2005; Moscardelli and Wood, 2008; Mazzanti and De Blasio, 2010; Janson et al., 2011; Mulder et al., 2012; Dakin et al., 2013; Principaud et al., 2015; Cardona et al., 2016; Moscardelli and Wood, 2016).

6.2 Deformation Style and Character

Different styles of deformation provide insight into process, material strength and rheology, basin orientation, and failure conditions (Figure 17; Dott, 1963; Fisher, 1983; Stow, 1986; Elverhoi et al., 2000; Eyles and Eyles, 2000; Strachan, 2002; De Blasio et al., 2006; Moscardelli and Wood, 2008; Tripsanas et al., 2008; Haughton et al., 2009; Mazzanti and De Blasio, 2010; Talling et al., 2012; Auchter et al., 2016; Jablonska et al., 2018). Styles of intrastratal deformation range from creep to slide to slump to debris flow, but often deposits reflect a continuum between these styles (Figure 17; Dott, 1963; Nemec, 1990; Strachan, 2002; Tripsanas et al., 2008; Haughton et al., 2009; Talling et al., 2012). Creep deposits (sensu Auchter et al.,

2016) are observed at many scales on the outcrop (Figure 17A, Figure 16A1, A2, Figure 15A) and are composed primarily of carbonate mudstone facies (F1, F2, F3) that have preserved strata and plastic deformation (folds, boudinage) and little to no brittle failure (Figure 17A, Dott, 1963; Stow, 1986; Moscardelli and Wood, 2008; Auchter et al., 2016). A macro-scale example of creep is documented from Bone Canyon south (Figure 15A), where deformed beds reach dips of 40° with minimal intra-bed disturbance, indicating high strength and coherency of the failing rock material (Dott, 1963; Stow, 1986; Elverhoi et al., 2000; Tripsanas et al., 2008; Talling et al., 2012). The prevalence of multi-scale creep within the carbonate slope facies (Figure 16A1, A2) suggest that the Bone Spring slope was almost always over-steepened and prone to failure (Stow, 1986).

Slide and slump deposits in the study area are composed of carbonate mudstone facies (F1, F2, F3) where bedding is generally preserved (Figure 11A), but plastically deformed (folds, boudinage, disrupted bedding) with minor brittle deformation (faulting, breccia; Figure 17B1, B2, B3). Slump deposits often sit on basal detachment surfaces that show brecciation and fracturing at the base (Figure 17B1, B2, B3; see basal shear zone, Cardona et al., in review). Slumping is differentiated from creep by evidence of brittle failure and high basal shear, suggesting detachment and transportation along the slope (Stow, 1986; Eyles and Eyles, 2000; Strachan, 2002; Moscardelli and Wood, 2008). Deposition of slump deposits on the steep Bone Spring slope indicate high material strength that prevented subsequent failure and/or transformation into a debris flow (Dott, 1963; Fisher, 1983; Elverhoi et al., 2000; De Blasio et al., 2006; Tripsanas et al., 2008).

Lastly, debris flow deposits (i.e., debrites) are composed of carbonate mudstone facies (F1, F2, F3) with minimal preserved strata (Figure 16B, C, Figure 9B), a chaotic fabric with matrix supported clasts (Figure 17 C, D), brittle deformation features (breccia, fractures; Figure 17C, D), and erosional bases (Figure 17C, D), features common to debrites (Dott, 1963; Fisher, 1983; Stow, 1984; Moscardelli and Wood, 2008; Tripsanas et al., 2008; Talling et al., 2012). The chaotic fabric with brittle and erosional basal deformation suggests laminar flow with high basal shear stresses during transport (Dott, 1963; Stow 1984; Haughton et al., 2009., Talling et al., 2012). Flow transformation (Fisher, 1983; Haughton et al., 2009; Talling et al., 2012) of debris flows along the sediment routing system may reflect the abundance of hybrid event beds in the distal Delaware basin (Driskill et al., 2018).

7. PARTITIONING OF CARBONATE, BIOGENIC SILICA, AND TERRIGENOUS SILICICLASTIC SEDIMENT

The presence and partitioning of mixed sediment on the Bone Spring slope is constrained by handheld XRF measurements (Figure 18). Ternary diagrams of Silicon, Calcium, and a clay-proxy (Aluminum + Titanium; cf. Tribovillard et al., 2006) establish carbonate-rich and siliciclastic-rich facies end-members (Figure 18). These domains are corroborated by thin section, SEM, and hand sample analysis. However, biogenic silica is abundant on the Bone Spring slope due to sponge spicules and radiolaria that have been diagenetically altered to chert nodules and beds (Figure 7A; McDaniel and Pray, 1967). Chert beds are high in silicon and can cause confusion for evaluating a terrigenous source of silica; to mitigate this, we add a trendline representing a continuum from carbonate- to terrigenous-dominate environments (Figure 18). Samples that plot off this trendline can be suspected of having a diagenetic component. For example, some samples have high Si but low Ti+Al (e.g., two Facies 5 samples highlighted in Figure 18), and thin section analysis (Figure 5E) reveals that these samples (1) are cemented by siliceous chert that is not derived from a terrigenous source and (2) little to no detrital siliciclastic sediment present. Other XRF-based methods to distinguish biogenic silica from detrital silica (e.g., Si/Al, Zr/Al, and Zr/Cr ratios) have also been useful in the Bone Spring Fm. (Driskill et al., 2018).

The most common facies in the study area are carbonate mudstones (F1, F2, F4), and these facies plot in the carbonate domain but with variable terrigenous input (Figure 18). Thin sections reveal that a small volume (<10%) of well-rounded, silt-sized, terrigenous, siliciclastic sediment is present (Figure 4A, B), causing the variability of terrigenous material within the carbonate-dominate facies. The siliciclastic sediment is interpreted to be aeolian-derived dust that was transported from onshore aeolian fields (Presley, 1987; Fisher and Sarnthein, 1988; Cecil et al., 2018) during high relative sea levels and high carbonate production. The siliciclastic siltstone facies (F6) plot within the siliciclastic-domain (Figure 18) and are interpreted as hemipelagic and sediment gravity flow processes connected to higher detrital siliciclastic sediment supply. The mixed-facies (F7) plot along a continuum between the carbonate- and siliciclastic-domain and represent a range of compositional mixing between F1 and F7 (Chiarella et al., 2017).

XRF transects taken across SDS 4, 6, 7, 8, and 9 (Figures 8 and 13) demonstrate an enrichment of terrigenous sediment input associated with slope detachment surface development (Figure 19). Each transect, with the exception of transect 1, begins within the mixed- or carbonate-domain (circle symbols, Figure 19) and shifts toward the siliciclastic-domain at the surface (square symbols). Following this shift, the transects move back into the mixed- or carbonate-domain (triangle symbols). This shift occurs in every transect but each transect is positioned in different parts of the calcium/silicon spectrum. Most transects (Figure 19B-E) occur within the mixed-domain with a shift toward the siliciclastic-domain at the surface, while the SDS 4 transect

(Figure 19A) occurs predominantly within the siliciclastic-domain. This latter transect is associated with the FA4 deposits in Clinothem 4 (Figure 3, Figure 9A).

We interpret these results to record failure of the margin as the result of an influx of terrigenous siliciclastic sediment caused by the interplay of accommodation and sediment supply (hereafter referred to as A/S, cf. Shanley and McCabe, 1994). ‘A’ refers to accommodation that directly impacts both the position of terrigenous sediment (shoreward vs basinward) and the production of carbonate (e.g. high production during high accommodation). Variable progradation and aggradation of carbonate sediment are captured in the ‘A’ term (e.g. high aggradation of carbonate decreases accommodation). ‘S’ refers to sediment supply of terrigenous sediment. Because terrigenous siliciclastic sediment is associated with development of slope detachment surfaces (i.e., failures), we interpret several possible mechanisms for large-scale failure: (1) an increase in loading from terrigenous sediment supply (Sultan et al., 2004; Vanneste et al., 2014), (2) weakened substrate from siliciclastic material (Kenter and Schlager, 1989; Kenter, 1990), (3) steep relict slopes created by the carbonate-dominant environment (Schlager and Camber, 1986; Ross et al., 1994). Likely a combination of all three mechanisms initiated large-scale slope failure. The steep Bone Spring slope locally (10-20°) surpasses the predicted stability spectrum for carbonate mudstone margins (Kenter, 1990), so the introduction of weaker siliciclastic sediment onto an over-steepened carbonate slope may initiate failure. The position of four of the surfaces within the mixed- to-carbonate-domain (Figure 19B-E) suggest that only a slight increase in terrigenous sediment influx is necessary to trigger large-scale failure.

Overlying the SDS, siliciclastic sediment can occur as thin draping beds (<5 cm, Figures 9B, C, 12B, D) with higher carbonate content (Figure 19B-E), or as meter-thick beds (Figure 9A) that are carbonate poor (Figure 19A). The meter-scale siliciclastic beds may record a relatively large decrease in A/S, while thin beds record only a minor decrease in A/S. In either case, allogenic or autogenic changes can produce these A/S changes, and the result is slope failure and bypass of siliciclastic sediment into the basin.

8. DISCUSSION

8.1 Evolution of the Victorio Peak-Bone Spring Mixed Margin

Outcrop observations of SDS and clinothem characteristics coupled with facies distributions aid in reconstruction of the Leonardian shelf-slope profile in the study area. We use the evolution of the 10 clinothem packages described above to generalize slope-building processes and sediment delivery/partitioning in a mixed-lithology margin, including a 3D reconstruction of the study area (Figure 20A-D) and the resulting shelf-to-basin cross-section (Figure 20E). Four possible evolutionary steps are detailed (A, B, C, D), and the route the system takes through these steps may vary both laterally and temporally.

In time step A (Figure 20A) A/S is high (i.e. A/S>1), promoting high carbonate production with minimal detrital siliciclastic sediment input. Carbonate-rich hemipelagic and sediment gravity flow facies (Facies 1, 2, 3, 4, 5, 8) deposit on the slope and basin with minor siliciclastic input present as aeolian dust transport (Figure 18; Cecil et al., 2018). The slope builds out with spatially variable progradation and aggradation, accounting for temporal changes in carbonate production and along-strike variability in slope morphology (Saller et al., 1989). The dominance of carbonate facies creates a relatively stable, albeit steep, environment, with minor micro-scale intrastratal deformation and meso-scale slope-attached MTDs (Figure 20A; Moscardelli and Wood, 2008). Clinothem packages 1-3, 5-10 (Figure 3) represent the stratigraphic record of time step A.

In time step B (Figure 20B) siliciclastic and argillaceous sediment supply increases, decreasing A/S (e.g., A/S approaching 1), destabilizing the shelf-margin and upper slope, creating macro-scale, shelf-attached failures that develop into a slope detachment surface with associated MTDs (Facies 2). These SDS may be part of a larger clinoform surface. Siliciclastic sediment draping surfaces indicates bypass into the basin (Facies 6 and 7, Figure 20E; Armitage et al., 2009; Amerman et al., 2011; Grosheny et al., 2012). SDS 1, 2, 5-9 (Figures 3, 9B, C, 12B, D) and Clinothems 1-3, 5-10 are representative of time step B (Figure 3).

In time step C (Figure 20C) further decrease of A/S (e.g. A/S approaching 0) introduces larger volumes (relative to time step B) of siliciclastic and argillaceous material to the shelf edge and slope. A clinothem is built by siliciclastic material (Facies 6), with the amount of carbonate facies (Facies 7) dependent on the local carbonate production and flux of siliciclastic sediment. The steep, inherited slope also promotes bypass of siliciclastic sediment into the basin (Figure 20E). SDS 3 and 4 and Clinothem 4 represent the outcrop expression of time step C (Figure 3).

In time step D (Figure 20D) A/S returns to time step A conditions. Carbonate production again dominates, and the slope begins to prograde and aggrade over its failed deposits. Dip attitude changes across SDS in the study area suggest a complex, 3D slope morphology as the slope builds over its relict topography, perhaps with a strike-oriented lobate clinothem shape (Figures 22C1, C2, 8, 10, 12, 14). This lobate style of progradation and aggradation on carbonate slopes has been documented as a mechanism for slope building in the Bone Spring Fm. (Saller et al., 1989) and in other carbonate clinoform systems (Sonnenfeld, 1991; Gomez-Perez et al., 1999; Katz et al., 2010; Playton et al., 2010; Playton and Kerans, 2018). Carbonate packstone and MTD facies (Facies 2, 4, 5) are common at the base of clinothems, as the relict scarp surfaces attract coarse-grained sediment bypass (Eggenhuisen et al., 2010; Janson et al., 2011; Stevenson et al., 2015). Toward the top of clinothem fill, undeformed lime mudstone facies (Facies 1) dominate as the slope finds local equilibrium.

Lobate clinothem architecture and coarse-grained bypass is demonstrated on the north wall of Shumard Canyon (Figure 21). In Clinothems 1-7, bedding orientations show an easterly slope progradation direction (90°, Figure 21B). At or near SDS 7 (Figure 21A), bedding orientations shift to a primarily southward progradation direction (180°, Figure 21B). We interpret this rotation to record a slope inflection point, where a local re-entrant may have locally focused deposition (Figure 21C). A high density of slope failure surfaces and MTDs at the inflection point may be related to focusing of deposition, and four submarine channel deposits are aligned here (Figure 3, Figure 21A), suggesting that topographic lows created from failures may have acted as conduits for coarse-grained sediment gravity flows (Figure 21C). These observations suggest that the Shumard Canyon area may have been an entry point for coarse-grained sediment for a portion of the northwestern Delaware Basin (Figure 1). Documentation of sediment conduits in both the Cutoff (Hurd et al., 2018) and Brushy Canyon (Gardner et al., 2008) formations at this location corroborate our observations of a prolonged basin entry point at this location.

In the study area, 7 of the 9 surfaces (SDS 1, 2, 5-9) likely followed an ABD path, skipping time step C and only storing siliciclastic sediment as thin bypass deposits (Figure 19B-E, Figures 9B, C, 13B, D). From SDS 3 to 4, the system likely followed an ABCD path, with a high magnitude decrease in A/S accounting for thicker siliciclastic beds on the slope (i.e. time step C; Figures 19A, 9A). A prolonged decrease in A/S (e.g. A/S ~ 0), for example the Bone Spring 1^{st}, 2^{nd}, and 3^{rd} Sands, would follow a similar path (i.e. ABCD), with time step C representing relatively large geologic time periods and large volumes of siliciclastic sediment bypass to the basin (Stevenson et al., 2015). A schematic cross-section of this time sequence (i.e. ABDABCD) is illustrated in Figure 20E.

8.2 Implications for Sequence Stratigraphic Concepts

Sequence stratigraphic concepts are commonly used for predicting facies from seismic-scale geometries (Mitchum et al., 1977; Vail, 1987). However, allogenic forcing is often over-relied upon without considering autogenic forcing and along-strike variability (see discussion in Burgess, 2016), resulting in over-simplified stratigraphic ‘pancake’ models for basin fill (e.g., a local sand body interpreted to represent a correlable lowstand all across a basin; Figure 22A; Saller et al., 1989; Montgomery, 1997b; Crosby et al., 2017; Bhatnager et al., 2018; Schwartz et al., 2018). Many studies have shown that sediment supply, accommodation, along-strike variability, and many other factors affect the regional and local development of both low-order and higher-order systems tracts and sequences (Covault et al., 2006; Burgess, 2016; Madof et al., 2016; Harris et al., 2018; Trower et al., 2018).

Results from this study suggest that carbonate and siliciclastic clinothem partitioning can be created by multiple forcing mechanisms. From an allogenic perspective, the siliciclastic beds associated with SDS (Figures 3, 19) could record sea level fluctuations of different magnitude; in this case, we would expect similar processes occurring regionally, resulting in a relatively correlable basin stratigraphy (Li et al., 2015; Nance and Rowe, 2015). From an autogenic perspective, variable carbonate progradation and aggradation rates result in a rugose margin (Saller et al., 1989) that may provide conduits for siliciclastic sediment into the basin without changing sea level. As the margin compensationally builds by growth and failure (Figure 20; Saller et al., 1989; Playton et al., 2010), along-strike variability (cf. Madof et al., 2016) may result in local variability in sediment input, clinothem composition and architecture, and a highly heterogeneous basin stratigraphy with contemporaneous carbonate and siliciclastic sediment deposition.

The sand-rich clinothem documented on the outcrop (Clinothem 4, Figure 3) may provide insight into this question. Based on the volume of sand deposited on the slope (Figure 3) and the high enrichment of terrigenous material (Figure 19A), we interpret this clinothem to represent the slope expression of the local 1st Bone Spring Sand (see basin stratigraphy, Figure 2), representing the base of the L5 sequence. An alternative hypothesis is that this sand-rich clinothem represents a sand-body within the larger-scale prograding L5 carbonate package. Further work correlating this clinothem to the shelf and the basin via biostratigraphy and well logs would provide further context to this hypothesis. In either case, the disconnected architecture and interbedding with carbonate facies (Figures 3, 7E, 11C, 13A1) suggests that autogenic processes are superimposed onto an allogenic signal, but deconvolving those signals would be very difficult. We advise to consider that both autogenic and allogenic processes contemporaneously act to build Bone Spring stratigraphy, and this complexity should be considered when making local and regional well correlations in the Delaware Basin and in similar mixed sediment routing systems (Figure 22B; Hampson, 2016; Madof et al., 2016; Romans et al., 2016).

8.3 Sub-seismic Scale Predictions from Seismic-scale Architectural Elements

Along strike, SDS 1-9 can be correlated for more than 1 km (Figure 3, 21) and have relief/thickness values greater than 20 m, indicating these are seismic-scale geometries. The spatial and temporal distribution of facies and depositional elements associated with SDS show how seismic-scale architecture can be used for prediction of sub-seismic-scale facies variability.

Subsurface features of similar scale and architecture are imaged in seismic reflection data from the Leonardian margin along the Northwest Shelf (Figure 23; Sarg, 1988, Sarg et al., 1999). A seismic-scale basinal siliciclastic wedge is interpreted (labeled Lower Avalon, Figure 23B) with a carbonate package prograding over the top of the sand (labeled Victorio Peak and Bone Spring Carbonate, Figure 23B). Within the prograding package, clinoform geometries are identified (orange lines, Figure 23B). Outcrops of the Bone Spring Fm. from this study are shown at the same scale as the seismic data (Figure 23C1, C2), reinforcing the outcrop as an analog for the subsurface, particularly for predicting sub-seismic-scale facies distributions. From the results in this study, we expect MTDs and siliciclastic facies to onlap clinoforming slope detachment surfaces at the toe-of-slope and in the basin and become progressively more carbonate-rich moving stratigraphically towards the top of the clinothem (Figure 20).

9. CONCLUSIONS

The stratigraphic architecture of the outcropping Bone Spring Fm. of Guadalupe Mountains National Park provides an opportunity to investigate slope-building processes and sediment delivery in a mixed siliciclastic-carbonate margin. This dataset reveals slope-building clinothems of mixed lithology bounded by slope detachment surfaces that are the result of large-scale subaqueous failure of the carbonate margin. Terrigenous sediment often mantles the slope detachment surfaces, suggesting that slope failure may be related to terrigenous sediment influx. At the base of clinothems, carbonate mass-transport deposits (MTDs) and coarse-grained carbonate allochem facies are common as the slope fills in its failed topography. At the top of clinothems, undeformed carbonate mudstone facies dominate as the slope finds local equilibrium. Bedding attitude data show dip azimuth changes between clinothems, suggesting that the primary mechanism for slope evolution was through compensationally-stacked lobate slope-building packages. A documented slope inflection point contains abundant failures and submarine channel deposits, suggesting that coarse-grained entry points to the basin are influenced by slope morphology.

Siliciclastic-rich deposits of the Bone Spring Fm. provide insight into sequence stratigraphic concepts in a mixed slope environment. A siliciclastic-rich clinothem documented in the study area is interpreted as the slope equivalent of the basinal 1st Bone Spring Sand. The nature of this clinothem (e.g., interbedding with carbonate sediment, variable lateral thickness) suggests that both autogenic and allogenic processes influenced deposition. Therefore, we suggest that both autogenic and allogenic processes be considered concurrently when making well-to-well correlations in the Delaware Basin.

These slope-building processes documented on the Bone Spring Fm. elucidate how mixed margins evolve and act as a primary control on compositional stacking patterns and depositional styles in the basin. Insight from this study can be used to reconstruct local margins and aid in predicting reservoir-forming facies types in the basin.

APPENDIX

Appendix A: Additional Photomosaics

Additional photomosaics were compiled from the outcrop to aid in the 3D reconstruction. The location of the photomosaics are shown in Figures 1B and A.1. Photopanels from the west wall of Shumard Canyon (Figure A.2) and the west wall of Bone Canyon (Figure A.3) were especially important for connecting Shumard and Bone Canyons and portraying the shelf-strike perspective of the outcrops.

Appendix B: Extended Facies Descriptions

Facies 1: thin-bedded laminated lime mudstone (hemipelagite/sediment gravity flow deposit)

Facies 1 is the primary facies present in the Bone Spring outcrop (Figure 4). The grains in this facies include carbonate allochems, detrital quartz, and pyrite. These grains are surrounded by a matrix composed of carbonate clay and minor argillaceous clay. The detrital siliciclastic to carbonate percentage is approximately 08/92 percent. However, the s/c ratio can show variability representing increasing or decreasing compositional mixing. Planar laminations can be seen on the outcrop and thin section scale (Figure 5A). The planar beds alternate between dark black to dark brown in the outcrop, and thin sections show that the dark black portion is composed of higher proportion of clay (Figure 5A). The alternation of clay and silt layers may represent segregation of grain size indicating some degree of turbulence. Some evidence of soft-sediment deformation (SSD) can be found in this facies, but Facies 1 is a lower-end member of a continuum with Facies 2 representing decreasing to increasing deformation on the slope (Figure 4A). Laterally continuous chert beds are ubiquitous in Facies 1. These chert beds appear to be cyclical and are typically 5-10 cm thick, occur approximately every 10-20 cm, and follow bedding planes. Facies 1 is interpreted to be hemipelagic and sediment gravity flow processes deposited on the upper-to-middle slope.

Facies 2: thin to thick-bedded deformed lime mudstone (mass-transport deposit)

Facies 2 is identical to Facies 1 in composition, grain size, and siliciclastic to carbonate content, but differs in sedimentary structures. Facies 2 represents the high-end member of the deformation continuum (Figure 4A) with Facies 1. In this facies, SSD sedimentary structures such as water escape, convolute bedding, microfracturing, and folded strata (recumbent folds, imbricate folds) can be identified, but in many instances, there is no distinguishable bedding (i.e. chaotic bedding, Figure 5B). The prevalence of identifiable sedimentary structures and bedding distinguishes the intensity of deformation experienced, with more visible and coherent bedding moving toward the low-end continuum member. Chert beds typically mimic the character of the bedding. In highly deformed hand samples, thin sections show a high degree of fracturing with fractures filling with carbonate cement (Figure 5B). Facies 2 is interpreted to be hemipelagic and sediment gravity flow slope deposits that have experienced syn- and post-deposition deformation on the upper-to-middle slope.

Facies 3: thick-bedded bioclastic lime wackestone to packstone (shallow-water, reworked-carbonate platform deposit)

Facies 3 is similar to Facies 1 and 2 in composition but differs in higher content of coarse-grained bioclastic material and sparite. In this facies, crinoids, peloids, shell fragments, and sponge spicules can be easily identified in outcrop (Figure 5C). Additionally, Facies 3 differs from Facies 1 and 2 with less-visible sedimentary structures, lighter color, and lower frequency of chert beds (approximately every 30-40 cm). The lower frequency of chert beds likely indicates overall thickening of beds. Chert beds may be continuous, like found in Facies 1 and 2, but are more often nodular (Figure 5C). Thin sections show the coarse-grained fraction to be made up very fine sand carbonate and biogenic grains (crinoids, bryozoan, brachiopods, peloids, shell fragments, spicules) with minimal, if any, detrital siliciclastic grains observed (s/c ratio <<1; 5C). Facies 3 is interpreted to be hemipelagic deposits on the upper-slope. The high presence of coarse-grained bioclastic content indicates proximity to the shelf margin relative to Facies 1 and 2.

Facies 4: interbedded lime mudstone and bioclastic packstone (interbedded hemipelagites and turbidites)

Facies 4 is composed of two elements: a carbonate mudstone element and a bioclastic packstone element (Figure 4A). The carbonate mudstone is identical to Facies 1. The bioclastic packstone element is composed of coarse-grained (very fine to coarse sand) carbonate grains that are mostly grain supported. Carbonate grains are composed of similar material found in Facies 1-3 (crinoids, brachiopods, bryozoan, spicules; Figure 5D). In the bioclastic packstone beds there is evidence of cementation from calcite and dolomite (Figure 5D). The packstone beds are typically on the order of cm- to mm-scale and have a frequency within the lime mudstone approximately every 1-2 centimeters and can be continuous, lenticular, or starved ripple beds (Figure 5D). Facies 4 is interpreted to be hemipelagic slope deposits with occurrences of sediment gravity flows, likely distal or low-density turbidity flows. These flows are pulses of shelfal material being swept off the shelf margin onto the slope, likely from wave, storm, current, or tidal forces.

Facies 5: thick-bedded normally-graded bioclastic lime packstone to grainstone (turbidites)

Facies 5 is made up of approximately 85% coarse-grained sediment, typically medium to coarse grain (0.5 to 1 mm in diameter) with some grains reaching pebble size. Grains are made up entirely of carbonate or biogenic grains (siliciclastic to carbonate content, 0:100) that are distinguished in hand sample and thin section as crinoids, peloids, brachiopods, bryozoan, mollusks, sparite grains, sponges, and sponge spicules (Figure 5E). Thin sections reveal that there is high occurrence of sparite and siliceous chert cement (Figure 5E). The source of the chert cement is from biogenic siliceous material present on the upper-slope (sponge spicules and radiolarians). In some occurrences of Facies 5, chert cement has entirely replaced beds. Additionally, some samples show higher degrees of sparite, ranging from 15-30% on the outcrop. Fabric indicates some normal grading, but also show poorly-sorted, “patchy” beds in many places (Figure 5E). Other sedimentary structures observed are low-angle scours, amalgamation surfaces, styolites, and continuous red-brown colored beds. The presence of grading, amalgamation surfaces, and depositional hiatuses (red surfaces) suggest these are multiple carbonate sediment gravity flows, most likely turbidity current deposits (calciturbidites).

Facies 6: thin-bedded laminated bioclast quartz siltstone (hemipelagites and turbidites)

Facies 6 is similar to Facies 1 except for a higher detrital siliciclastic silt fraction (s/c>1, Figure 5F). This facies is made up of very fine detrital quartz and carbonate allochems set in a silt and clay matrix. The matrix is dominated by siliciclastic grains and argillaceous mud (Figure 5F). The ratio of siliciclastic to carbonate can vary and represents a siliciclastic-rich end member in continuum with Facies 1 (Figure 4A). The increasing siliciclastic and argillaceous content contributes to a noticeable lighter-brown color and different weathering pattern (Figure 5F). Sedimentary structures are planar laminations to mostly a homogeneous, structureless face both in outcrop and in thin section (Figure 5F). Chert is noticeably absent in this facies. Facies 6 is interpreted to be siliciclastic-rich hemipelagic deposits on the upper-slope and possibly direct settling of aeolian sediment blowing offshore. Facies 6 represents a clear change in accommodation or sediment supply in comparison to the other hemipelagic facies (F1, F2, F3).

Facies 7: thin-bedded laminated quartz lime mudstone (hemipelagites and turbidites)

Facies 7 is on a siliciclastic-to-carbonate continuum with Facies 1 and 6, representing approximately a medial position between the two facies (Figure 4A). The siliciclastic-carbonate ratio here is approximately 1, with about 45% siliciclastic and 55% carbonate material (Figure 5G). The facies is composed of very fine detrital quartz with minimal allochems present set in a carbonate mud and sparite matrix (Figure 5G). Like Facies 6, detrital quartz grains are well rounded (Figure 5G) and likely represent aeolian sediment. In outcrop, minimal sedimentary structures are observed but show some lamination with chert beds 5-10 cm thick and occur every 10-20 cm. This facies is slightly browner in color than Facies 1 but darker than Facies 6 (Figure 5G). Facies 7 is interpreted to be hemipelagic material with an increase in detrital influence, either from aeolian settling or hemipelagic processes.

Facies 8: thick-bedded bioclastic lime packstone to grainstone (shallow-water carbonate platform deposits)

Facies 8 is similar to Facies 1, 2, and 3 but shows a higher coarse-grained bioclastic content, lighter color, less sedimentary structures, and thicker bedding (Figure 4A). Thin sections show Facies 8 is grain supported with crinoids, bryozoan, brachiopods, peloids, sparite grains, bivalves, sponges, and sponge spicules visible (Figure 5H). The fine-grained fraction is entirely sparite, with no carbonate mud present. Chert beds are continuous to nodular and occur approximately every 0.5 to 1 meter, which is interpreted to represent higher bed thicknesses than Facies 1-3. Sedimentary structures are rarely observed and have not been documented, likely indicating proximity to production centers. Facies 8 is interpreted to be carbonate platform in situ deposits. The higher content of bioclastic material indicates a more proximal location to the outer shelf than Facies 3 so represents the outer shelf margin environment rich in sponges, crinoids, and brachiopods. Deposits were likely interacting with tidal, storm, and/or current processes. This facies has been previously identified as Lower Victorio Peak by Kirkby (1982) and will be considered Lower Victorio Peak for the remainder of this paper.

ACKNOWLEDGMENTS

We would like to thank Colorado School of Mines and the Chevron Center for Research Excellence (CoRE) for providing the primary funding for this project. Additional funding was provided by the West Texas Geological Society (WTGS), AAPG Grants-In-Aid, and the SEPM Foundation. We would like to thank Sebastian Cardona, Evan Gross, Thomas Martin, and Enry Horas Sihombing for assistance during field work and Mary Carr for providing useful feedback that improved the paper.

REFERENCES CITED

Allen, J., DeSantis, J., Koglin, D. and Chen, F., 2013, Integration of structure and stratigraphy in Bone Spring tight oil sandstones using 3D seismic in the Delaware Basin, TX. Unconventional Resources Technology Conference, 2521-2527

Amerman, R., 2009, Deepwater mass-transport deposits: Structure, stratigraphy, and implications for basin evolution, [PhD dissertation]: Colorado School of Mines, Golden, Colorado, 152 p.

Amerman, R., E.P. Nelson, M.H. Gardner, and B. Trudgill, 2011, Submarine mass-transport deposits of the Permian Cutoff Formation, West Texas, USA: Internal architecture and controls on overlying reservoir sand deposition, *in*, C.R. Shipp, P. Weimer, and H.W.

Posamentier, eds., Mass-transport deposits in deepwater settings: Society for Sedimentary Geology Special Publication 96, 235-268

Amitage, D.A., B.W. Romans, J.A. Covault, S.A. Graham, 2009, The influence of mass-transport deposit surface topography on the evolution of turbidite architecture: the Sierra Contreras, Tres Pasos Formation (Cretaceous), Southern Chile: Journal of Sedimentary Research, v. 79, 287-301

Asmus, J.J., Grammer, M.G., 2013, Characterization of Deepwater Carbonate Turbidites and Mass-Transport Deposits Utilizing High-Resolution Electrical Borehole Image Logs: Upper Leonardian (Lower Permian) Upper Bone Spring Limestone, Delaware Basin, Southeast New Mexico and West Texas: Gulf Coast Association of Geological Societies Transactions, v. 63, 27-65

Auchter, N. C., Romans, B. W., & Hubbard, S. M., 2016, Influence of deposit architecture on intrastratal deformation, slope deposits of the Tres Pasos Formation, Chile: Sedimentary Geology, 341, 13–26

Bhatnagar, P., M., Scipione, M., Bianco, R., 2018, Characterization of mass transport deposit using seismic attributes: Spraberry formation, Midland Basin, west Texas: SEG International Exposition and 88th annual meeting

Bosellini, A., 1984, Progradation geometries of carbonate platforms: examples from the Triassic of the Dolomites, northern Italy: Sedimentology, 31(1), 1-24.

Bouma, A.H., 1962, Sedimentology of Some Flysch Deposits: A Graphic Approach to Facies Interpretation: Amsterdam Elsevier, 168 pp.

Bull, S., Cartwright, J. and Huuse, M., 2009, A subsurface evacuation model for submarine slope failure: Basin Research, 21(4), 433-443

Burgess, P. M., 2016, The future of the sequence stratigraphy paradigm: Dealing with a variable third dimension: Geology, 44(4), 335–336

Cardona, S., L. J. Wood, R. J. Day-Stirrat, and L. Moscardelli, 2016, Fabric Development and Pore-Throat reduction in a Mass-Transport Deposit in the Jubilee Gas Field, Eastern Gulf of Mexico: Consequences for the Sealing Capacity of MTDs, *in* G. Lamarche et al., eds., Submarine Mass Movements and their Consequences: Cham, Springer International Publishing, Advances in Natural and Technological Hazards Research, 27–37

Cardona, S., Wood, L. J., Dugan, B., Jobe, Z., & Strachan, L. J., Characterization of the Basal Shear Zone of the Rapanui Mass-Transport Deposit: Mount Messenger Formation, Taranaki Basin, New Zealand: Sedimentology, (in press)

Cecil, C. B., Hemingway, B. S., & Dulong, F. T., 2018, The Chemistry of Eolian Quartz Dust and the Origin of Chert: Journal of Sedimentary Research, 88(6), 743–752

Chiarella, D., & Longhitano, S. G., 2012, Distinguishing Depositional Environments In Shallow-Water Mixed, Bio-Siliciclastic Deposits On the Basis Of The Degree Of Heterolithic Segregation (Gelasian, Southern Italy) : Journal of Sedimentary Research, 82(12), 969–990

Chiarella, D., Longhitano, S. G., & Tropeano, M., 2017, Types of mixing and heterogeneities in siliciclastic-carbonate sediments: Marine and Petroleum Geology, 88, 617–627

Covault, J. A., Normark, W. R., Romans, B. W., & Graham, S. A., 2007, Highstand fans in the California borderland: The overlooked deep-water depositional systems: Geology, 35, 783-786

Crosby, C. B., Pigott, J. D., & Pigott, K. L., 2018, High resolution sequence stratigraphy of the Leonardian Bone Spring Formation, northern Delaware Basin, Eddy and Lea counties, New Mexico: Search and Discovery, 51464(51464), 1–138

Dakin, N., Pickering, K. T., Mohrig, D., & Bayliss, N. J., 2013, Channel-like features created by erosive submarine debris flows: Field evidence from the Middle Eocene Ainsa Basin, Spanish Pyrenees: Marine and Petroleum Geology, 41(1), 62-71

De Blasio, F.V., Elverhøi, A., Issler, D., Harbitz, C.B., Bryn, P. and Lien, R., 2005, On the dynamics of subaqueous clay rich gravity mass flows—the giant Storegga slide, Norway, in Ormen Lange–an Integrated Study for Safe Field Development in the Storegga Submarine Area: Elsevier, 179-186

De Blasio, F.V., Engvik, L., Harbitz, C.B., Elverhoi, A., 2006, High mobility of subaqueous debris flows and the lubricating-layer model: Norwegian Journal of Geology / Norsk Geologisk Forening, 86(3), 275–284

Dott, R. H., 1963, Dynamics of Subaqueous Gravity Depositional Processes: AAPG Bulletin, v. 47, no. 1, 104–128

Driskill, B., Pickering, J., & Rowe, H., 2018, Interpretation of High Resolution XRF data from the Bone Spring and Upper Wolfcamp, Delaware Basin, USA, Unconventional Resources Technology Conference, 2861–2888

Dunham, R. J., 1962, Classification of carbonate rocks according to depositional texture. Classification of Carbonate Rocks: American Association of Petroleum Geologists Memoir, 108–121

Eggenhuisen, J. T., McCaffrey, W. D., Haughton, P. D. W., Butler, R. W. H., Moore, I., Jarvie, A., & Hakes, W. G., 2010, Reconstructing large-scale remobilisation of deep-water deposits and its impact on sand-body architecture from cored wells: The Lower Cretaceous Britannia Sandstone Formation, UK North Sea: Marine and Petroleum Geology, 27(7), 1595–1615

Elverhoi, A., Harbitz, C.B., Dimakis, P., Mohrig, D., Marr, J. and Parker, G., 2000. On the dynamics of subaqueous debris flows: Oceanography, 13(3), 109-117.

Eyles, C.H., Eyles, N., 2000, Subaqueous mass flow origin for Lower Permian diamictites and associated facies of the Grant Group, Barbwire Terrace, Canning Basin, Western Australia: Sedimentology, 47, 343-356

Fisher, R. V., 1983, Flow transformations in sediment gravity flows: Geology, 11(5), 273–274

Fischer, A.G., and M. Sarnthein, 1988, Airborne silts and dune-derived sands in the Permian of the Delaware Basin: Journal of Sedimentary Petrology, v. 58, 637-643

Fitchen, W.M., 1997, Lower Permian sequence stratigraphy of the western Delaware Basin Margin, Sierra Diablo, West Texas, [PhD dissertation]: University of Texas at Austin, 263 p.

Folk, R.L., 1954, The distinction between grain size and mineral composition in sedimentary-rock nomenclature: The Journal of Geology, 62(4), 344-359

Folk, R.L., 1980, Petrology of sedimentary rocks: Hemphill Publishing Company

Gardner, M. H., and M. D. Sonnenfeld, 1996, Stratigraphic changes in facies architecture of the Permian Brushy Canyon Formation in Guadalupe Mountains National Park, west Texas, *in* W. D. DeMis and A. G. Cole, eds., The Brushy Canyon Play in outcrop and subsurface: Concepts and examples: Midland, Texas: Permian Basin Section SEPM Publication 96-38, 17–40

Gardner, M.H., Borer, J.M., Romans, B.W., Baptista, N., Kling, E.K., Hanggoro, D., Melick, J.J., Wagerle, R.M., Dechesne, M., Carr, M.M., Amerman, R., Atan, S., 2008, Stratigraphic Models for Deep-Water Sedimentary Systems, *in* Answering the Challenges of Production from DW Reservoirs: Analogues and Case Histories to Aid a New Generation: Gulf Coast Section of SEPM Annual Conference, Houston, Texas

Gómez-Pérez, I., Fernández-Mendiola, P. A., & García-Mondéjar, J., 1999, Depositional architecture of a rimmed carbonate platform (Albian, Gorbea, western Pyrenees) : Sedimentology, 46(2), 337-356

Grosheny, D., Ferry, S., & Courjault, T., 2015, Progradational patterns at the head of single units of base-of-slope, submarine granular flow deposits (“Conglomérats des Gas”, Coniacian, SE France): Sedimentary Geology, 317, 102-115

Hampson, G. J., 2016, Towards a sequence stratigraphic solution set for autogenic processes and allogenic controls: Upper Cretaceous strata, Book Cliffs, Utah, USA: Journal of the Geological Society, 173(5), 817–836

Harman, C. A., 2011, Quantified Facies Distribution and Sequence Geometry of the Yates Formation, Slaughter Canyon, New Mexico, [PhD dissertation]: University of Texas at Austin, 137 p.

Harris, M. T., 1987, Sedimentology of the Cutoff Formation (Permian), western Guadalupe Mountains, west Texas: New Mexico Geology, (November), 74–79

Harris, M.T., 2000, Members for the Cutoff Formation, western escarpment of the Guadalupe Mountains, West Texas: Smithsonian Contributions to the Earth Sciences, 32, 102-122

Harris, A.D., Baumgardner, S.E., Sun, T. and Granjeon, D., 2018, A poor relationship between sea level and deep-water sand delivery: Sedimentary Geology, 370, 42-51

Haughton, P., Davis, C., McCaffrey, W., & Barker, S., 2009, Hybrid sediment gravity flow deposits - Classification, origin and significance: Marine and Petroleum Geology, 26, 1900-1918

Hayes, P. T., 1964, Geology of the Guadalupe Mountains, New Mexico: U. S. Geological Survey Professional Paper, (446), 69 pp.

Hill, C.A., 1996, Geology of the Delaware Basin Guadalupe, Apache, and Glass Mountains, New Mexico and West Texas: Permian Basin Section of the Society of Economic Paleontologists and Mineralogists Publication 96-39, 480

Hills, J.M., 1984, Sedimentation, Tectonism, and Hydrocarbon Generation in Delaware Basin, West Texas and Southeastern New Mexico: American Association of Petroleum Geologists Bulletin, v. 68, No. 3 (March 1984), 250-267

Hu, N., D.F. Stockli, G. Sharman, H.S. Hamlin, J. Covault, 2018, Provenance of Depositional Controls on Reservoir Quality of the Lower Permian (Leonardian) Spraberry Formation, Midland Basin, TX, American Association of Petroleum Geologists Abstract

Hubbard, S. M., Romans, B. W., & Graham, S. A., 2008, Deep-water foreland basin deposits of the Cerro Toro Formation, Magallanes basin, Chile: Architectural elements of a sinuous basin axial channel belt: Sedimentology, 55(5), 1333–1359

Hurd, G.S., 2016, Revised stratigraphic framework for the Cutoff Formation and implications for deepwater systems modified by large-scale inflections in slope angle below the shelf break, [PhD dissertation]: University of Texas at Austin, 275 p.

Hurd, G. S., Kerans, C., Fullmer, S., & Janson, X., 2016, Large-Scale Inflections in Slope Angle Below the Shelf Break: A First Order Control On the Stratigraphic Architecture of Carbonate Slopes: Cutoff Formation, Guadalupe Mountains National Park, West Texas, U.S.A: Journal of Sedimentary Research, 86(4), 336–362

Hurd, G. S., Kerans, C., Frost, E. L., Simo, J. A., & Janson, X., 2018, Sediment gravity-flow deposits and three-dimensional stratigraphic architectures of the linked Cutoff, upper Bone Spring, and upper Avalon-system, Delaware Basin: AAPG Bulletin, 102(9), 1703–1737

Jablonská, D., Di Celma, C. N., Alsop, G. I., & Tondi, E., 2018, Internal architecture of mass-transport deposits in basinal carbonates: A case study from southern Italy: Sedimentology, 65(4), 1246–1276

James, N.P., Bone, Y., von der Borch, C.C., Gostin, V.A., 1992, Modern carbonate and terrigenous clastic sediments on a cool water, high energy, mid-latitude shelf: Lacepede, southern Australia: Sedimentology, 39(5), 877–903

Janocko, M., Nemec, W., Henriksen, S., & Warchoł, M., 2013,The diversity of deep-water sinuous channel belts and slope valley-fill complexes: Marine and Petroleum Geology, 41(1), 7–34

Janson, X., Kerans, C., Loucks, R., Marhx, M.A., Reyes, C. and Murguia, F., 2011, Seismic architecture of a Lower Cretaceous platform-to-slope system, Santa Agueda and Poza Rica fields, Mexico: AAPG bulletin, 95(1), 105-146

Jo., A., Eberli, G.P., Grasmueck, M., 2015, Margin collapse and slope failure along southwestern Great Bahama Bank: Sedimentary Geology, 317, 43-52

Katz, D. A., Playton, T., Bellian, J., Harrison, C., & Maharaja, A., 2010, Slope Heterogeneity and Production Results in a Steep-sided Upper Paleozoic Isolated Carbonate Platform Reservoir, Karachaganak Field, Kazakhstan, *in* SPE Caspian Carbonates Technology Conference: Society of Petroleum Engineers, 1-7

Kenter, J., 1990, Carbonate platform flanks : slope angle and sediment fabric Carbonate platforms have been the focus of increasing: Sedimentology, 37, 777–794

Kenter, J. A. M., & Schlager, W., 1989, A comparison of shear strength in calcareous and siliciclastic marine sediments: Marine Geology, 88(1–2), 145–152

Kerans, C., Kempter, K., 2002, Hierarchical stratigraphic analysis of a carbonate platform, Permian of the Guadalupe Mountains: American Association of Petroleum Geologists Datapages Discovery Series, no. 5, CD ROM

Kerans, C., W.M. Fitchen, M.H. Gardner, and B.R. Wardlaw, 1993, A contribution to the evolving stratigraphic framework of middle Permian strata of the Delaware Basin, Texas and New Mexico, *in*, Carlsbad Region (New Mexico and West Texas), Love, D.W., Hawley, J.W., Kues, B.S., Austin, G.S., Lucas, S.G., eds., New Mexico Geological Society 44th Annual Fall Field Conference Guidebook, 44, 175-84

Kertznus, V. and Kneller, B., 2009, Clinoform quantification for assessing the effects of external forcing on continental margin development: Basin Research, 21(5), 738-758

King, P.B., 1948, Geology of the southern Guadalupe Mountains, Texas: USGS Professional Paper 215, 183 pp.

Kirkby, K.C., 1982, Deposition, erosion and diagenesis of the upper Victorio Peak Formation (Leonardian), southern Guadalupe Mountains, West Texas, [MSc thesis]: Madison, University of Wisconsin, 165 p.

Kvale, E. P., & Rahman, M.W., 2017, Depositional Facies and Organic Content of Upper Wolfcamp Formation (Permian) Delaware Basin and Implications for Sequence Stratigraphy and Hydrocarbon Source, Unconventional Resources Technology Conference

Lazar, O. R., Bohacs, K. M., Macquaker, J. H. S., Schieber, J., & Demko, T. M., 2015, Capturing Key Attributes of Fine-Grained Sedimentary Rocks In Outcrops, Cores, and Thin Sections: Nomenclature and Description Guidelines: Journal of Sedimentary Research, 85(3), 230–246

Li, S., Yu, X., Li, S., & Giles, K. A., 2015, Role of sea-level change in deep water deposition along a carbonate shelf margin, Early and Middle Permian, Delaware Basin: implications for reservoir characterization: Geologica Carpathica, 66(2), 99–116

Lowe, D.R., 1982, Sediment gravity flows: II. Depositional models with special reference to the deposits of high-density turbidity currents: Journal of Sedimentary Petrology, 52, 279–297

Madof, A. S., Harris, A. D., & Connell, S. D., 2016, Nearshore along-strike variability: Is the concept of the systems tract unhinged? : Geology, 44(4), 315–318

Mazzanti P., De Blasio F.V., 2010, Peculiar Morphologies of Subaqueous Landslide Deposits and Their Relationship to Flow Dynamics. In: Mosher D.C. et al. (eds) Submarine Mass Movements and Their Consequences: Advances in Natural and Technological Hazards Research, 28, 141-152

McDaniel, P.N. and Pray, L.C., 1967, Bank to basin transition in the Permian (Leonardian) Carbonates, Guadalupe Mountains, Texas: American Association of Petroleum Geologists Bulletin, v. 51, 474

Milliken, K.L., 2014. A Compositional Classification For Grain Assemblages In Fine-Grained Sediments and Sedimentary Rocks: Journal of Sedimentary Research, 84, 1185–1199

Mitchum, R. M., Vail, P. R., & Thompson, S., 1977, Seismic Stratigraphy and Global Changes of Sea Level, Part 2: The Depositional Sequence as a Basic Unit for Stratigraphic Analysis: Section 2. Application of Seismic Reflection Configuration to Stratigraphic Interpretation. Seismic Stratigraphy: Applications to Hydrocarbon Exploration: AAPG Memoir 26, 53–62

Montgomery, S.L., 1997a, Permian Bone Spring Formation: Sandstone Play in the Delaware Basin Part I: Slope: American Association of Petroleum Geologists Bulletin, v. 81, No. 8 (August 2017), 1239-1258

Montgomery, S. L., 1997b, Permian Bone Spring formation: Sandstone play in the Delaware basin, part II - Basin: AAPG Bulletin, v. 81, no. 9, 1423-1434

Moscardelli, L., & Wood, L., 2008, New classification system for mass transport complexes in offshore Trinidad: Basin Research, 20(1), 73–98

Moscardelli, L., & Wood, L., 2016, Morphometry of mass-transport deposits as a predictive tool: Bulletin of the Geological Society of America, 128(1–2), 47–80

Mulder, T., E. Ducassou, G. P. Eberli, V. Hanquiez, E. Gonthier, P. Kindler, M. Principaud et al., 2012, New insights into the morphology and sedimentary processes along the western slope of Great Bahama Bank: Geology, v. 40, no. 7, 603–606

Nance, H.S., Rowe, H., 2015, Eustatic controls on stratigraphy, chemostratigraphy, and water mass evolution preserved in a Lower Permian mudrock succession, Delaware Basin, west Texas, USA: Interpretation, v. 3, No. 1 (February 2015), SH11-SH25

Nemec, W., 1990, Aspects of sediment movement on steep delta slopes: Special Publication Int. Ass. Sed., 10, 20-73

Permian Stratigraphy, Delaware to Midland Stratigraphic Correlation. https://www.sec.gov/Archives/edgar/data/1658566/000110465916143354/g155425mmi049.gif (May 2019).

Playton, T.E., Janson, X., Kerans, C., James, N.P. and Dalrymple, R.W., 2010, Carbonate slopes, *in* James and Dalrymple 2010, Facies models 4, 449-476

Playton, T. E., & Kerans, C., 2018, Architecture and genesis of prograding deep boundstone margins and debris-dominated carbonate slopes: Examples from the Permian Capitan Formation, Southern Guadalupe Mountains, West Texas: Sedimentary Geology, 370, 15-41

Poole, F.G., Perry Jr., W.J., Madrid, R.J., Amaya-Martinez, R., 2005, Tectonic synthesis of the Ouachita-Marathon-Sonora orogenic margin of southern Laurentia: Stratigraphic and structural implications for timing of deformational events and plate-tectonic model, *in*, Anderson, T.H., Nourse, J.A., McKee, J.W., and Steiner, M.B., eds., The Mojave-Sonora megashear hypothesis: Development, assessment, and alternatives, Geological Society of America Special Paper 393, 543-596

Prather, B. E., O'Byrne, C., Pirmez, C., & Sylvester, Z., 2017, Sediment partitioning, continental slopes and base-of-slope systems: Basin Research, 29 (3), 394-416

Presley, M.W., 1987, Evolution of Permian evaporite basin in Texas Panhandle: American Association of Petroleum Geologists Bulletin, v. 71, 167-190

Principaud, M., Mulder, T., Gillet, H., & Borgomano, J., 2015, Large-scale carbonate submarine mass-wasting along the northwestern slope of the Great Bahama Bank (Bahamas): Morphology, architecture, and mechanisms: Sedimentary Geology, 317, 27–42

Resor, P. G., & Flodin, E. A., 2010, Forward modeling synsedimentary deformation associated with a prograding steep-sloped carbonate margin: Journal of Structural Geology, 32(9), 1187–1200

Rich, J.L., 1951. Three critical environments of deposition, and criteria for recognition of rocks deposited in each of them: Geological Society of America Bulletin, 62(1), 1-20.

Romans, B. W., Castelltort, S., Covault, J. A., Fildani, A., & Walsh, J. P., 2016, Environmental signal propagation in sedimentary systems across timescales: Earth-Science Reviews, 153, 7-29

Ross, W.C., Halliwell, B.A., May, J.A., Watts, D.E. and Syvitski, J.P.M., 1994, Slope readjustment: a new model for the development of submarine fans and aprons: Geology, 22(6), 511-514

Salazar, M., Moscardelli, L., & Wood, L., 2016, Utilising clinoform architecture to understand the drivers of basin margin evolution: a case study in the Taranaki Basin, New Zealand: Basin Research, 28(6), 840–865

Saller, A.H., J.W. Barton, and R.E. Barton, 1989, Slope sedimentation associated with a vertically building shelf, Bone Spring Formation, Mescalero Escarpe field, southeastern New Mexico, *in*, P.D. Crevello, J.J. Wilson, J.F. Sarg, and J.F. Read, eds., Controls on carbonate platform and basin development, Society of Economic Paleontologists and Mineralogists, 275-288

Sarg, J.F. and Lehmann, P.J., 1986, Lower-middle Guadalupian facies and stratigraphy, San Andres/Grayburg Formations, Permian Basin, Guadalupe Mountains, New Mexico, *in*, Moore, G.E., Wilde, G.L., and Sarg, J.F., eds., Lower and middle Guadalupian facies, stratigraphy, and reservoir geometries: San Andres/Grayburg Formations, Guadalupe Mountains, New Mexico and Texas: Society of Economic Paleontologists and Mineralogists, Permian Basin Section, Symposium and Guidebook, v. 86-25

Sarg, J.F., 1988, Carbonate Sequence Stratigraphy. Sea-Level Changes – An Integrated Approach: SEPM Special Publication, 42, 155-181

Sarg, J.F., Markello, J.R., Weber, L.J., 1999, The second-order cycle, carbonate-platform growth, and reservoir, source, and trap prediction: Society of Economic Paleontologists and Mineralogists Special Publication No. 63, 11-34

Schlager, W., & Camber, O., 1986, Submarine slope angles, drowning unconformities, and self-erosion of limestone escarpments: Geology, 14(9), 762–765

Schwartz, K.M., Meier, H., Star, A., Stolte, N., 2018, Review of the First Bone Spring Hybrid Play in the Delaware Basin, West Texas and Southeast New Mexico, Unconventional Resources Technology Conference

Shanley, K. W., & McCabe, P. J., 1994, Perspectives on the sequence stratigraphy of continental strata: American Association of Petroleum Geologists Bulletin, 78(4), 544–568

Shumaker, L.E., Jobe, Z.R. and Graham, S.A., 2017, Evolution of submarine gullies on a prograding slope: Insights from 3D seismic reflection data: Marine Geology, 393, 35-46

Silver, B.A., Todd, G.T., 1969, Permian Cyclic Strata, Northern Midland and Delaware Basins, West Texas and Southeastern New Mexico: American Association of Petroleum Geologists Bulletin, v. 53, No. 11 (November 1969), 2223-2251

Sonnenfeld, M. D., 1991, Anatomy of offlap in a shelf-margin depositional sequence: upper San Andres Formation (Permian, Guadalupian), Last Chance Canyon, Guadalupe Mountains, New Mexico, [M.S. thesis]: Colorado School of Mines, 296 p.

Soreghan, G. S., & Soreghan, M. J., 2013, Tracing Clastic Delivery To the Permian Delaware Basin, U.S.A.: Implications For Paleogeography and Circulation In Westernmost Equatorial Pangea: Journal of Sedimentary Research, 83(9), 786–802

Soto-Kerans, G.M., X. Janson, D.F. Stockli, J. Covault, 2018, Provenance Analysis of Permian (Guadalupian) Deposits: Implications for Sediment Routing and Stratal Geometry, Delaware Basin, TX: American Association of Petroleum Geologists Abstract

Stanesco, J.D., 1991, Sedimentology and depositional environments of the lower Permian Yeso Formation, northwestern New Mexico (No. 1808) : US Department of the Interior, US Geological Survey, M1-M12

Stevenson, C. J., Jackson, C. A.-L., Hodgson, D. M., Hubbard, S. M., & Eggenhuisen, J. T., 2015, Deep-Water Sediment Bypass: Journal of Sedimentary Research, 85(9), 1058–1081

Stow, D.A.V., 1984, Anatomy of debris-flow deposits: Init. Rep. Deep Sea Drilling Project, 75, 801-807

Stow, D. A. V., 1986, Deep clastic seas, in H. G. Reading, ed., Sedimentary Environments and Facies: Oxford, Blackwell Scientific, 399–444

Strachan, L. J., 2002, Geometry to genesis: a comparative field study of slump deposits and their modes of formation: [PhD dissertation]: University of Cardiff, 409 p.

Sultan, N., Cochonat, P., Canals, M., Cattaneo, A., Dennielou, B., Haflidason, H., Laberg, J.S., Long, D., Mienert, J., Trincardi, F. and Urgeles, R., 2004, Triggering mechanisms of slope instability processes and sediment failures on continental margins: a geotechnical approach: Marine Geology, 213(1-4), 291-321

Sylvester, Z., Deptuck, M.E., Prather, B.E., Pirmez, C., and O’Byrne, C., 2012, Seismic stratigraphy of a shelf-edge delta and linked submarine channels in the northeastern Gulf of Mexico: Society of Economic Paleontologists and Mineralogists Special Publication No. 99, 31-59

Talling, P.J., D.G. Masson, E.J. Sumner, and G. Malgesini, 2012, Subaqueous sediment density flows: Depositional processes and deposit types: Sedimentology, v. 59, 1937-2003

Tassy, A., Crouzy, E., Gorini, C., Rubino, J. L., Bouroullec, J. L., & Sapin, F., 2015, Egyptian Tethyan margin in the Mesozoic: Evolution of a mixed carbonate-siliciclastic shelf edge (from Western Desert to Sinai): Marine and Petroleum Geology, 68(March 2018), 565–581

Thompson, M., Desjardins, P., Pickering, J., Driskill, B., 2018, An Integrated View of the Petrology, Sedimentology, and Sequence Stratigraphy of the Wolfcamp Formation, Delaware Basin, Texas, Unconventional Resources Technology Conference

Tribovillard. N., T.J. Algeo, T. Lyons, A. Riboulleau, 2006, Trace metals as paleoredox and paleoproductivity proxies: An update: Chemical Geology (2006), 232, 12-32

Tripsanas, E.K., Piper, D.J., Jenner, K.A. and Bryant, W.R., 2008. Submarine mass-transport facies: new perspectives on flow processes from cores on the eastern North American margin: Sedimentology, 55(1), 97-136

Trower, E.J., Ganti, V., Fischer, W.W. and Lamb, M.P., 2018, Erosional surfaces in the Upper Cretaceous Castlegate Sandstone (Utah, USA): Sequence boundaries or autogenic scour from backwater hydrodynamics?: Geology, 46(8), 707-710

Vail, P. R., 1987, Seismic stratigraphy interpretation procedure: Atlas of Seismic Stratigraphy, 27 (2), 1–10

Vanneste, M., Sultan, N., Garziglia, S., Fredrik, C., & Heureux, J. L., 2014, Sea floor instabilities and sediment deformation processes: The need for integrated, multi-disciplinary investigations: Marine Geology, 352, 183–214

Zelt, F. B., and C. R. Rossen, 1995, Geometry and continuity of deep-water sandstones and siltstones, Brushy Canyon Formation (Permian) Delaware Mountains, Texas, *in* K. T. Pickering, R. N. Hiscott, N. H. Kenyon, F. Ricci-Luchi, and R. D. A. Smith, eds., Atlas of

Deep Water Environments—Architectural Style in Turbidite Systems: Chapman and Hill, London, p. 167-183

FIGURE CAPTIONS

Figure 1: Overview map of the Permian outcrops in and around Guadalupe Mountains National Park (GMNP), west Texas (modified from King, 1948). **A)** Geologic map of GMNP. Black box denotes Figure 1B location. White line A-A' indicates location of cross-section in Figure 2. Inset map shows Permian Basin paleogeography with GMNP denoted as a red box along the western margin of the Delaware basin, blue line indicates Figure 23 seismic line; HV = Hovey Channel, SS = San Simon Channel, SH = Sheffield Channel. **B)** Study area focusing on Leonardian-aged outcrops. Red dashed line indicates 3-D model shown in Figure 3, and red solid lines highlight interpreted outcrop exposures shown in Figures 8, 10, 12, 14, A2, and A3. Dotted tan line marks Shumard Trail.

Figure 2: Stratigraphic section (A-A') of the west face of Guadalupe Mountains National Park (modified from Kerans and Kempter, 2002). This study focuses on the Bone Spring (upper slope) and Victorio Peak (outer shelf) L5 and L6 sequences (red box). Outcrop-defined sequences shown in the stratigraphic column to the left compiled from Fitchen 1997, Sarg et al., 1999, Kerans and Kempter, 2002, Hurd et al., 2016, and this study. The stratigraphic section at right defines the basin terminology with inferred chronostratigraphic correlations to outcrops. Note the Bone Spring Fm. outcrops are interpreted to correlate to the basinal rocks referred to as the Middle Avalon Carbonate, Lower Avalon Shale, and some portion of the 1st Bone Spring Carbonate.

Figure 3: Stratigraphic Architecture of the outcropping Bone Spring Fm (see Supplementary Material for field-scale print). **A)** Plan view of 3D model with bedding attitudes. Contacts between Brushy Canyon, Cutoff, Upper Victorio Peak (UVP), and Lower Victorio Peak (LVP) formations shown. **B)** 3D digital outcrop model of the stratigraphic architecture of the Bone Spring Fm. Depositional elements, lithology variability, stratigraphic surfaces, and dip direction displayed. Ten clinothems (orange numbers) are bounded by nine slope detachment surfaces (black lines and blue numbers).

Figure 4: Facies analysis of Bone Spring Fm. deposits. **A)** Facies diagram displaying eight facies with generalized XRF readings. Facies are grouped based on composition and depositional process. **B)** Ternary diagram displaying XRF data color-coded by carbonate- mixed- or siliciclastic- dominant facies (blue, orange, black, respectively). Axes truncated for detail. **C)** Schematic of naming scheme used in this study with facies projected.

Figure 5: Facies pictures from outcrop (upper photo) and thin section (lower photo). **A)** Facies 1 thin-bedded laminated lime mudstone. Pencil is marking ripples. Thin section of Facies 1 is predominantly lime mudstone, but detrital quartz grains are present. **B)** Facies 2, thin to thick-bedded deformed lime mudstone with lines indicating deformation. Thin section of Facies 2 with deformation-induced calcite-cemented fractures with background facies identical to Facies 1. **C)** Facies 3, thick-bedded bioclastic lime wackestone to packstone. Thin section of Facies 3 shows an increase in mud content to the top interpreted as possible turbidity current. **D)** Facies 4, interbedded lime mudstone and bioclastic packstone with interbedded packstone indicated. Thin

section shows interbedded packstone beds with calcite cementation and lenticular to continuous nature. **E)** Facies 5, thick-bedded normal-graded bioclastic lime packstone to grainstone. Normal grading shown with finger placed on basal coarse-grain deposit. Thin section shows bryozoan (by), brachiopods (ba), and undifferentiated carbonate allochems with chert cement. **F)** Facies 6, thin-bedded laminated bioclastic quartz siltstone. Note different color and weathering pattern to Facies 1. Thin section shows noticeably higher detrital quartz present in comparison to Facies 1. **G)** Facies 7, thin-bedded laminated quartz lime mudstone. Interbedded with Facies 6 showing different weathering pattern. Note brown color in comparison to Facies 1. Thin section of Facies 7 with detrital quartz content less than Facies 6 but greater than Facies 1. **H)** Facies 8, thick-bedded bioclastic lime packstone to grainstone. Thin section of Facies 8 reveals bryozoan (by), sponge spicules (sp), rugose corals (co), brachiopods (ba), and unidentified carbonate material.

Figure 6: Facies Associations of the outcropping Bone Spring Fm. **A)** Facies Association 1: Upward-shoaling carbonate margin. Transition from Bone Spring Fm. (BS) to Victorio Peak Fm. (VP) facies indicated. **B)** Facies Association 2: Carbonate slope deposits with mass wasting. **C)** Facies Association 3: Submarine carbonate channel deposits. Mid-slope and shelf-edge settings shown. **D)** Facies Association 4: Upper-slope siliciclastic-dominant hemipelagic and sediment gravity flow deposits.

Figure 7: Photos of Facies Associations from the outcrop. **A)** Facies Association 1 (FA1): undeformed prograding slope with planar chert beds (dark colored rock). **B)** Discordant surface within FA2; note truncation of F1, with F2 overlying the surface. **C)** Facies Association 3 (FA3): upper-slope submarine channel facies (F5) cutting into slope deposits (F1). Erosional surfaces

shown in yellow. **D)** FA3: mid-slope submarine gully deposits show offset stacking and axis-to-margin fining. E) Facies Association 4 (FA4): Interbedding of siliciclastic-rich Facies 6 (fissile, grey, recessive) and mixed-composition Facies 7 (tan colored, more resistant) on the upper slope.

Figure 8: Stratigraphic Architecture of the north wall of Shumard Canyon (see Supplementary Material for field-scale print). SDS and clinothems labeled by blue and orange circles, respectively. Note the prominent dip-azimuth change in Clinothem 8 (from eastward to southward dips), coincident with a concentration of mass wasting deposits and FA3 channel deposits. Numbered inset boxes correspond to Figure 9, where siliciclastic-dominant intervals (A), mass transport deposits (B), and discordant truncation surfaces (C, D) are highlighted. Arrow symbols represent dip direction (where North is up). Compensationally stacked channels shown in Figure 7D indicated in black. Location of XRF transects 1-3 shown in blue.

Figure 9: Architectural features visible on Shumard north wall. **A)** Prominent SDS (3 and 4) with dip attitude and lithology changes across surfaces. Above SDS 3, siliciclastic-beds dominate and are truncated by SDS 4. Figure 16D and 17A indicated in black boxes. Arrow and numerical value represent dip azimuth and magnitude; North corresponds to Figure 8. **B)** SDS 6 with a 5 m thick MTD sitting directly above the surface. Note debrites (db) and packstone beds (pb) with some preserved strata internally in the MTD (white lines) with the healing phase topography above the MTD. Geologist for scale. **C)** SDS 7 with truncation and dip attitude change in Facies 1. **D)** Discordant surface (red) within Clinothem 8, with ~15-20 m of overlying Facies 1 with a wedge geometry. Note the geologist for scale.

Figure 10: Stratigraphic Architecture of the south wall of Shumard Canyon (see Supplementary Material for field-scale print). SDS and clinothems labeled by blue and orange circles, respectively. The large submarine channel deposit is shown in blue (see Figure 7C for details). Inset boxes correspond to Figure 11. Note that the Shumard Trail passes directly through many key architectural features.

Figure 11: Architectural features visible on Shumard south wall. **A)** Large MTD overlying SDS 7. Figure 16C indicated in black box. **B)** MTD overlying SDS 6 shows multiple detachment surfaces (red) separating folded and faulted Facies 1 deposits. Note geologist for scale. **C)** FA4 in Clinothem 4 consists of interbedded siliciclastic (F6) and carbonate (F7) deposits.

Figure 12: Stratigraphic Architecture of the north wall of Bone Canyon (see Supplementary Material for field-scale print). The Cutoff Fm. here has been eroded from the overlying Brushy Canyon Fm. channel. SDS and clinothems labeled by blue and orange circles, respectively. Numbered inset boxes correspond to Figure 13, where sand beds and normal faults (A), SDS 8 (B), a 5-10-meter discordant surface (C), and a calciturbidite deposit (FA3) sitting on top of SDS 9 are highlighted. Note vertical fractures at the eastern side of the outcrop.

Figure 13: Architectural features visible on Bone north wall. **A1)** Interbedding of siliciclastic and carbonate beds (FA4) in Clinothem 4. **A2)** Post-depositional faulting. Faulting shown here is small and mostly antithetic to the primary escarpment-bounding fault to the west of the outcrop (Figure 1). Geologist in circle. **B)** SDS 8 showing dip attitude change, truncation, and similar facies on either side of the surface. Arrow and numerical value represent dip azimuth and

magnitude; North corresponds to Figure 12. Location of XRF transect 4 (Figure 21D) shown. Symbols represent XRF readings below (circle), along (square), and above (triangle) surface. **C)** Example of small-scale discordant surface in red. Surface is on the meter-scale, cuts through only 1-2 beds, with minimal dip change across the surface. **D)** SDS 9 with a calciturbidite (FA3) sitting above the surface and a dip attitude shift from below to above. Location of XRF transect 5 (Figure 21E) shown. Backpack indicated by circle.

Figure 14: Stratigraphic Architecture of the south wall of Bone Canyon (see Supplementary Material for field-scale print). SDS and clinothems labeled by blue and orange circles, respectively. Numbered inset boxes correspond to Figure 15, where a large mass transport deposit (A), bedding orientation change across SDS 8 (B), and SDS 9 with related mass wasting features (C) are highlighted. Figure 17B indicated. Note the Cutoff Fm. eroding into the Bone Spring Fm. (Hurd et al., 2016) and the overlying Brushy Canyon Fm. (Gardner et al., 2008).

Figure 15: Architectural features visible on Bone south wall. **A)** Large mass transport deposit that shows minimal internal deformation other than minor folding and a soft-sediment thrust fault shown in green. Arrow and numerical value represent dip azimuth and magnitude; North corresponds to Figure 14. **B)** A 40° dip azimuth change occurs across SDS 8, with FA2 both above and below the surface. The surface itself dips at 29/050. **C)** SDS 9 with overlying deformed Facies 2 MTDs, and other small-scale discordant surfaces (red surfaces) with variable F1 and F2. Note the Cutoff Fm. contact just above this surface, and the geologist for scale.

Figure 16: Scales of syn-sedimentary, intrastratal deformation observed in the Bone Spring Formation. **A1)** Deformed lime mudstone facies (F2) with micro-scale deformation. **A2)** Line drawing of figure A1. **B)** Meso-scale deformation. Debrite (F2) highlighted in red eroding into underlying strata. Note deformed chert beds within debrite. White lines indicate undeformed bedding below and above debrite. Location indicated in Figure 14. **C)** Meso-scale deformation. MTD sitting above SDS 7 erodes into underlying carbonate mudstone facies (F1). Some deformed strata and chert beds indicated by white lines. See location in Figure 11A. **D)** Meso-scale deformation within siliciclastic-dominant facies (F6). Deformed bedding in red with overlying undeformed bedding highlighted in white. Yellow lines indicate Cenozoic normal faults. See location in Figure 9A.

Figure 17: Examples of the various styles and characteristics of deformation deposits found on the Bone Spring outcrop. **A)** Creep deposit. Individual lamina set highlighted by white arrows shows micro-scale detachment and deformation but no failure at the bed-set (~ 1 m) scale. Note chert nodules mimic the primary bedding. Location indicated in Figure 9A. Pencil circled for scale. **B1)** Slump deposit. Two large (meso-scale) folds separated by decollement surfaces in red. Folded bedding in white. Compressional thrust faults in yellow below first fold. Location for B2 and B3 in boxed areas. Geologist for scale. Location of fold shown in Figure A.2. **B2)** Breccia at the base of lower fold. Arrow and white lines indicate brecciated basal zone. **B3)** Thin section image near base of lower fold. Fractures in white are calcite-filled. Matrix is an F1 lime mudstone. **C)** Debris flow deposit (debrite). Debrite truncates underlying undeformed strata in white. Note chert and mudstone clasts within debrite. Location in area B of Shumard Cyn. south

wall. **D)** Debris flow deposit displaying chaotic nature of chert and carbonate mudstone matrix. Geologist pointing at large chert nodule. Location on Bone Cyn. south wall.

Figure 18: Facies-based XRF results. A Calcium, Silicon, and Aluminum + Titanium ternary diagram shows a carbonate- mixed- and siliciclastic-domain that represent facies end-members in the Bone Spring Fm. A dashed line represents a continuum from the carbonate-domain to the siliciclastic-domain. Highlighted in blue, two hand samples identified as Facies 5 (i.e. calciturbidites) plot high in Silicon but deviate from the carbonate-to-siliciclastic trendline, indicating diagenetic chert present. This is confirmed in thin section (Figure 5E).

Figure 19: XRF transects through Shumard and Bone canyons. Results demonstrate terrigenous sediment is associated with slope detachment surfaces. The ‘x’ marks the first measurement with the stratigraphic path of the transects indicated by arrows (see Figure 13). Turquoise circles mark readings of clinothems below the SDS, turquoise squares represent SDS readings, and triangles represent clinothem readings above the SDS. Blue arrows highlight transect trends; gray symbols correspond to facies in Figure 18. **A)** transect 1 through SDS 4. This transect is located predominantly within the siliciclastic-domain. **B)** transect 2 through SDS 6. Transect located within the mixed- to carbonate-domain and shifts toward the siliciclastic-domain at the surface. **C-E)** transects 3-5 and SDS 7-9, respectively. Surface transects show same trend as transect 2 with a shift from the mixed-domain toward the siliciclastic-domain at the slope detachment surface.

Figure 20: Interpretive schematics of Leonardian margin associated with the Guadalupe Mountains National Park outcrops. **A)** Time step A. High A/S with high carbonate production and minimal siliciclastic input. Slope progrades and aggrades at different rates locally. **B)** Time step B. Detrital siliciclastic and argillaceous sediment introduced to the outer margin from a decrease in A/S. The increase in siliciclastic material weakens the slope and creates large-scale, shelf-attached failure. Large-scale failure creates slope detachment surfaces that are likely part of a larger clinoform surface (magenta surface). Surfaces are coeval with MTDs at the toe-of-slope and in the basin. **C)** Time step C. Further A/S decrease introduces large volumes of siliciclastic sediment to the outer margin and upper slope. Continued surface development as siliciclastic and argillaceous sediment bypass to the basin. **D)** Time step D. Return to high A/S with the slope prograding and aggrading over its relict topography creating a new clinothem. **E)** Schematic shelf-to-basin cross-section based on the slope reconstructions representing an ABDABCD time sequence. Red surfaces represent slope detachment surfaces and corresponding time-lines similar to those documented on the outcrop. The transitioning facies of Facies 5, 6, and 7 represent the expected proximal to distal transition. Red box represents outcrop-constrained portion of the schematic.

Figure 21: Slope inflection points may act as conduits for coarse-grained sediment. **A)** Line drawing of Shumard north wall (Figure 8) with dip azimuth readings (north is up). Orange arrows represent dip readings within Clinothems 1-7, while blue arrows represent readings in Clinothem 8. Note the calciturbidites and red discordant surfaces become more common near SDS 7. The large submarine channel deposit on Shumard south wall (Figure 10) also aligns with this region. **B)** Bedding attitude data from Shumard north wall. Colors correspond to location on

Figure A. Average dip azimuth shifts 90 degrees after SDS 7. **C)** Schematic of Shumard north wall with a local inflection point in the slope. This inflection point creates instability from over-sedimentation and the resultant failure scarps act as a conduits for coarse-grained turbidites to the basin.

Figure 22: Well-log correlations in the Permian Basin. **A)** 'Pancake model' interpretation of Bone Spring Fm. members in the Delaware and Midland Basins. Note that the shale and sand members of the Bone Spring are interpreted to be correlable across the entire Delaware Basin. Digital image from the web (Permian Stratigraphy). **B)** Alternative interpretation based on the results in this study. Note there is higher-order packages of high net-to-gross (N:G) sand and carbonate, but internally these members are heterogeneous with siliciclastic and carbonate sedimentation occurring simultaneously. Additionally, the Midland and Delaware Basins are not correlated, as they have different fill histories (Sarg, 1988, Sarg et al., 1999).

Figure 23: Predicting sub-seismic facies types from seismic-scale architecture. **A)** Unedited seismic line of the Delaware Basin shelf margin from Sarg (1988) and Sarg et al. (1999). Location shown in Figure 1A inset. Red box indicates location of part B. **B)** Interpreted seismic section of Leonardian and Guadalupian shelf-to-basin stratigraphy. The unit labeled Bone Spring Carbonate would roughly correlate to the upper section (L6) of the Bone Spring outcrops in the study area. Orange lines highlight clinoform geometries within the prograding carbonate package. The Lower Avalon represents a basinal siliciclastic wedge between L5 and L6 (Figure 2). **C1)** Photo and **C2)** line drawing of Shumard north, highlighting the similarity of scale and geometry of clinoforms to those seen in seismic.

Figure A.1: Location of six photopanels compiled along the outcrop shown here overlaying the 3D textured model.

Figure A.2: West wall of Shumard Canyon photopanel. Location of figures in text indicated. See Supplementary Material for field-scale print.

Figure A.3: West wall of Bone Canyon photopanel. Location of figures in text indicated. See Supplementary Material for field-scale print.

Table 1. Summary of descriptions and interpretations of lithofacies

Facies	Basin Naming Scheme (Lazar et al., 2015)	Mud Content Silt/clay type	Coarse-grain % Size Type	Si/Ca ratio (s/c)	Sedimentary Structures	Diagenetic Features	Depositional Process	Depositional Environment
F1 Thin-bedded laminate lime mudstone (Figure 5A)	Laminate calcareous siltstone	75-80% 60/40 Carbonate clay, argillaceous clay, carbonate grains, qz grains, organic matter, pyrite	20-25% vfs Carbonate and biogenic grains, crinoids, spicules, shell fragments, quartz	08/92 s/c<<1	>90% planar laminations (mm-scale beds) some evidence of soft-sediment deformation some bioturbation	Chert beds mostly planar (5-10 cm thick) or nodular, occurring every 10-20 cm Minor dolomitization Pyrite formation	Hemipelagic and sediment gravity flow	Hemipelagic deposits on the upper-slope with sediment gravity flow common
F2 Thin to thick-bedded deformed lime mudstone (Figure 5B)	Deformed calcareous siltstone	75-80% 60/40 Carbonate clay, argillaceous clay, carbonate grains, qz grains, organic	20-25% vfs Carbonate and biogenic grains, crinoids, spicules, shell fragments,	08/92 s/c<<1	Planar laminations Soft-sediment deformation: folding, fractures, fluid-escape, decollement surfaces Chaotic	Chert beds mimic bedding structure and can be folded, deformed, nodular, or planar Calcite-filled fractures Minor	Hemipelagic deposition with soft sediment deformation, slope creep, sediment gravity flow	Hemipelagic and sediment gravity flow slope deposits that have undergone deformation from high slope angles and/or high sediment supply

		matter, pyrite	quartz		bedding in places	dolomitization Pyrite formation		
F3 Thick-bedded bioclastic lime wackestone to packstone (Figure 5C)	Thick-bedded bioclastic lime siltstone to very fine sandstone	30% 70/30 Carb. and arg. clay, carbonate grains, qz grains, organic matter, pyrite 50% mud 50% sparite	70% vfs carbonate and biogenic grains, peloids, spicules, crinoids, shell fragments, bryozoan, brachiopods, qz grains	5/95 s/c<<1	Grading Laminations Some in-place production	Chert beds mostly nodular (5-10 cm thick), occurring every 30-40 cm	Hemipelagic and sediment gravity flow	Hemipelagic slope deposits that are proximal to the shelf margin relative to F1 and F2 and have experienced reworking from tidal, storm, or current forces
F4 Interbedded lime mudstone and bioclastic packstone (Figure 5D)	Interbedded calcareous siltstone and bioclastic very fine sandstone	70% Same as Facies 1	30% vfs Crinoids, spicules, peloids, shell fragments	08/92 s/c<<1	Packstone beds occur every 1-2 cm and are planar and continuous or lenticular Starved ripples Some bioturbation	Significant dolomitization and calcite cement in packstone beds	Hemipelagic deposition interbedded with sediment gravity flows (turbidity currents)	Slope sheet deposits of coarse-grained material (turbidites) coming off the shelf onto hemipelagic slope deposits

F5 Thick-bedded normal-graded bioclastic lime packstone to grainstone (Figure 5E)	Normal-graded bioclastic calcareous sandstone	15% 0% carbonate mud 100% sparite Silt-sized carbonate grains (shell frg., spicules) Sparite can reach 30% in some cases	85% Coarse (0.5-1mm in diameter) Carbonate and biogenic grains, crinoids, peloids, spicules, brach., bryo., bivalves, shell frg.	0/100 s/c<<1	Some normal grading and grain size segregation Patches of coarse grains Low-angle scours Amalgamation surfaces Continuous red surfaces	Siliceous cement (chert) Styolites	Sediment gravity flow (turbidity currents)	Calciturbidites on the shelf-margin and slope
F6 Thin-bedded laminate bioclast quartz siltstone (Figure 5F)	Laminate bioclast-rich siliceous siltstone	75-85% 70/30 Argillaceous clay (Al- and K-rich), qz, crinoids, peloids, shell frg. Minimal sparite	15-25% vfs Quartz, carbonate grains	75/25 s/c>1	Planar laminations ("flaggy" bedding) Ripples Scouring perpendicular to bedding	Iron oxidation and/or calcification of carbonate grains Minor dolomitization Chert absent	Hemipelagic and sediment gravity flow (turbidity currents) Possibly aeolian settling	Terrigenous hemipelagic deposition on the outer margin and reworked and transported by turbidity currents Possible reworking by thermohaline bottom currents
F7	Laminated quartz-rich	60-70%	30-40%	45/55	Planar	Chert beds mostly planar	Hemipelagic and sediment	Terrigenous hemipelagic

Thin-bedded laminated quartz lime mudstone (Figure 5G)	calcareous siltstone	50% mud and silt 50% sparite	vfs Some fs Mostly qz, some shell frg.	s/c~1	laminations Scouring perpendicular to bedding Minor soft-sediment deformation	(5-10cm thick) or nodular, occurring every 10-20 cm Minor dolomitization	gravity flow (turbidity currents) Possibly aeolian settling	deposition compositionally mixing with carbonate material on the outer margin and reworked and transported by turbidity currents Possible reworking by thermohaline bottom currents
F8 Thick-bedded bioclastic lime packstone to grainstone (Figure 5H)	Bioclastic lime very fine sandstone to sandstone	20-30% 0% mud 100% sparite	70-80% Coarse Range: vfs-pebble Crinoids, peloids, spicules, brach., bryo., sponges, bivalves, carbonate grains, shell frg., sparite grains	0/100 s/c<<1 No siliciclastic observed	None observed (in-place)	Chert beds mostly nodular (5-10 cm thick), occurring every 0.5-1 meter Dolomitization	Carbonate platform *in situ* growth Some tidal, storm, or current reworking	Outer shelf margin to upper-slope deposits Considered Lower Victorio Peak (King, 1948; Kirkby, 1982; Harris, 2000)

Figure 1

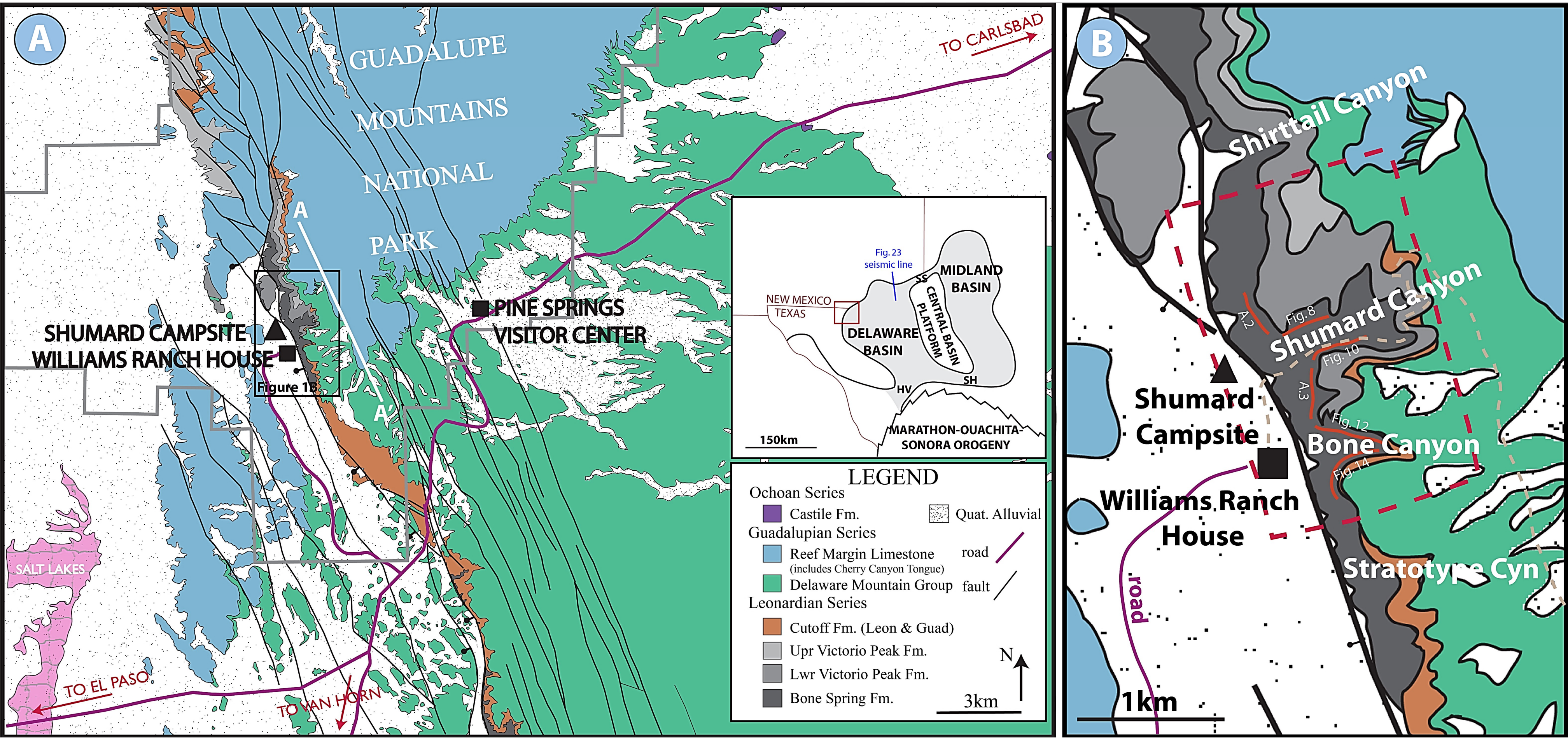
A
GUADALUPE
MOUNTAINS
NATIONAL
PARK
TO CARLSBAD
A
A'
PINE SPRINGS
VISITOR CENTER
SHUMARD CAMPSITE
WILLIAMS RANCH HOUSE
Figure 1B
SALT LAKES
TO EL PASO
TO VAN HORN
Fig. 23
seismic line
NEW MEXICO
TEXAS
MIDLAND
BASIN
DELAWARE
BASIN
CENTRAL BASIN
PLATFORM
SS
HV
SH
MARATHON-OUACHITA-
SONORA OROGENY
150km
LEGEND
Ochoan Series
Castile Fm.
Quat. Alluvial
Guadalupian Series
Reef Margin Limestone
(includes Cherry Canyon Tongue)
road
Delaware Mountain Group
fault
Leonardian Series
Cutoff Fm. (Leon & Guad)
Upr Victorio Peak Fm.
Lwr Victorio Peak Fm.
Bone Spring Fm.
N
3km
B
Shirttail Canyon
Shumard Canyon
Fig. 8
A.2
Fig. 10
A.3
Fig. 12
Fig. 14
Shumard
Campsite
Bone Canyon
Williams Ranch
House
Stratotype Cyn
road
1km

Figure 2

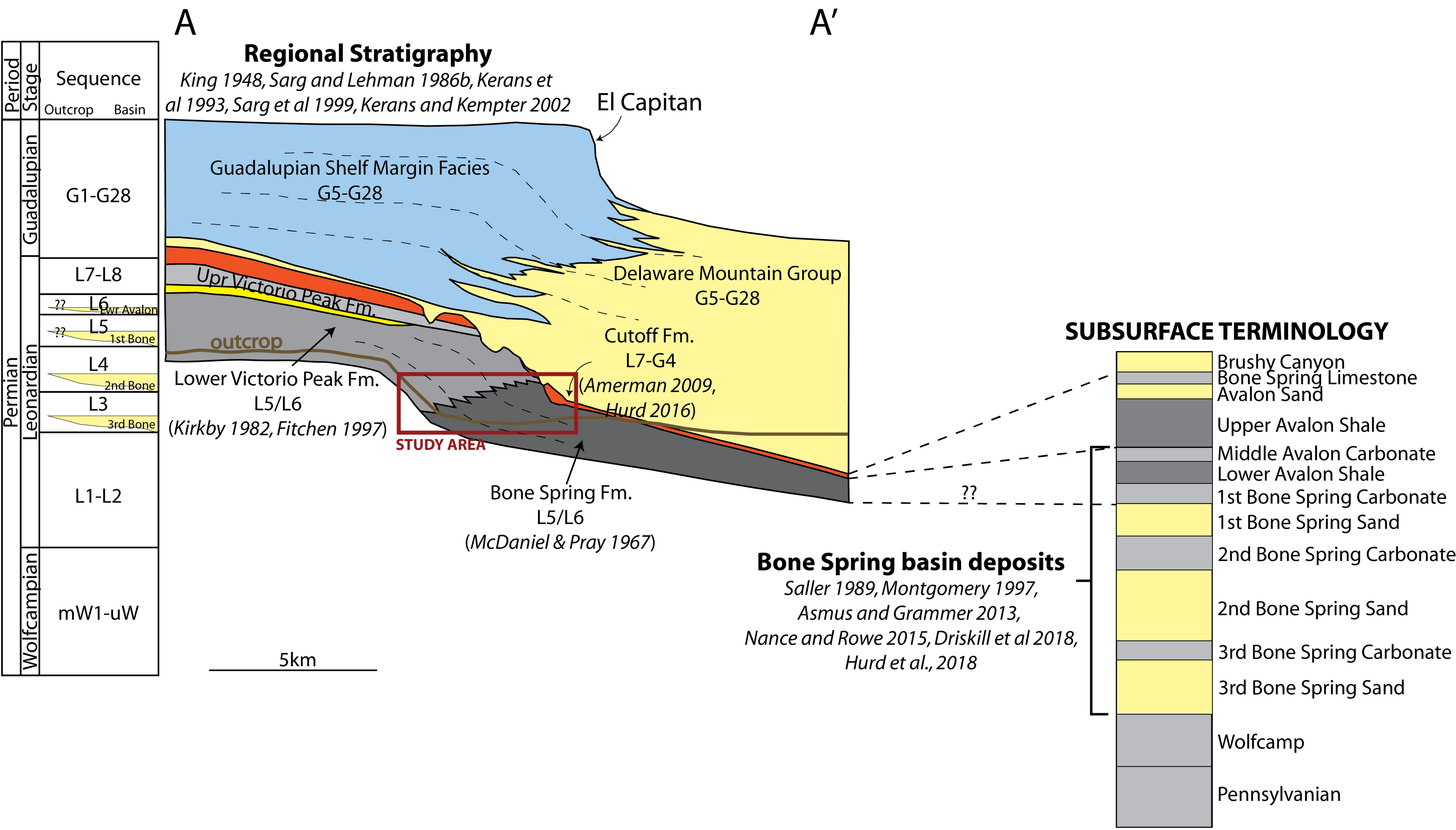

A
A'
Period
Stage
Sequence
Outcrop
Basin
Permian
Guadalupian
Leonardian
Wolfcampian
G1-G28
L7-L8
L6
Lwr Avalon
L5
1st Bone
L4
2nd Bone
L3
3rd Bone
L1-L2
mW1-uW
??
Regional Stratigraphy
King 1948, Sarg and Lehman 1986b, Kerans et al 1993, Sarg et al 1999, Kerans and Kempter 2002
El Capitan
Guadalupian Shelf Margin Facies
G5-G28
Upr Victorio Peak Fm.
outcrop
Delaware Mountain Group
G5-G28
Cutoff Fm.
L7-G4
(Amerman 2009, Hurd 2016)
Lower Victorio Peak Fm.
L5/L6
(Kirkby 1982, Fitchen 1997)
STUDY AREA
Bone Spring Fm.
L5/L6
(McDaniel & Pray 1967)
5km
SUBSURFACE TERMINOLOGY
Brushy Canyon
Bone Spring Limestone
Avalon Sand
Upper Avalon Shale
Middle Avalon Carbonate
Lower Avalon Shale
1st Bone Spring Carbonate
1st Bone Spring Sand
2nd Bone Spring Carbonate
2nd Bone Spring Sand
3rd Bone Spring Carbonate
3rd Bone Spring Sand
Wolfcamp
Pennsylvanian
??
Bone Spring basin deposits
Saller 1989, Montgomery 1997,
Asmus and Grammer 2013,
Nance and Rowe 2015, Driskill et al 2018,
Hurd et al., 2018

Figure 3a

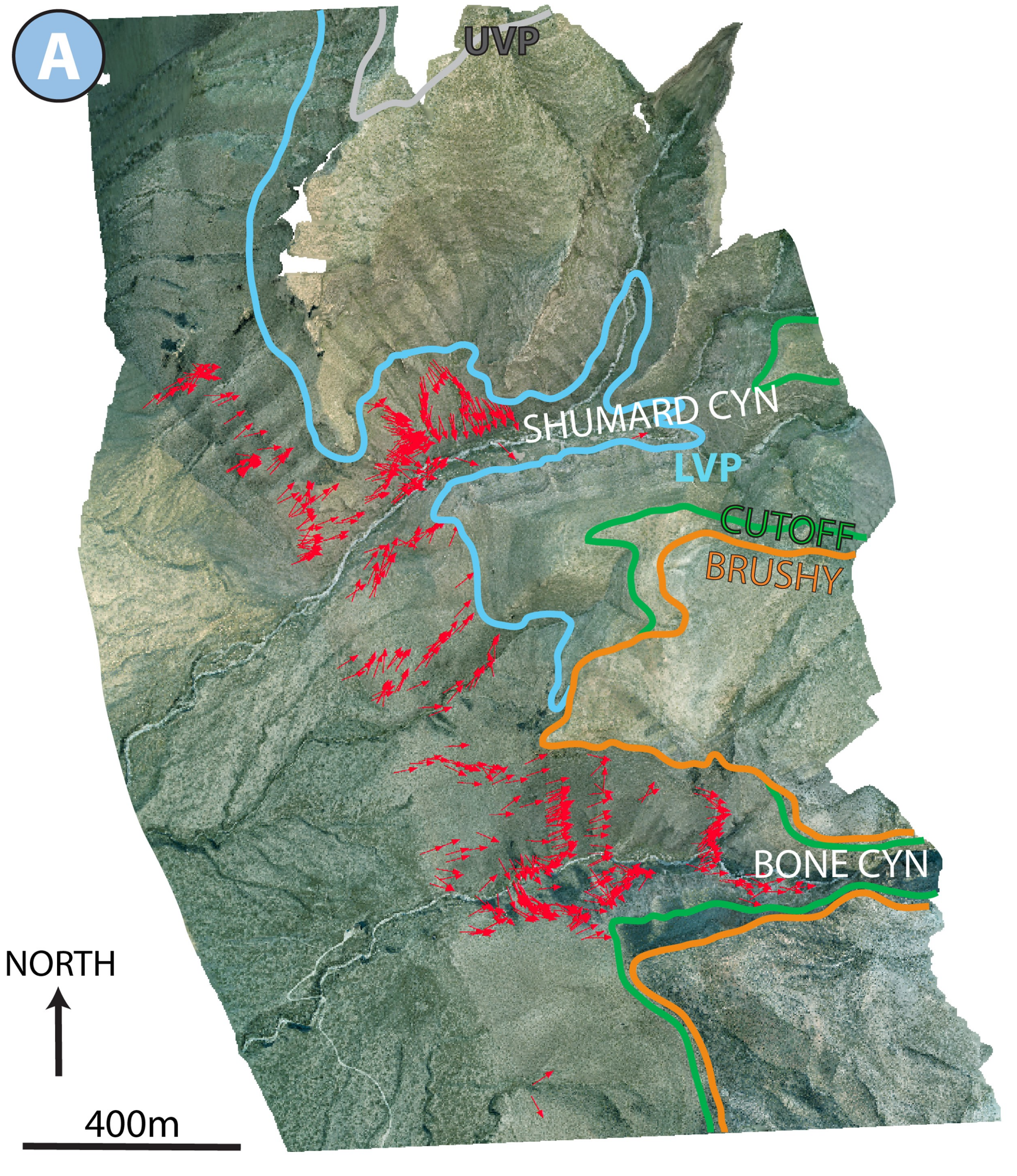

Figure 3b

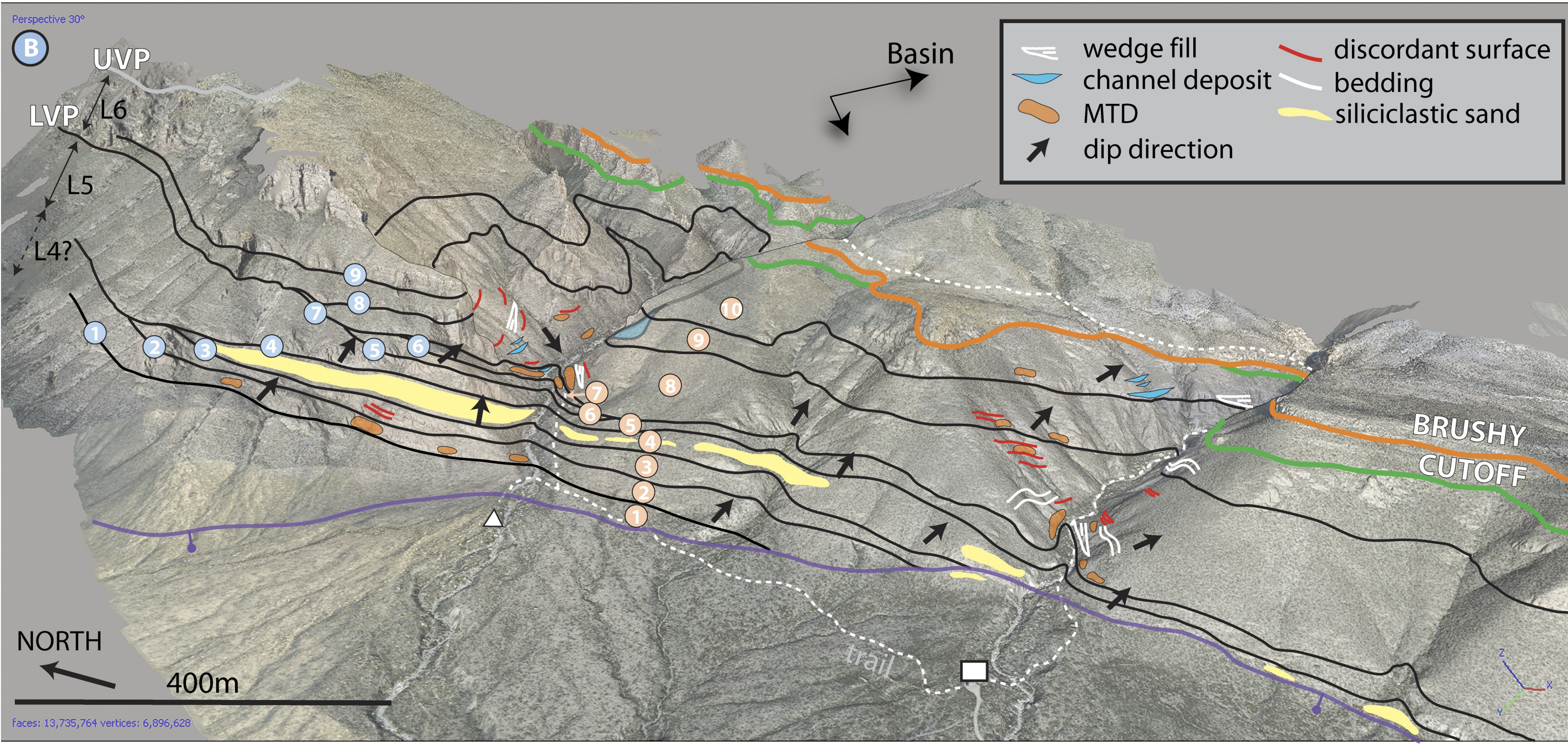

Perspective 30°
B
UVP
LVP
L6
L5
L4?
Basin
wedge fill
channel deposit
MTD
dip direction
discordant surface
bedding
siliciclastic sand
BRUSHY
CUTOFF
trail
NORTH
400m
faces: 13,735,764 vertices: 6,896,628

Figure 4

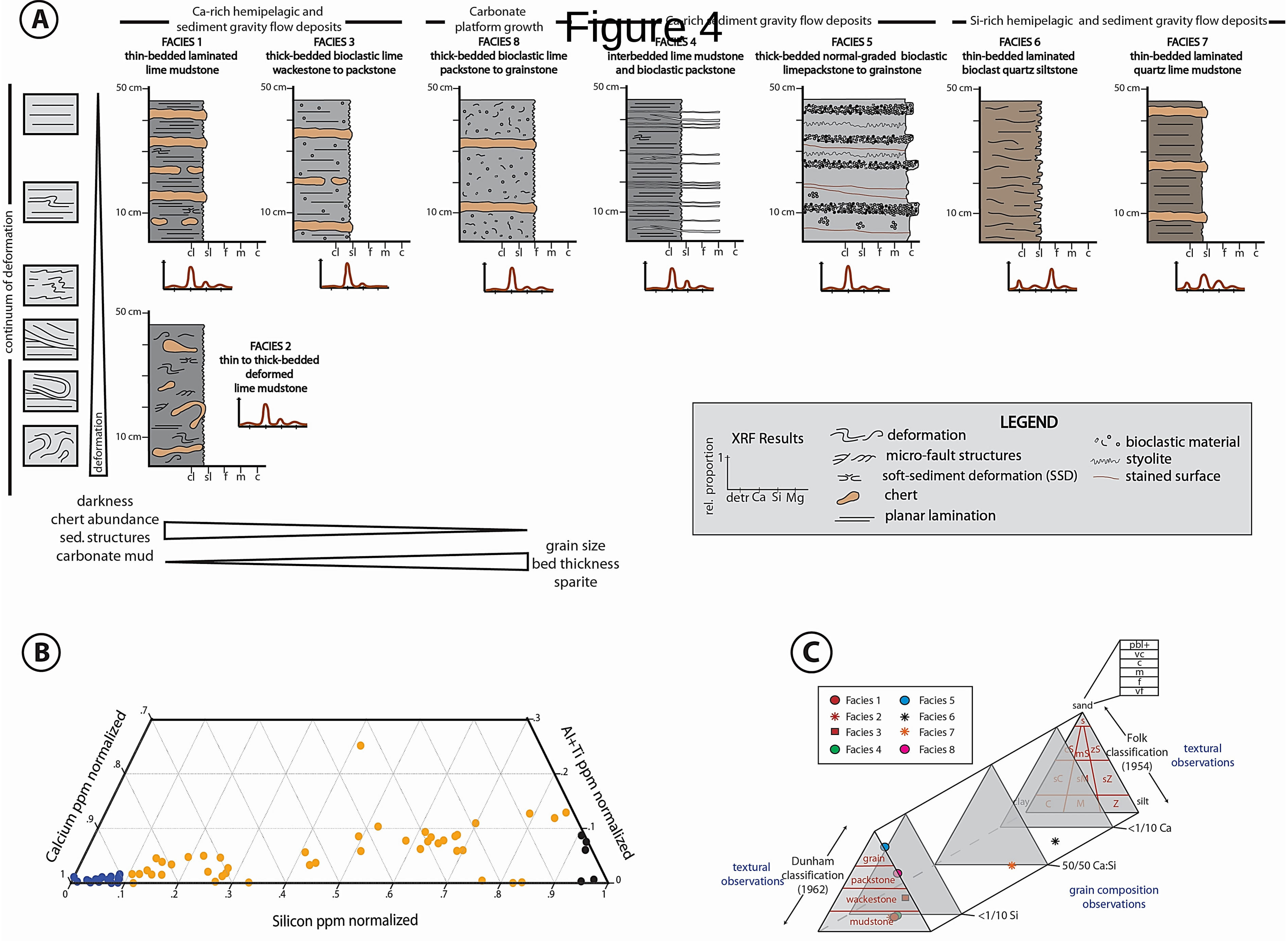

A
Ca-rich hemipelagic and sediment gravity flow deposits
Carbonate platform growth
Ca-rich sediment gravity flow deposits
Si-rich hemipelagic and sediment gravity flow deposits
FACIES 1 thin-bedded laminated lime mudstone
FACIES 3 thick-bedded bioclastic lime wackestone to packstone
FACIES 8 thick-bedded bioclastic lime packstone to grainstone
FACIES 4 interbedded lime mudstone and bioclastic packstone
FACIES 5 thick-bedded normal-graded bioclastic limepackstone to grainstone
FACIES 6 thin-bedded laminated bioclast quartz siltstone
FACIES 7 thin-bedded laminated quartz lime mudstone
FACIES 2 thin to thick-bedded deformed lime mudstone
50 cm
10 cm
cl sl f m c
continuum of deformation
deformation
darkness
chert abundance
sed. structures
carbonate mud
grain size
bed thickness
sparite
LEGEND
XRF Results
rel. proportion
1
detr Ca Si Mg
deformation
micro-fault structures
soft-sediment deformation (SSD)
chert
planar lamination
bioclastic material
stylolite
stained surface
B
Calcium ppm normalized
Al+Ti ppm normalized
Silicon ppm normalized
C
Facies 1
Facies 2
Facies 3
Facies 4
Facies 5
Facies 6
Facies 7
Facies 8
pbl+
vc
c
m
f
vf
sand
Folk classification (1954)
textural observations
silt
clay
<1/10 Ca
50/50 Ca:Si
<1/10 Si
Dunham classification (1962)
grain
packstone
wackestone
mudstone
grain composition observations

Figure 5

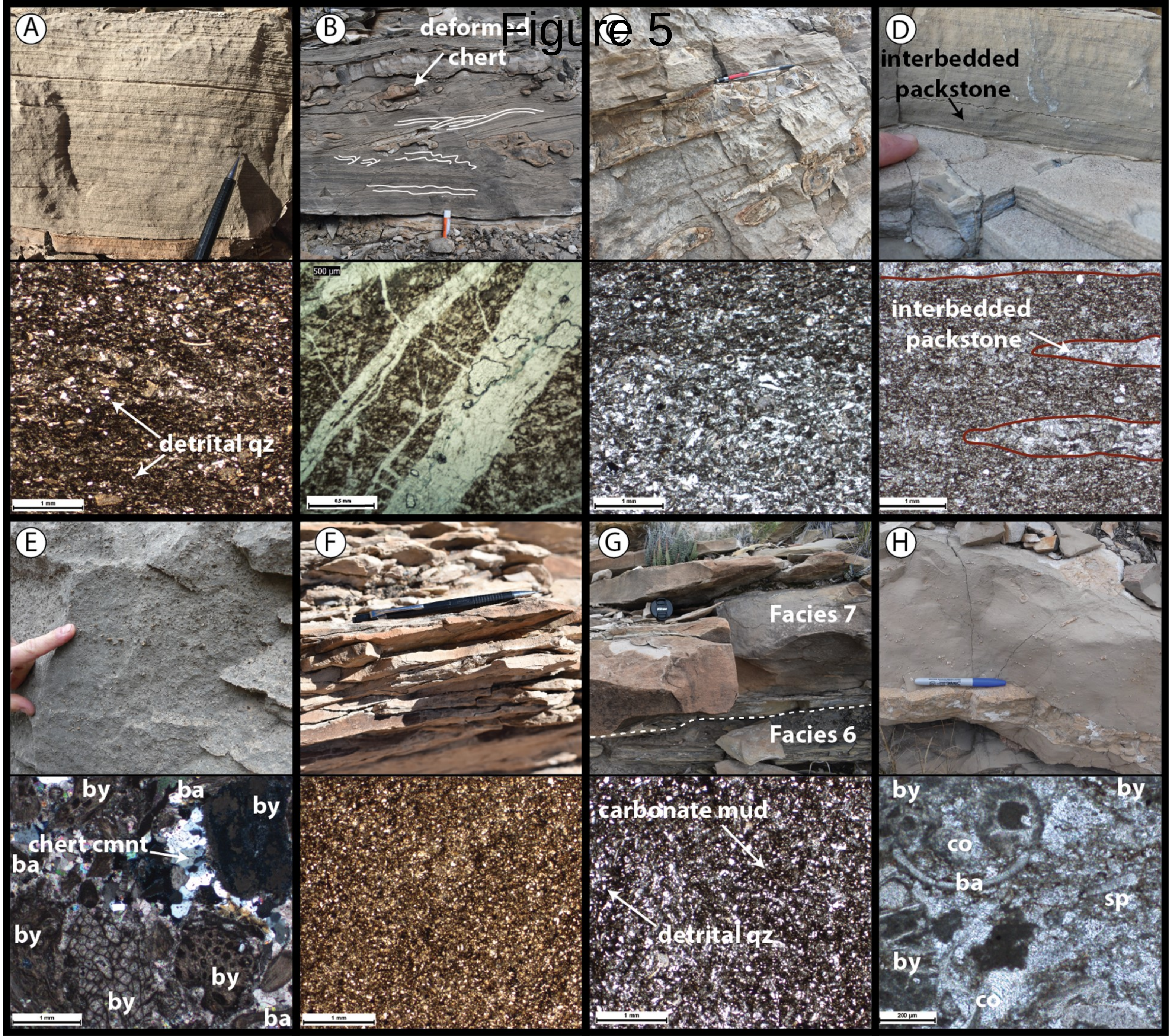

A
B
deformed chert
C
D
interbedded packstone
500 µm
detrital qz
1 mm
0.5 mm
1 mm
interbedded packstone
1 mm
E
F
G
Facies 7
Facies 6
H
by
ba
by
chert cmnt
ba
by
by
by
ba
1 mm
1 mm
carbonate mud
detrital qz
1 mm
by
by
co
ba
sp
by
co
200 µm

Figure 6

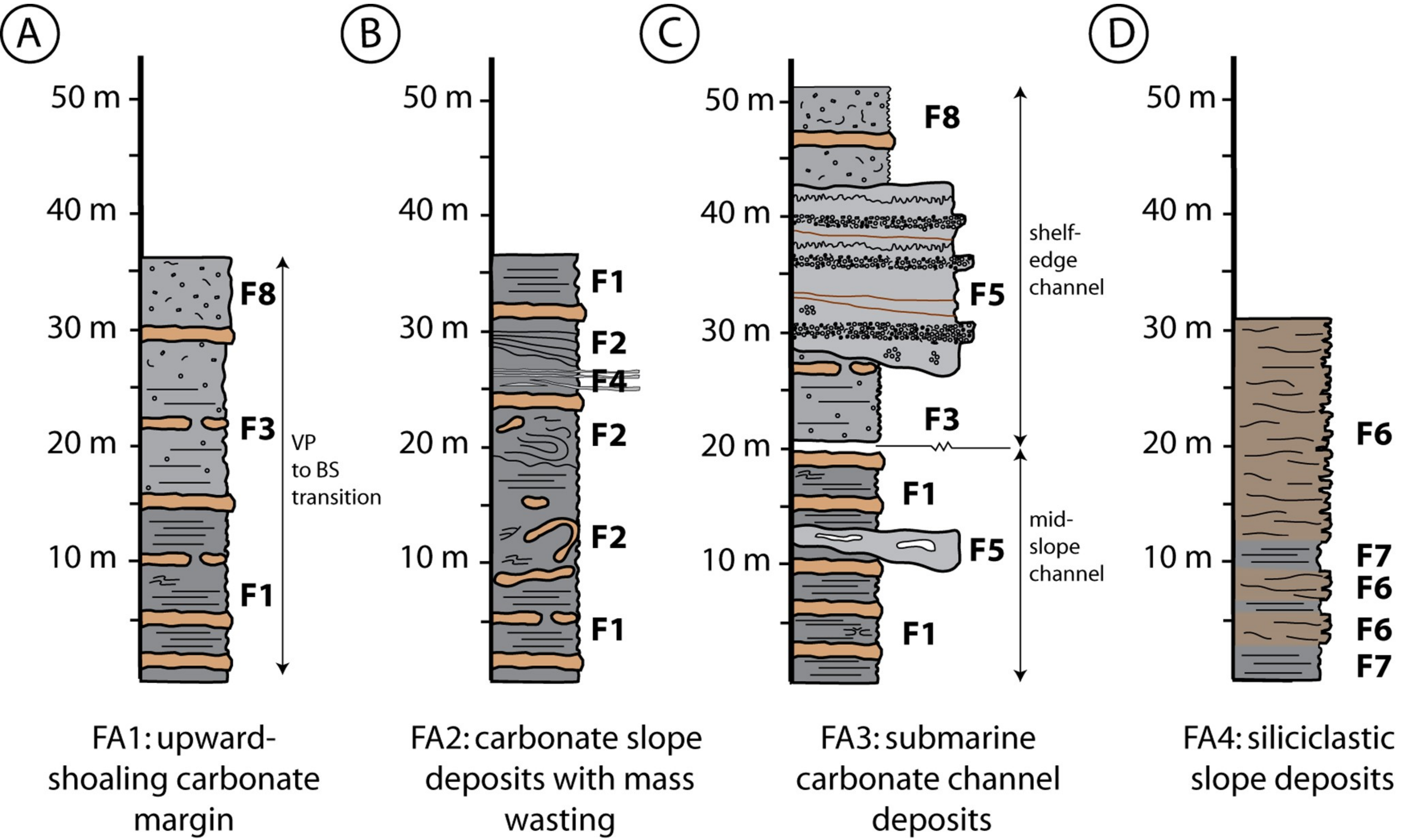
A
50 m
40 m
30 m
20 m
10 m
F8
F3
F1
VP
to BS
transition
FA1: upward-
shoaling carbonate
margin
B
50 m
40 m
30 m
20 m
10 m
F1
F2
F4
F2
F2
F1
FA2: carbonate slope
deposits with mass
wasting
C
50 m
40 m
30 m
20 m
10 m
F8
F5
F3
F1
F5
F1
shelf-
edge
channel
mid-
slope
channel
FA3: submarine
carbonate channel
deposits
D
50 m
40 m
30 m
20 m
10 m
F6
F7
F6
F6
F7
FA4: siliciclastic
slope deposits

Figure 7

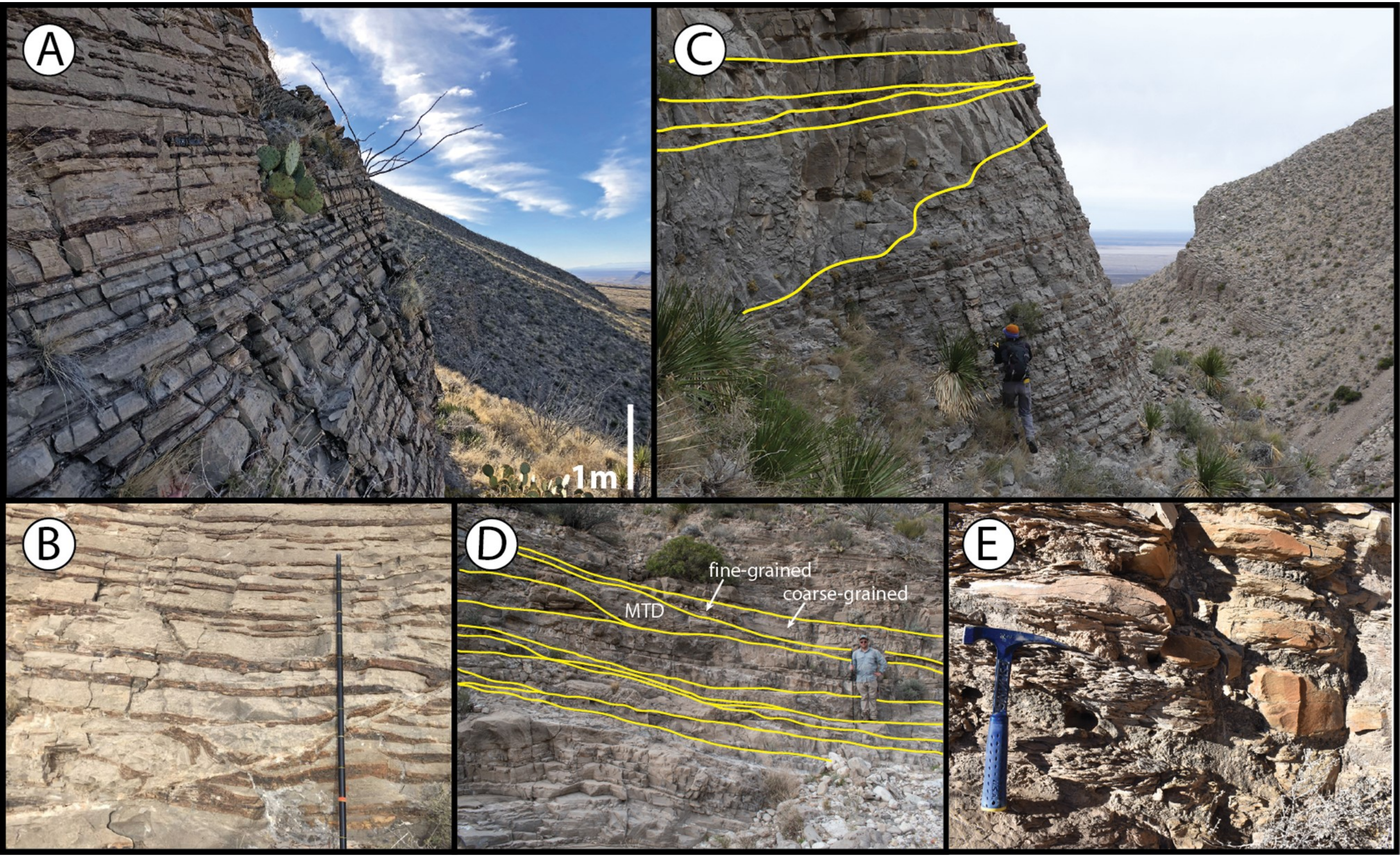

Figure 8

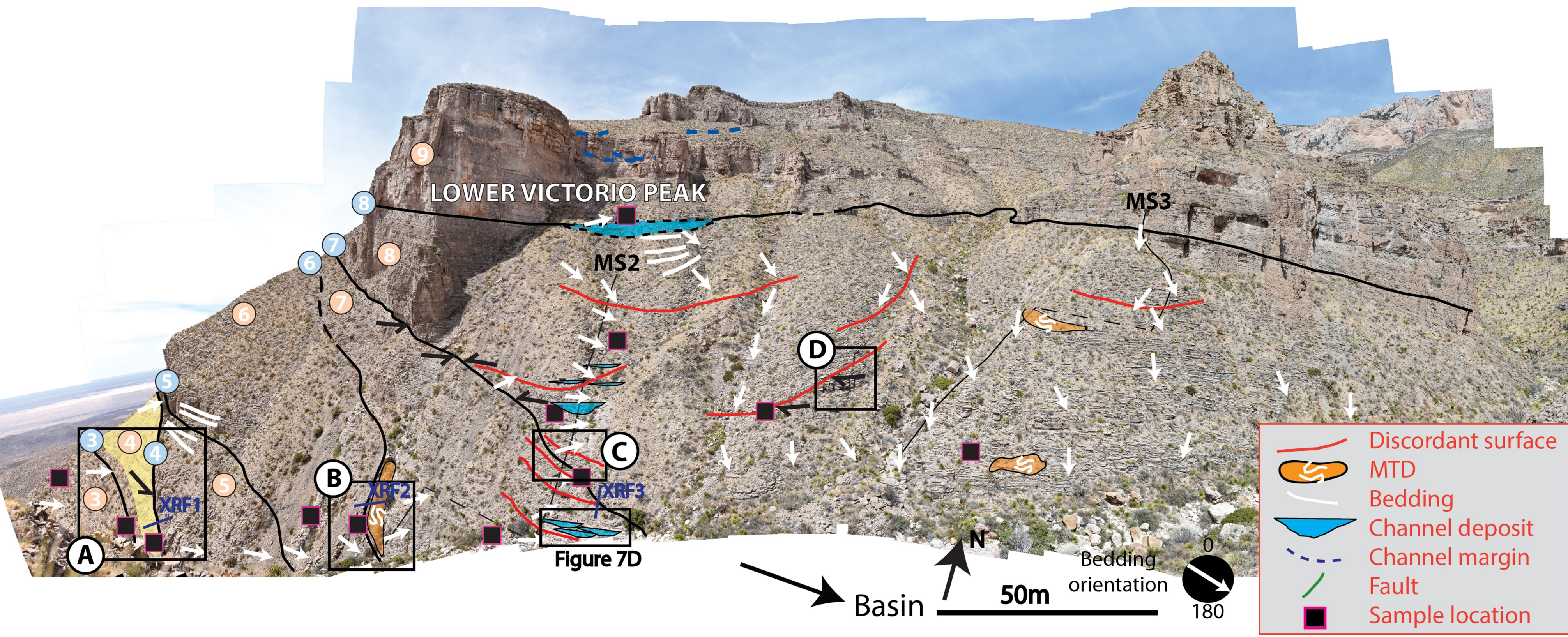

LOWER VICTORIO PEAK
MS2
MS3
A
B
C
D
XRF1
XRF2
XRF3
Figure 7D
3
4
5
6
7
8
9
N
Basin
50m
Bedding orientation
0
180
Discordant surface
MTD
Bedding
Channel deposit
Channel margin
Fault
Sample location

Figure 9

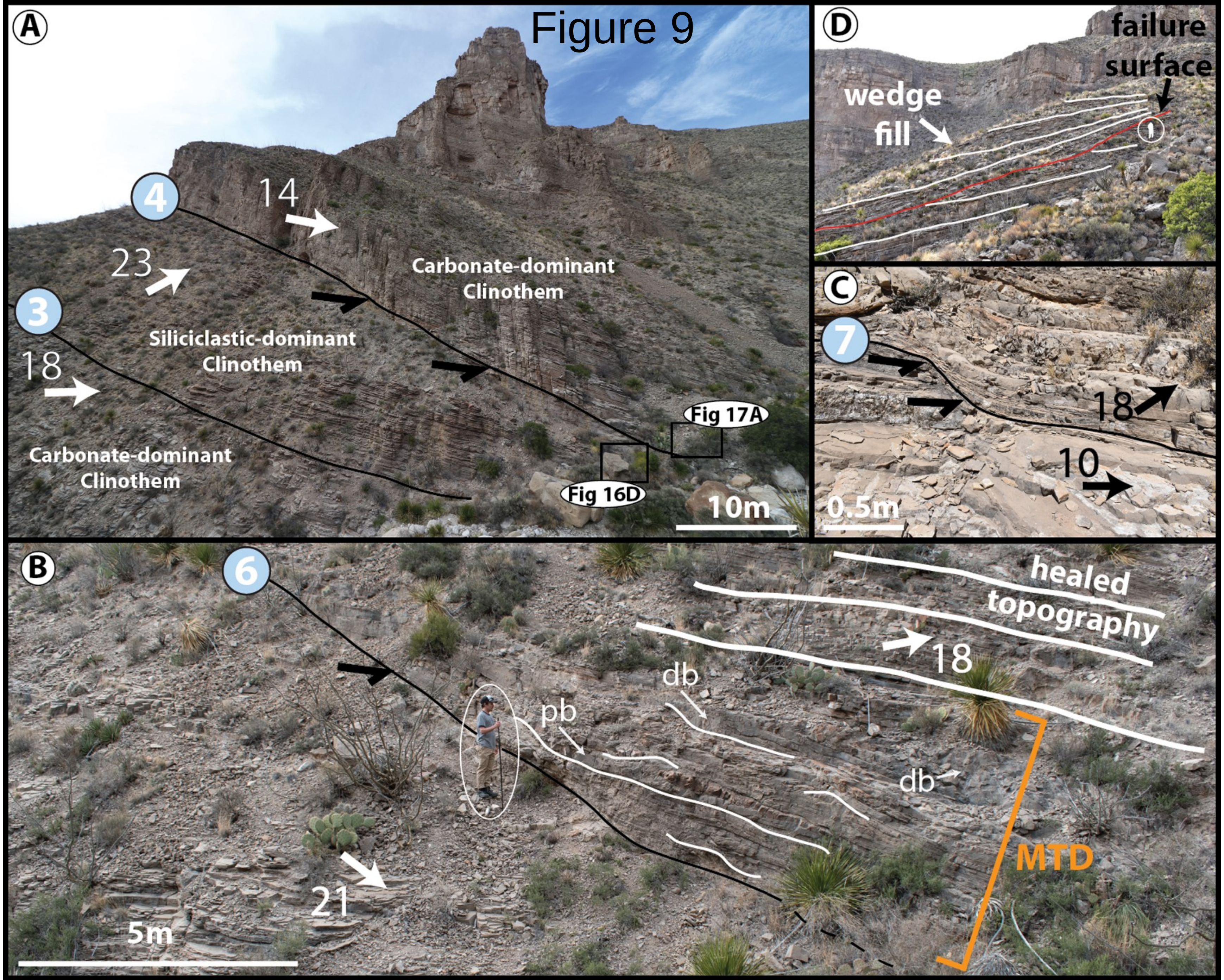

A
4
14
23
3
18
Carbonate-dominant Clinothem
Siliciclastic-dominant Clinothem
Carbonate-dominant Clinothem
Fig 17A
Fig 16D
10m
D
failure surface
wedge fill
C
7
18
10
0.5m
B
6
healed topography
18
db
pb
db
MTD
21
5m

Figure 10

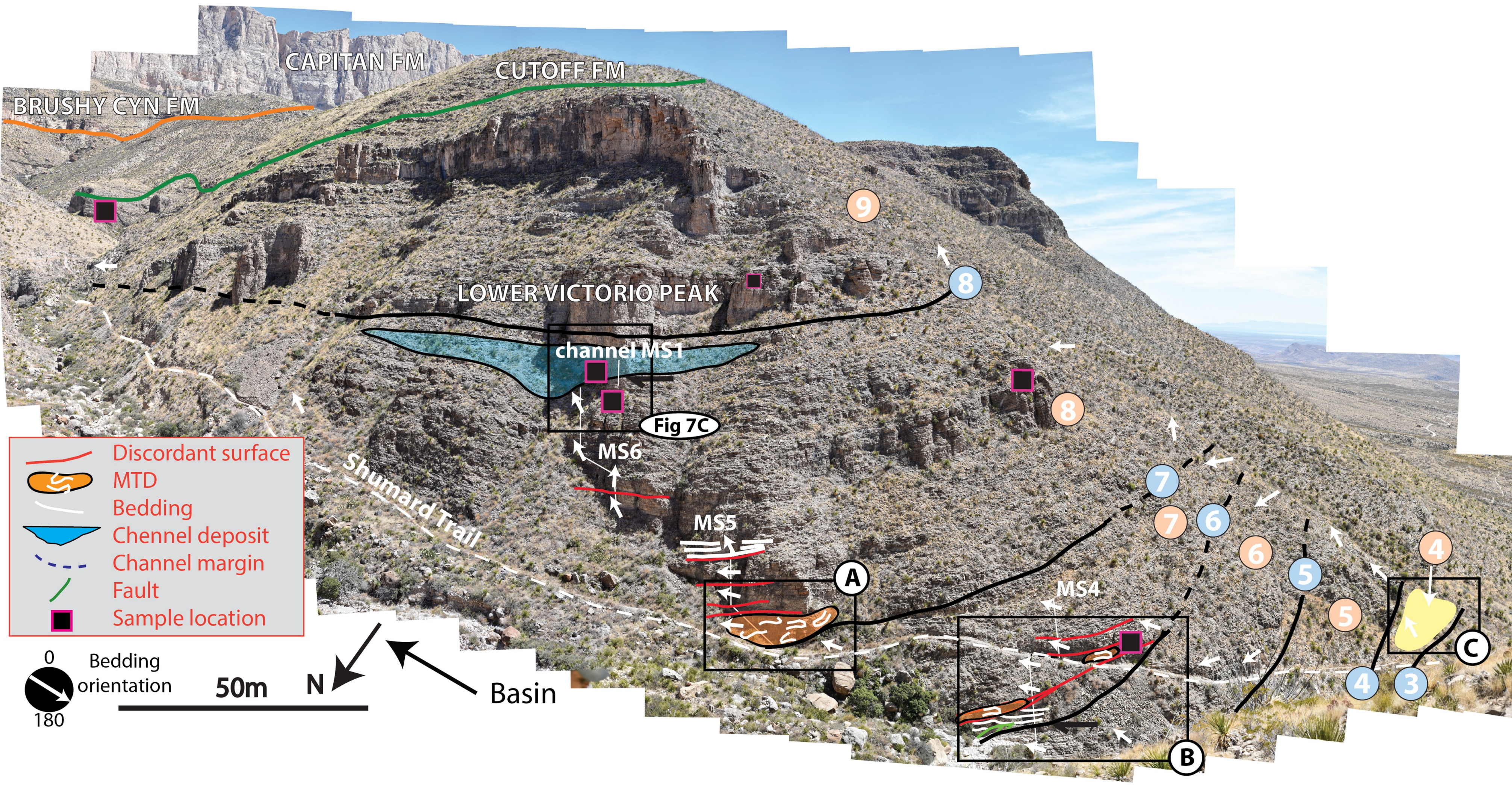

CAPITAN FM
CUTOFF FM
BRUSHY CYN FM
LOWER VICTORIO PEAK
channel MS1
Fig 7C
MS6
MS5
MS4
Shumard Trail
A
B
C
9
8
8
7
7
6
6
5
5
4
4
3
Discordant surface
MTD
Bedding
Chennel deposit
Channel margin
Fault
Sample location
0
180
Bedding orientation
50m
N
Basin

Figure 11

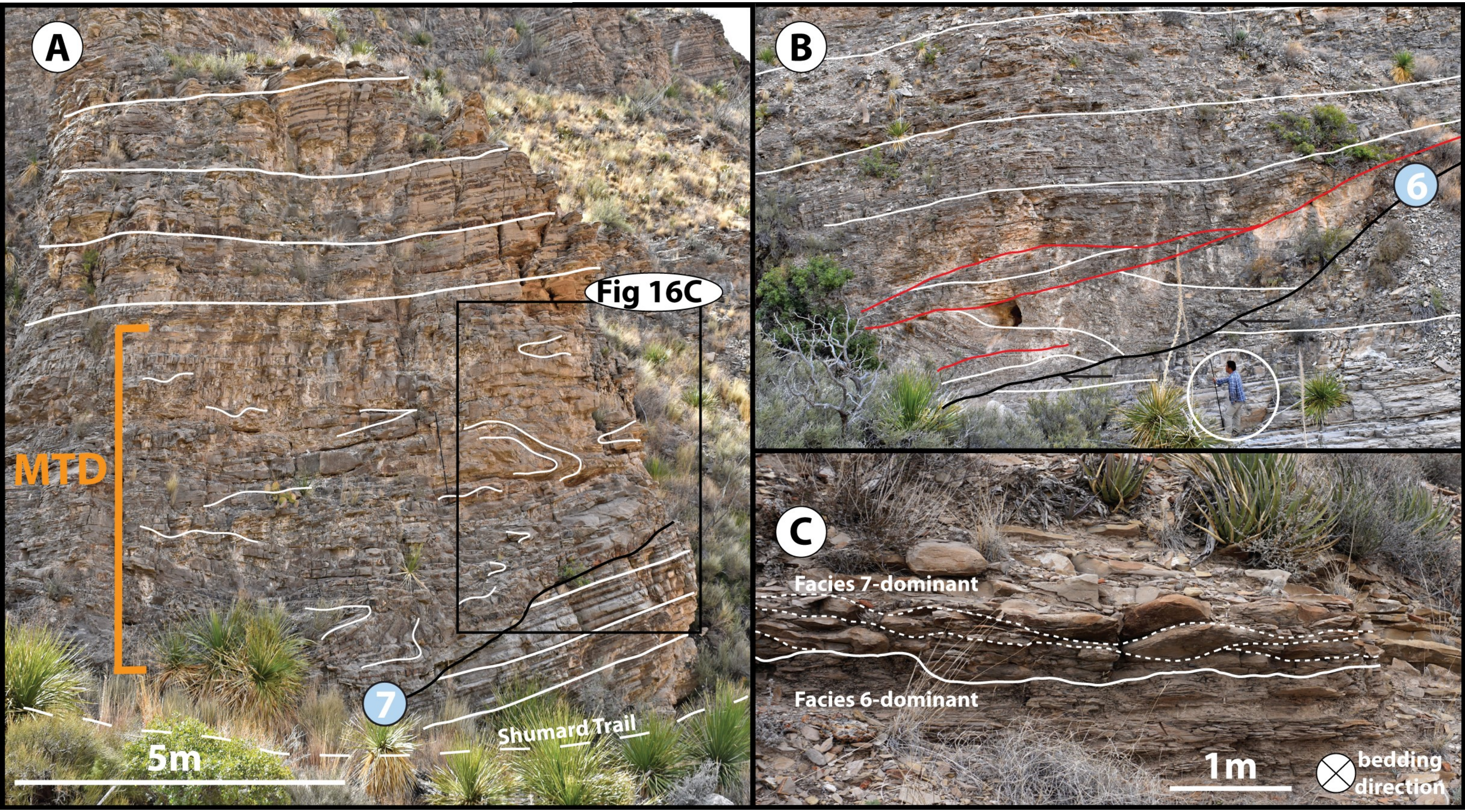
A
Fig 16C
MTD
7
Shumard Trail
5m
B
6
C
Facies 7-dominant
Facies 6-dominant
1m
bedding
direction

Figure 12

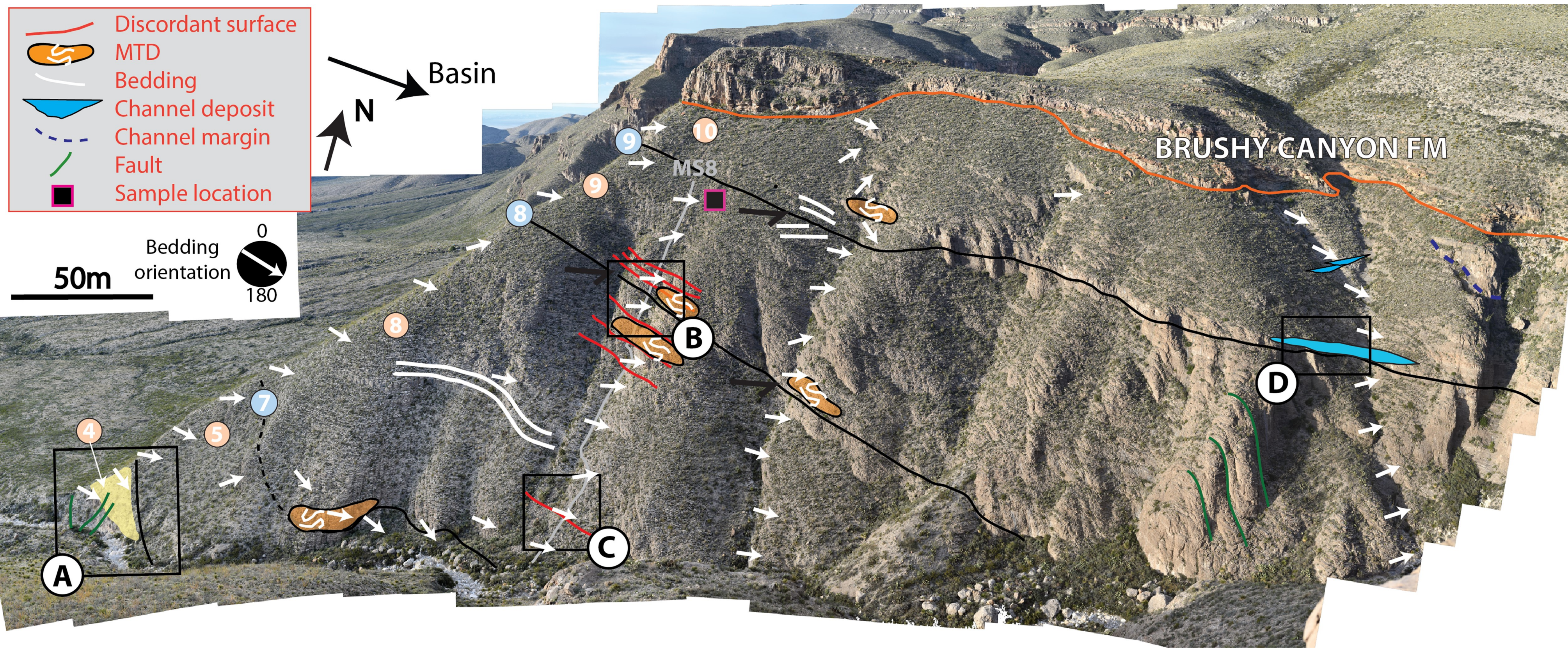

Discordant surface
MTD
Bedding
Channel deposit
Channel margin
Fault
Sample location
Basin
N
Bedding orientation
0
180
50m
BRUSHY CANYON FM
MS8
A
B
C
D
4
5
7
8
8
9
9
10

Figure 13

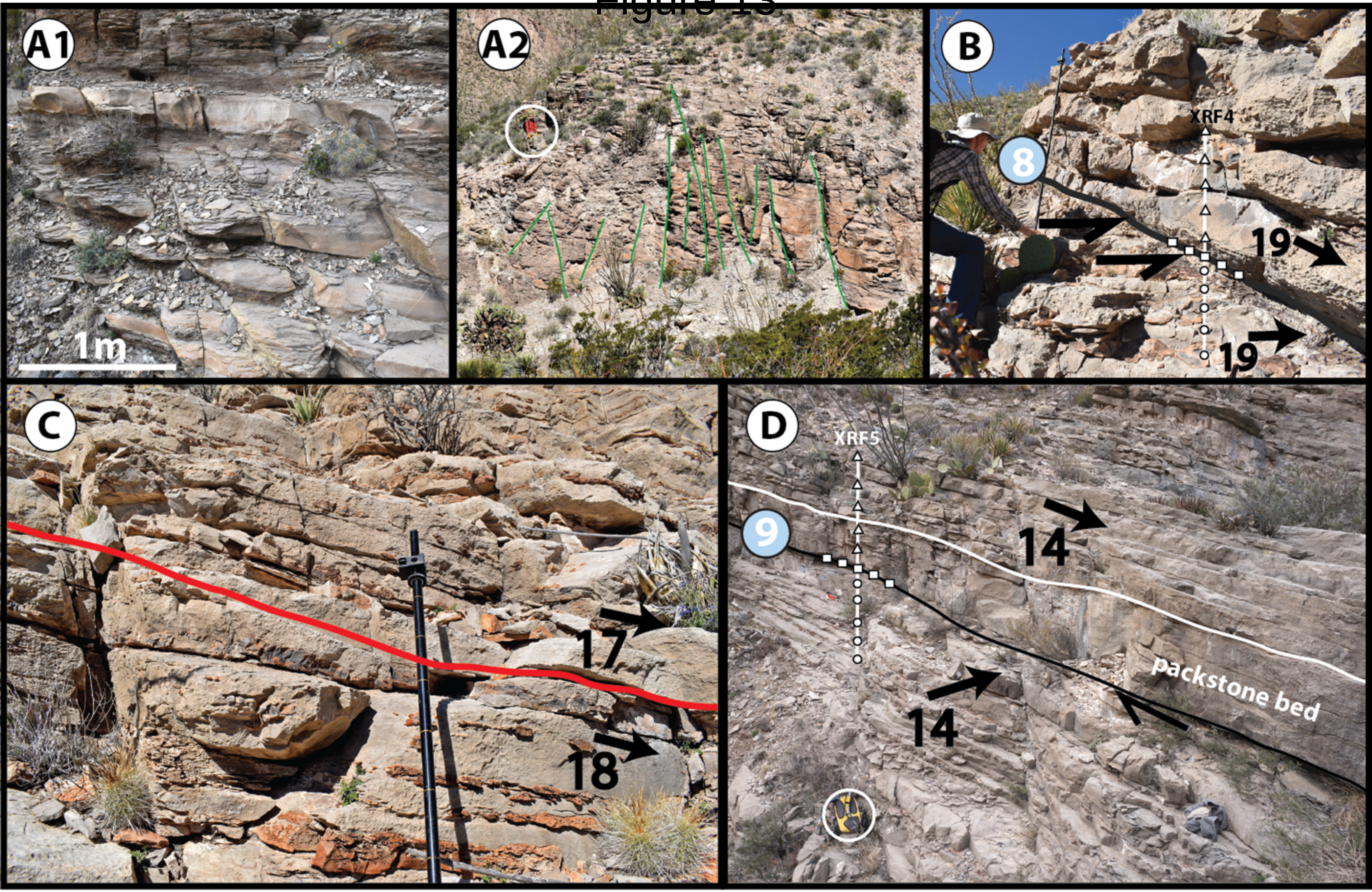

Figure 14

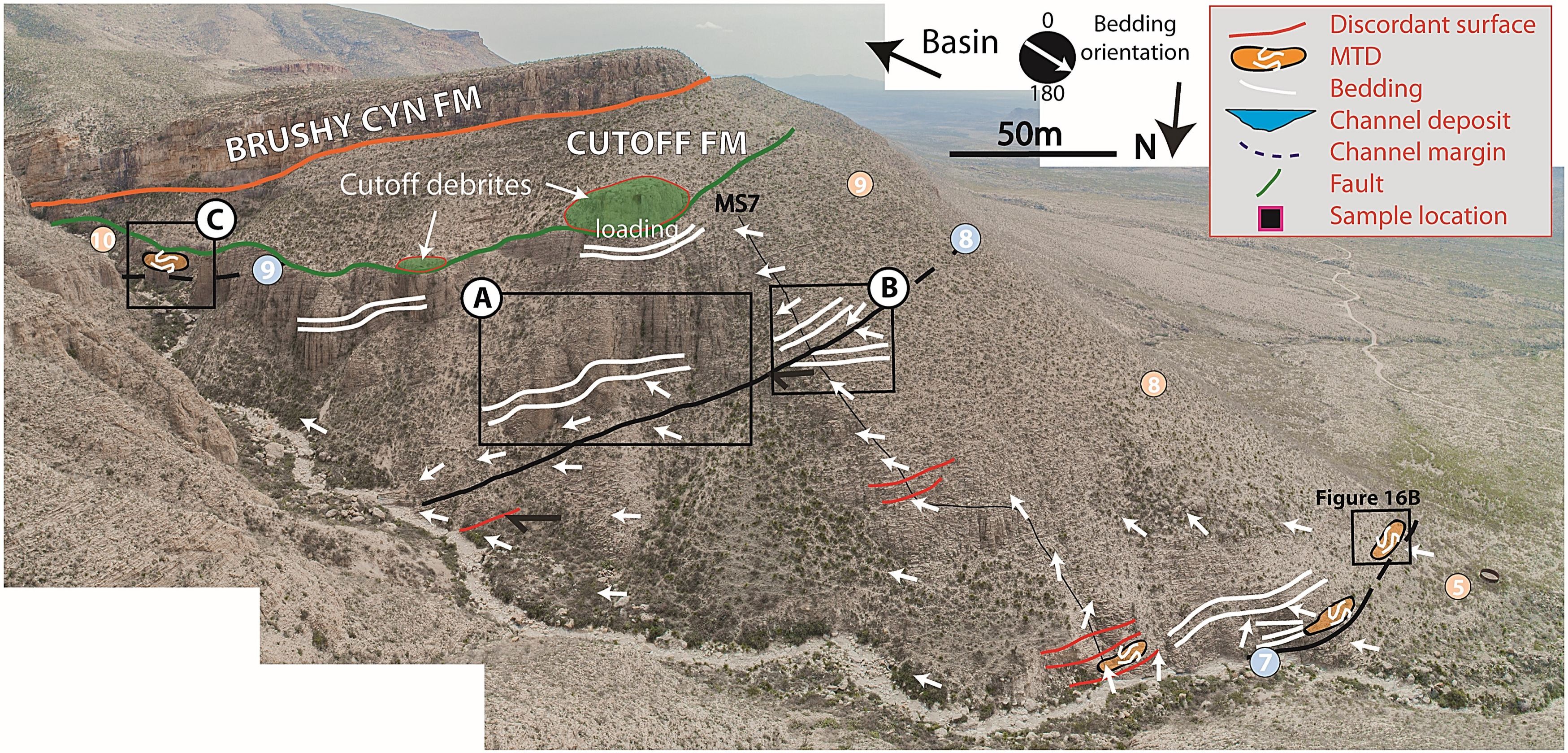

Basin
0
Bedding orientation
180
50m
N
Discordant surface
MTD
Bedding
Channel deposit
Channel margin
Fault
Sample location
BRUSHY CYN FM
CUTOFF FM
Cutoff debrites
loading
MS7
Figure 16B
A
B
C

Figure 15

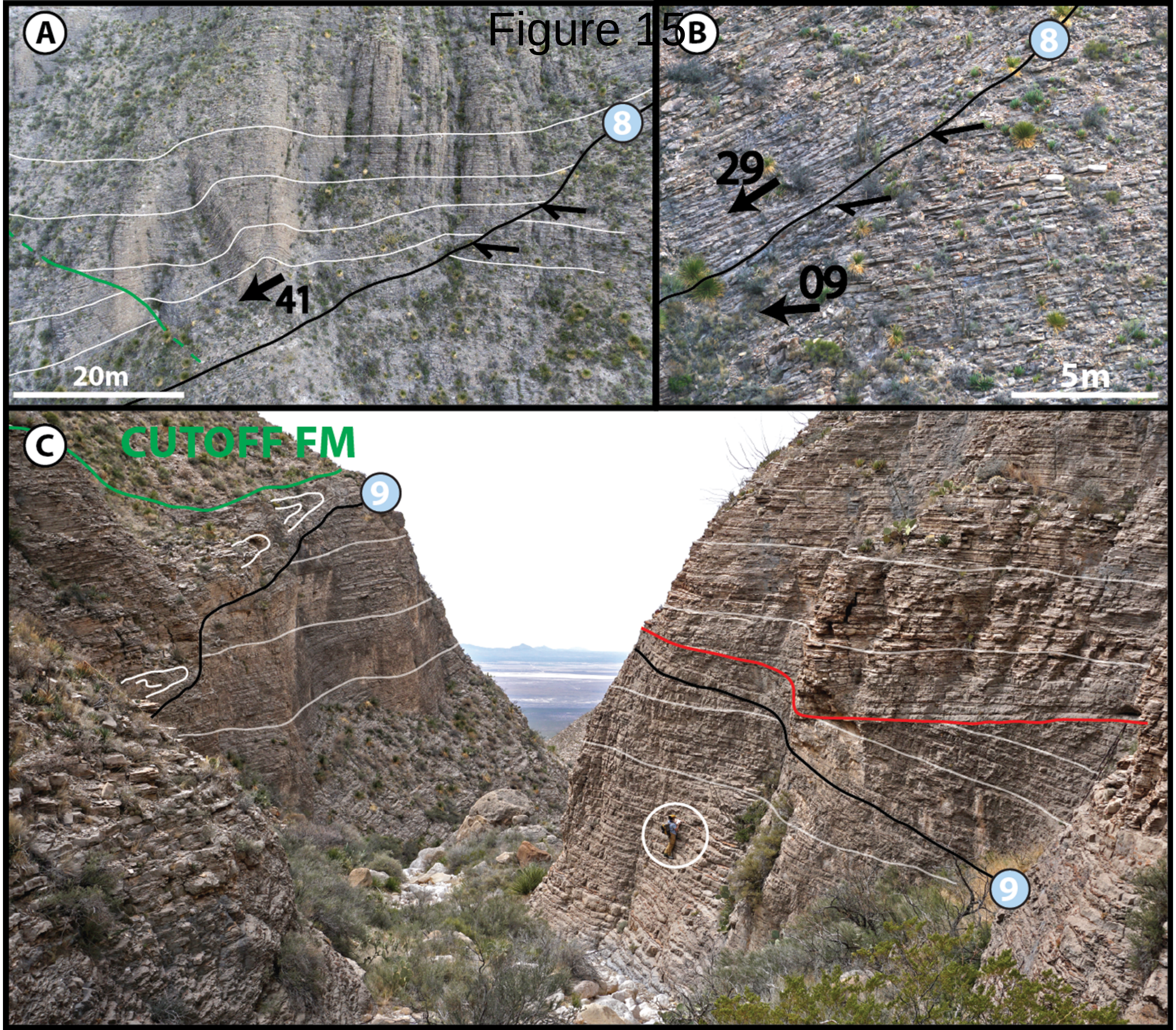

Figure 16

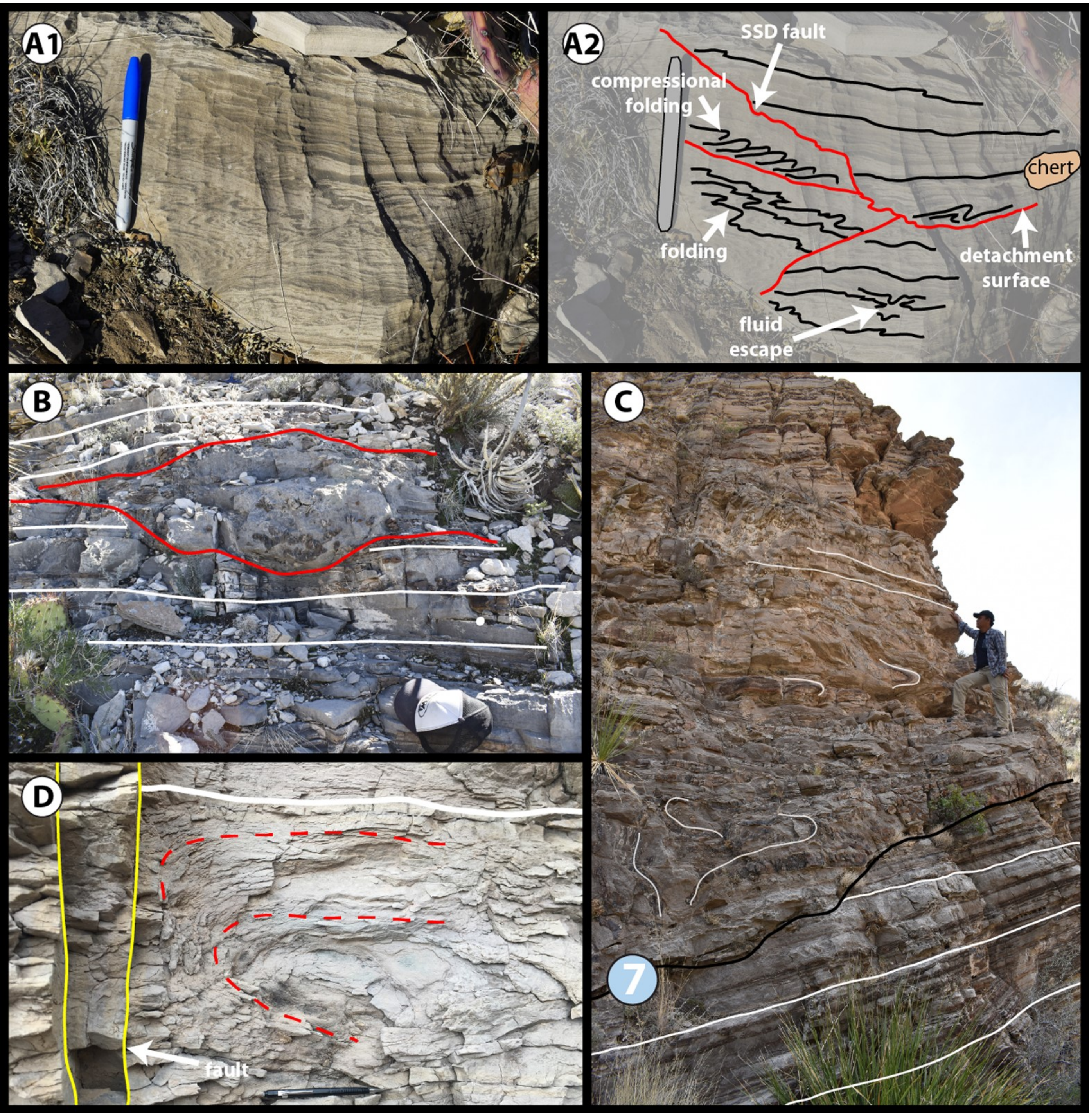

A1
A2
SSD fault
compressional folding
chert
folding
detachment surface
fluid escape
B
C
D
fault
7

Figure 17

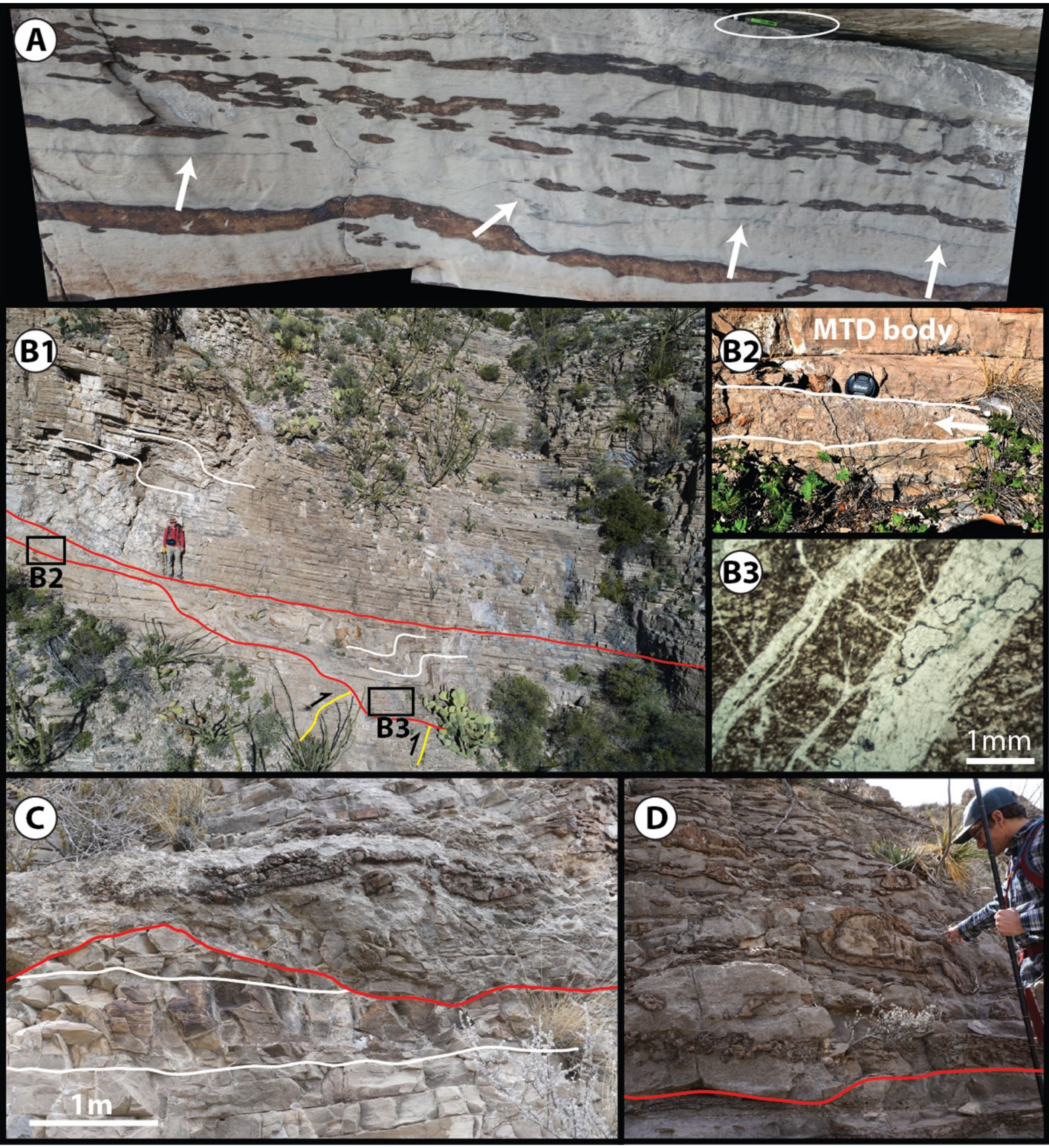

Figure 18

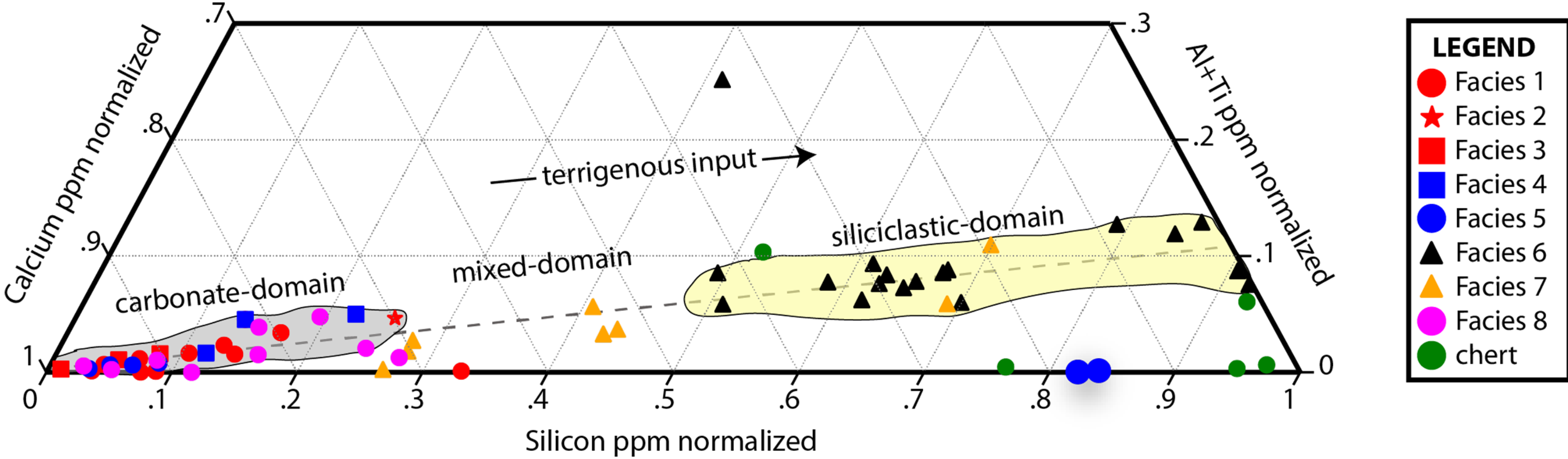

Calcium ppm normalized
.7
.8
.9
1
0
.1
.2
.3
.4
.5
.6
.7
.8
.9
1
Silicon ppm normalized
.3
.2
.1
0
Al+Ti ppm normalized
terrigenous input
siliciclastic-domain
mixed-domain
carbonate-domain
LEGEND
Facies 1
Facies 2
Facies 3
Facies 4
Facies 5
Facies 6
Facies 7
Facies 8
chert

Figure 19

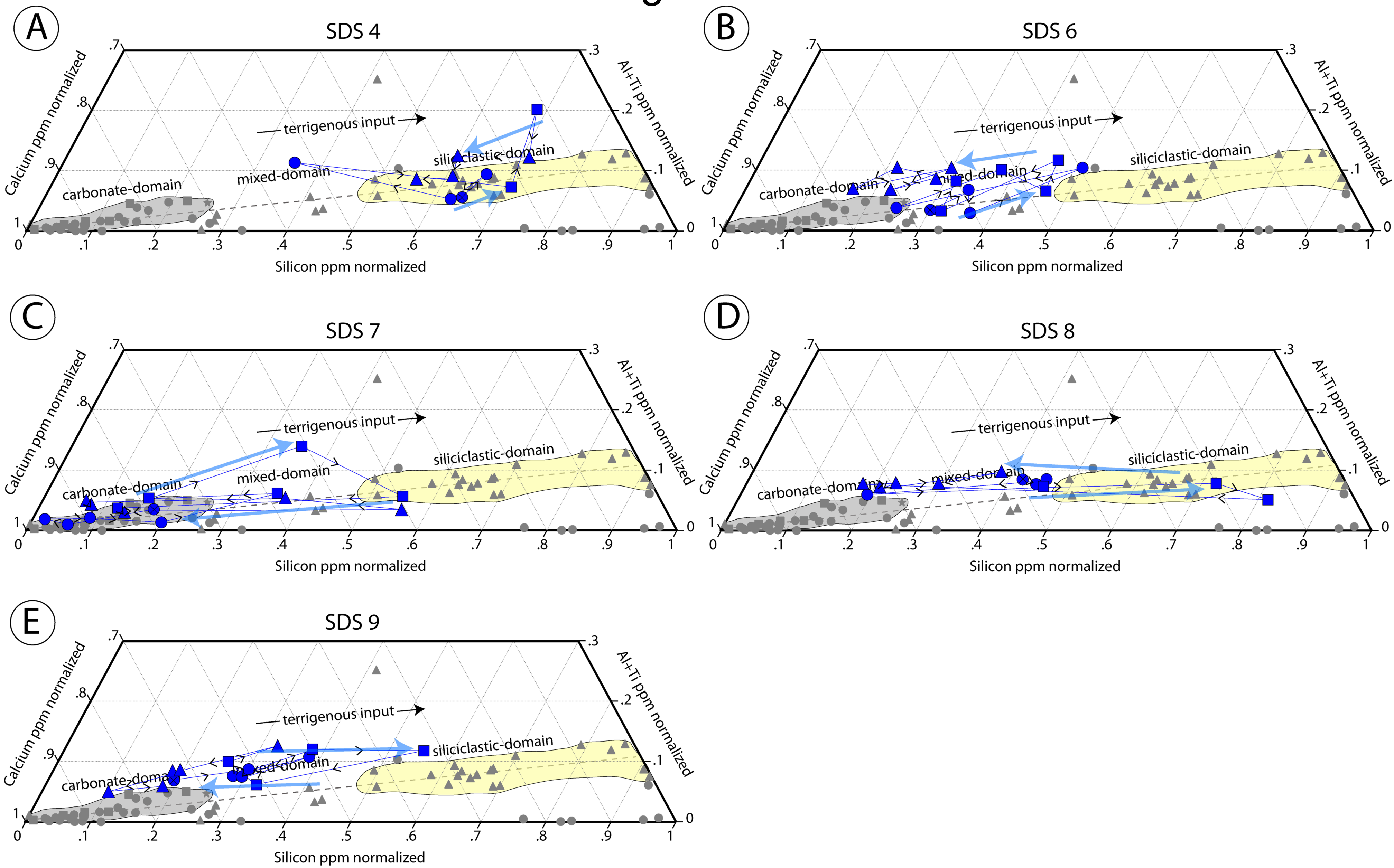
A
SDS 4
B
SDS 6
C
SDS 7
D
SDS 8
E
SDS 9
terrigenous input
siliciclastic-domain
mixed-domain
carbonate-domain
Calcium ppm normalized
Al+Ti ppm normalized
Silicon ppm normalized
.7
.8
.9
1
.3
.2
.1
0
.1
.2
.3
.4
.5
.6
.7
.8
.9
1

Figure 20

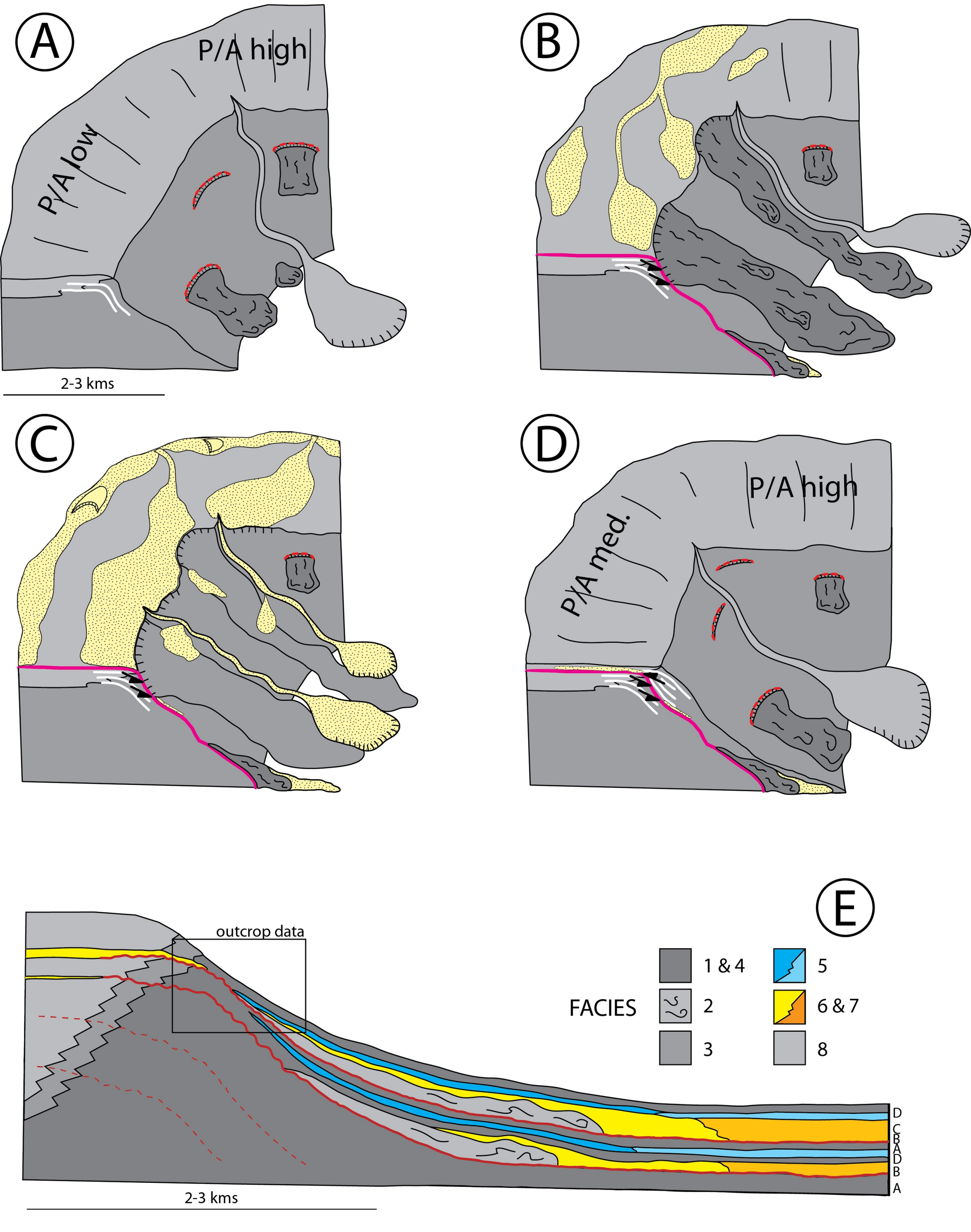

A
P/A high
P/A low
2-3 kms
B
C
D
P/A high
P/A med.
E
outcrop data
FACIES
1 & 4
2
3
5
6 & 7
8
D
C
B
A
D
B
A
2-3 kms

Figure 21

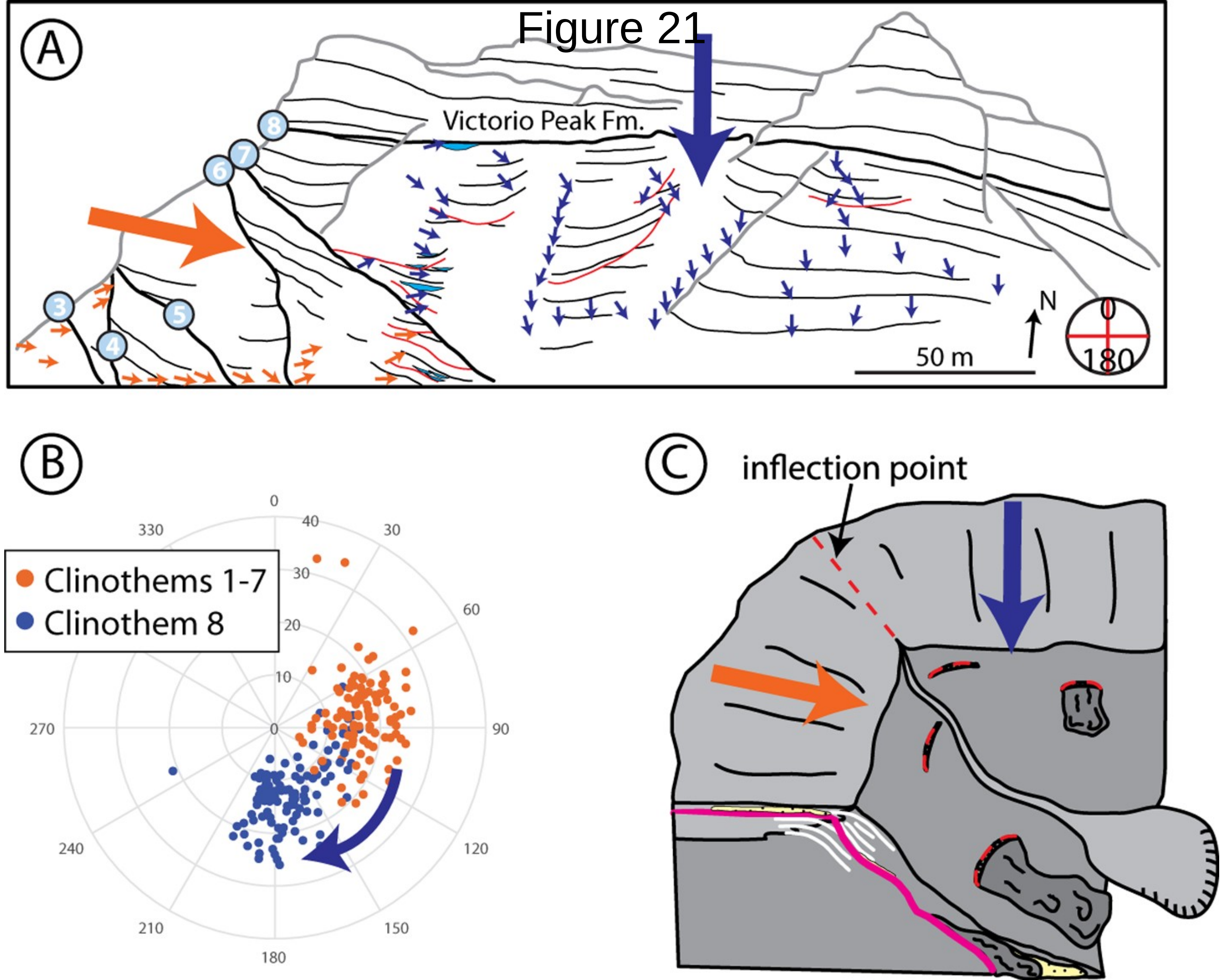
A
Victorio Peak Fm.
8
7
6
3
4
5
50 m
N
0
180
B
Clinothems 1-7
Clinothem 8
0
330
30
60
90
120
150
180
210
240
270
40
30
20
10
0
C
inflection point

Figure 22

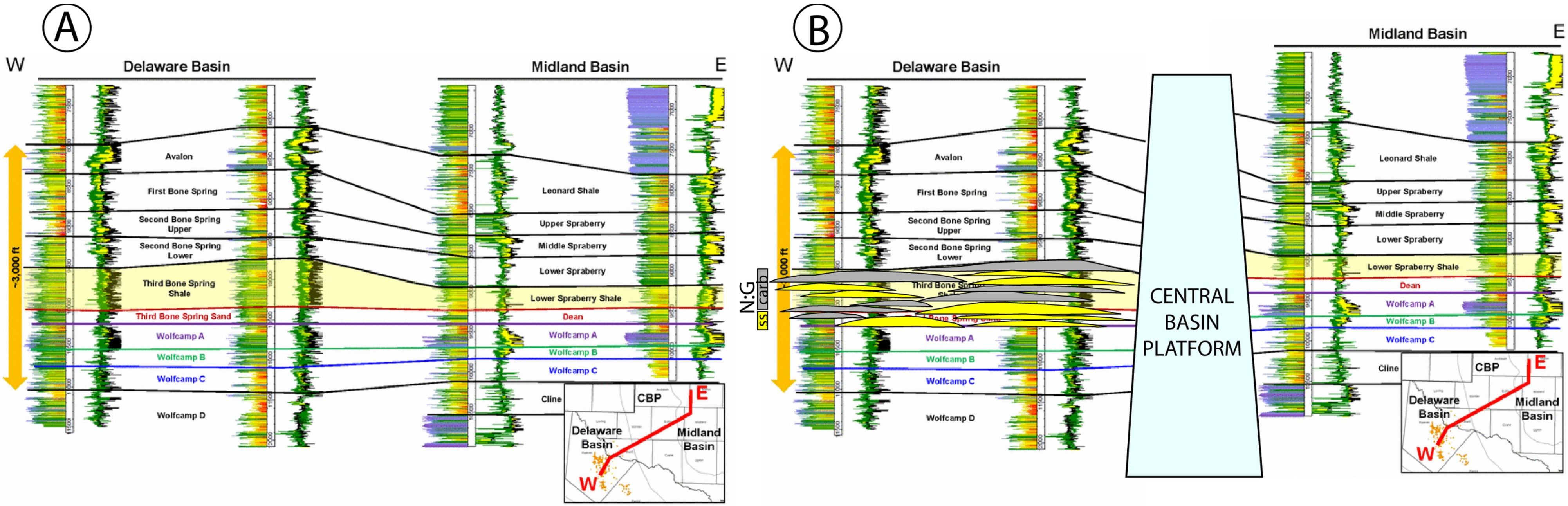

A
W
Delaware Basin
Midland Basin
E
~3,000 ft
Avalon
First Bone Spring
Second Bone Spring Upper
Second Bone Spring Lower
Third Bone Spring Shale
Third Bone Spring Sand
Wolfcamp A
Wolfcamp B
Wolfcamp C
Wolfcamp D
Leonard Shale
Upper Spraberry
Middle Spraberry
Lower Spraberry
Lower Spraberry Shale
Dean
Cline
CBP
Delaware Basin
Midland Basin
B
N:G
ss
carb
CENTRAL BASIN PLATFORM

Figure 23

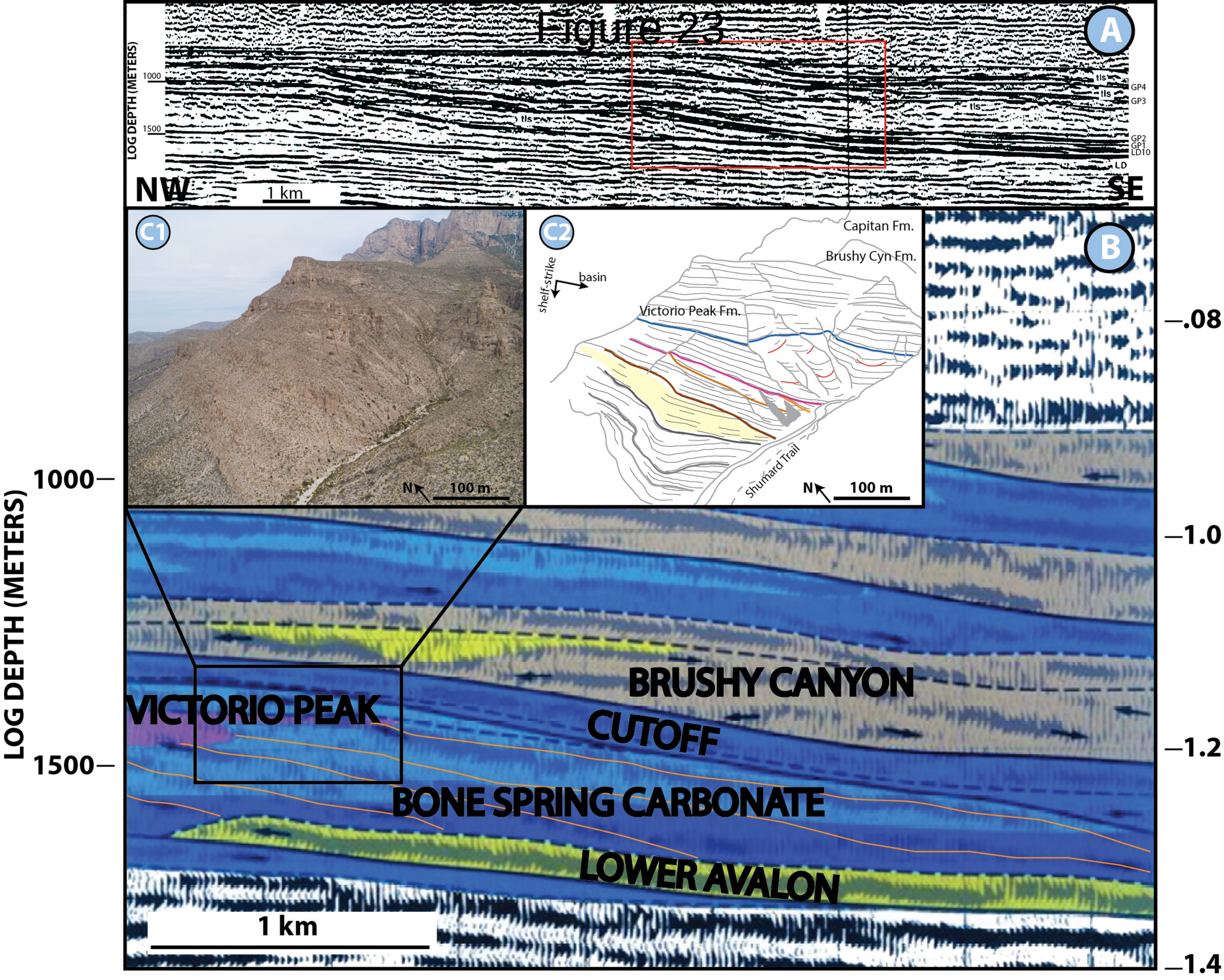
A
LOG DEPTH (METERS)
1000
1500
tls
GP4
GP3
GP2
GP1
LD10
LD
NW
SE
1 km
C1
N
100 m
C2
Capitan Fm.
Brushy Cyn Fm.
shelf-strike
basin
Victorio Peak Fm.
Shumard Trail
N
100 m
B
LOG DEPTH (METERS)
1000
1500
TIME-SECONDS
.08
1.0
1.2
1.4
BRUSHY CANYON
VICTORIO PEAK
CUTOFF
BONE SPRING CARBONATE
LOWER AVALON
1 km

Figure A.1

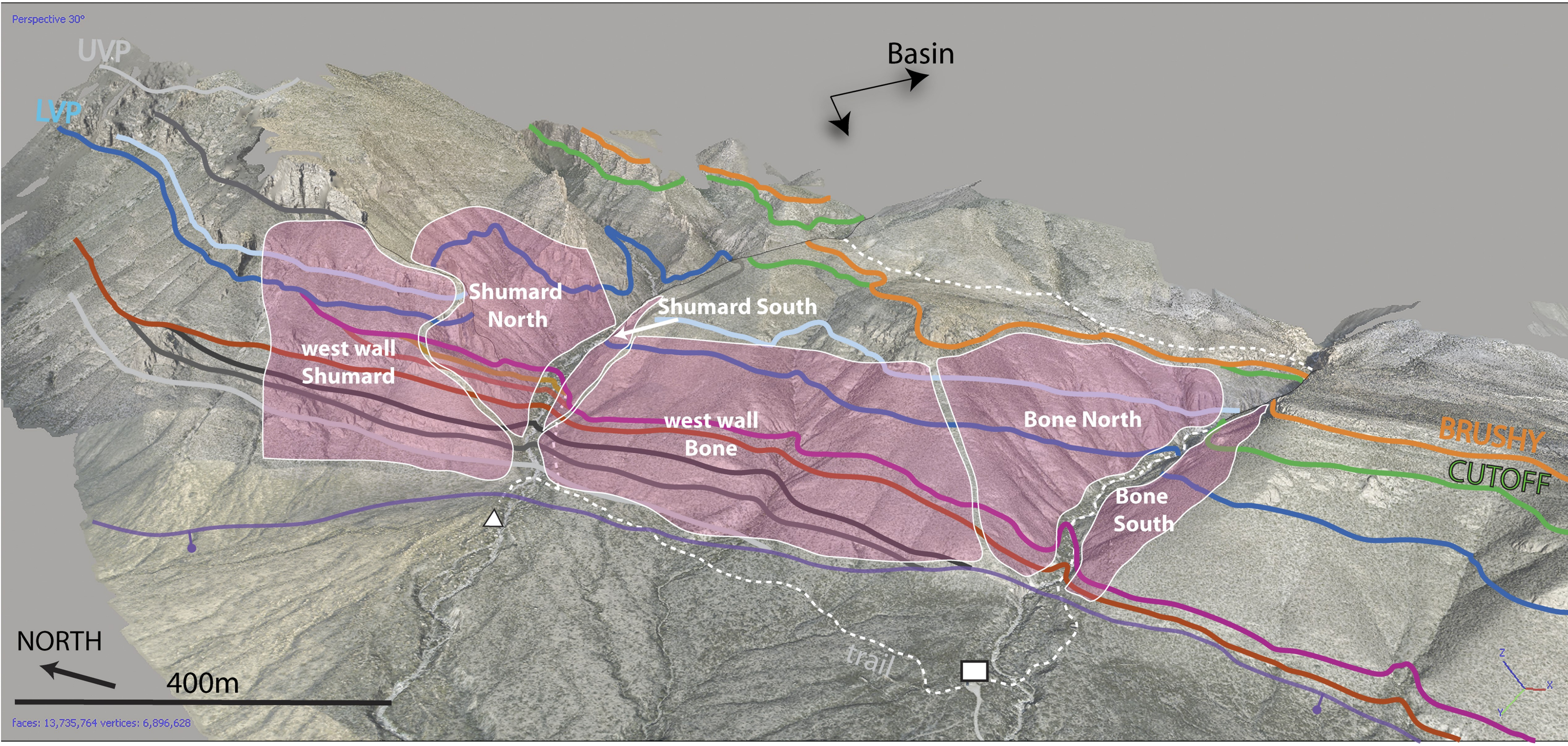

Perspective 30°
UVP
LVP
Basin
Shumard North
Shumard South
west wall Shumard
west wall Bone
Bone North
Bone South
BRUSHY
CUTOFF
trail
NORTH
400m
faces: 13,735,764 vertices: 6,896,628

Figure A.2

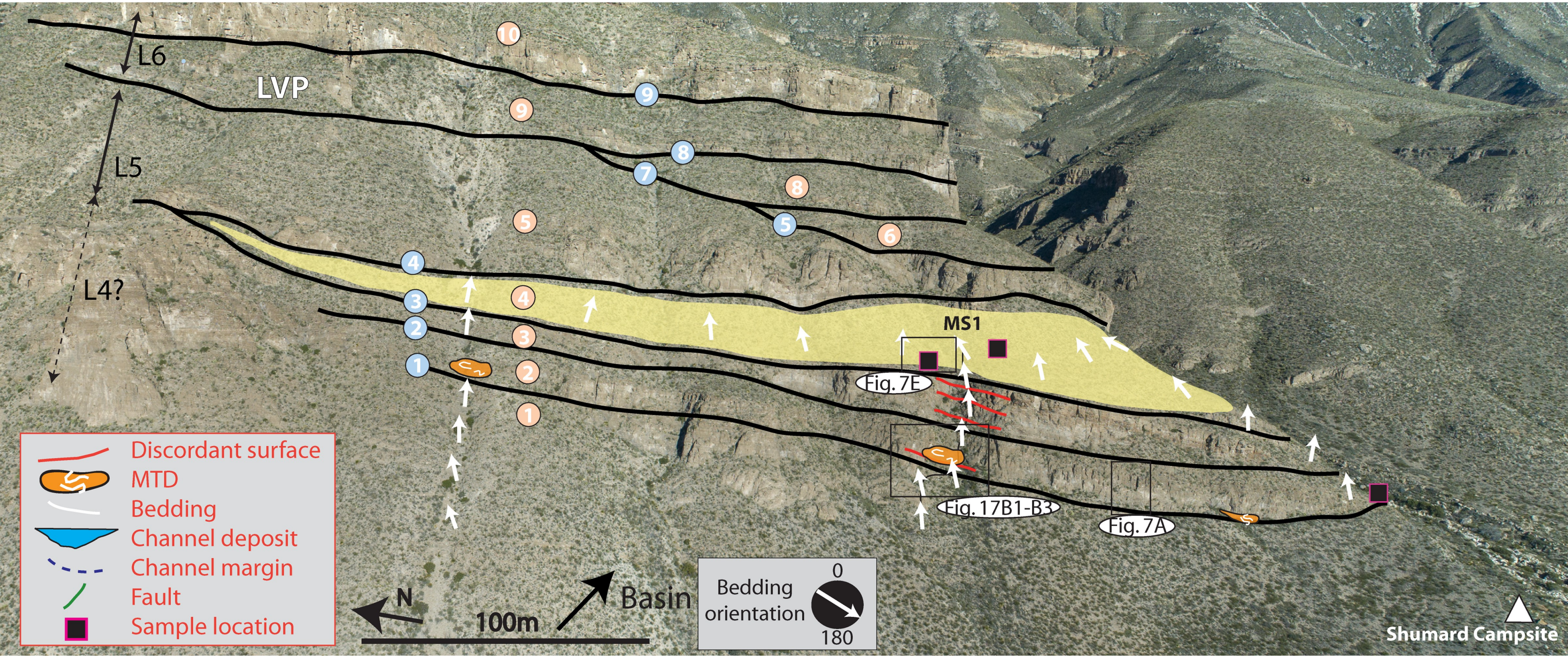

L6
LVP
L5
L4?
10
9
9
8
7
8
5
5
6
4
4
3
3
2
2
1
1
MS1
Fig. 7E
Fig. 17B1-B3
Fig. 7A
Discordant surface
MTD
Bedding
Channel deposit
Channel margin
Fault
Sample location
N
100m
Basin
Bedding orientation
0
180
Shumard Campsite

Figure A.3

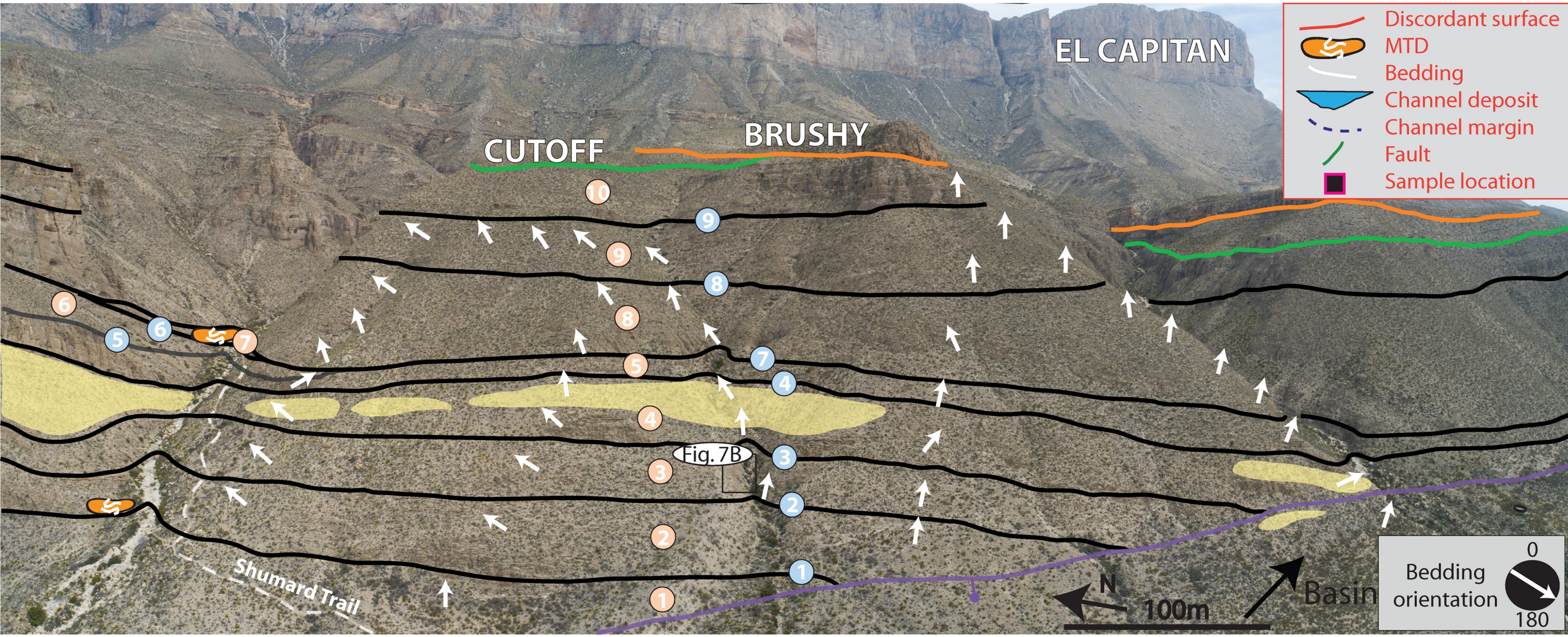
EL CAPITAN
CUTOFF
BRUSHY
Discordant surface
MTD
Bedding
Channel deposit
Channel margin
Fault
Sample location
10
9
8
7
6
5
4
3
2
1
Fig. 7B
Shumard Trail
N
100m
Basin
Bedding orientation
0
180